

CMS Draft Analysis Note

The content of this note is intended for CMS internal use and distribution only

2019/11/15

Archive Hash: 074b376-D

Archive Date: 2019/11/14

Search for VBF Higgs bosons decaying to invisible particles at 13 TeV with 2017 and 2018 data

Alp Akpinar, Andreas Albert, Zeynep Demiragli, and Siqi Yuan
Boston University (US)

Abstract

This note describes the search for invisible decays of Higgs boson produced with vector boson fusion (VBF). The search is performed using a shape-based analysis, using the data collected by CMS at $\sqrt{s} = 13 \text{ TeV}$ in 2017 and 2018, corresponding to integrated luminosities of 41.3 fb^{-1} and 59.7 fb^{-1} , respectively.

This box is only visible in draft mode. Please make sure the values below make sense.

PDFAuthor: Alp Akpinar, Andreas Albert, Zeynep Demiragli, Siqi Yuan
PDFTitle: Run-II VBFHinv BU
PDFSubject: CMS
PDFKeywords: CMS, physics, your topics

Please also verify that the abstract does not use any user defined symbols

1 Contents

2	1	Introduction	2
3	2	Samples	2
4	2.1	Data Samples	2
5	2.2	Background Samples	2
6	2.3	Signal simulation samples	4
7	3	Trigger	4
8	3.1	Efficiency measurement	5
9	4	Physics objects	9
10	4.1	Jets	10
11	4.2	Missing transverse momentum and recoil	12
12	4.3	Leptons	13
13	4.4	Photons	15
14	5	Reweighting of simulated events	17
15	5.1	Trigger efficiency reweighting	19
16	5.2	Pileup reweighting	19
17	5.3	Lepton and photon identification/reconstruction efficiency reweighting	19
18	5.4	Higher-order reweighting	26
19	6	Event selection	31
20	6.1	Signal region selection	31
21	6.2	Single muon control region selection	34
22	6.3	Single electron control region selection	39
23	6.4	Double muon control region selection	44
24	6.5	Double electron control region selection	49
25	6.6	Photon control region	54
26	7	Background estimation	58
27	7.1	Signal extraction strategy	58
28	7.2	Transfer factors	58
29	7.3	Systematic uncertainties	61
30	7.4	Control sample validation	63
31	7.5	QCD multijet estimation	63
32	8	Results	66
33	A	Comparison of 1D and 2D QCD k-factors	67
34	B	Trigger efficiencies in double muon CR	73

35 1 Introduction

36 This analysis note describes a search for events in which the Higgs boson is produced by vector
 37 boson fusion (VBF), decaying into invisible particles in the final state. The signature of such a
 38 final state will be two separated jets and an imbalance in \vec{p}_T due to the undetected particles.
 39 Two separated jets are the result of the hadronization of two final state quarks emerging from
 40 the VBF process.

41 This analysis makes use of data collected with the CMS detector in proton-proton (pp) colli-
 42 sions in 2017 and 2018 at $\sqrt{s} = 13$ TeV, corresponding to an integrated luminosity of 41.3 fb^{-1}
 43 and 59.7 fb^{-1} , respectively.

44 The analysis strategy is similar to that of 2016 VBF analysis, with several improvements. One
 45 of the major improvements in this analysis is the addition of the photon control region as the
 46 fifth control region. The addition of this new control region provides additional constraint and
 47 sensitivity on the final fit. In addition to this, the theory scale factors are re-derived in this
 48 analysis for VBF topology.

49 2 Samples

50 The analysis described in this note is performed using data collected in 2017 by CMS at 13 TeV
 51 and corresponds to an integrated luminosity of 41.5 fb^{-1} . The MC simulation samples for the
 52 background processes have been produced in the Fall17 and Autumn18 campaigns. Further
 53 details are given in the following sub-sections.

54 2.1 Data Samples

55 The datasets listed in Tab. 1 are used to select events in the signal and the control regions, and
 56 to perform measurements on physics objects used in the analysis (e.g. trigger turn-ons).

Table 1: List of datasets used to select events in the signal and control regions. Datasets for both years correspond to the Nano1June2019 campaign, otherwise known as v5. For the 2017 data, the 31Mar2018 reconstruction is used for all periods. For 2018 data, the 17Sep2018 reconstruction is used for runs A to C, and the 22Jan2019 reconstruction is used for run D.

Year	Dataset name	Events selected for
2017	/MET/Run201*/NANO AOD	Signal, single muon, double muon control regions
	/SingleElectron/Run2017*/NANO AOD	Single electron, double electron control regions
	/SinglePhoton/Run2017*/NANO AOD	Single photon control region
2018	/EGamma/Run2018*/NANO AOD	Single electron, double electron control, single photon control regions

57 2.2 Background Samples

58 Simulation datasets for the background processes are listed in Table 2 and 3. There are several
 59 Standard Model processes that pose as backgrounds to the VBF H_{inv} signal, experimental sig-
 60 nature of the final state being two jets with large rapidity separation and invariant mass, along
 61 with p_T^{miss} . These processes are as follows:

62 **Z($\nu\nu$) + jets** : This process yields the largest irreducible background in the analysis, consist-
 63 ing of a Z boson and 2 or more jets coming from either QCD or EWK vertices. Simulated

samples for this background have been produced at leading order (LO) in QCD using the aMC@NLO generator in several bins of H_T for the QCD case, and in one inclusive sample for the EWK case.

W + jets : This process is the second largest source of background in this analysis, consisting of a W boson and 2 or more jets coming from either QCD or EWK vertices. The contribution of this background can be reduced by rejecting events with charged lepton candidates (electron/muon/tau). However, this process becomes irreducible in the case where the charged leptons are outside of the detector acceptance. Simulation samples for this background have been generated at LO in QCD using the aMC@NLO generator in several bins H_T for the QCD case, and in once inclusive sample for the EWK case.

Z($\ell\ell$) + jets : This process mimics signal-like events in the case where the leptons coming from the Z boson decay are not reconstructed. As in the case of $W \rightarrow \ell\nu$, the contribution of this background is reduced by rejecting events with charged leptons. Simulation samples for this process have been generated at LO in QCD using the aMC@NLO generator in bins of H_T for the QCD case, and in once inclusive sample for the EWK case.

Top: Top-quark decays (both $t\bar{t}$ and single top) also contribute background events to this analysis. In these processes, the W boson produced in a top-quark decay further decays leptonically, which produces genuine p_T^{miss} in the event. Next-to-leading order (NLO) $t\bar{t}$ simulation samples have been produced with the aMC@NLO generator with two additional partons in the matrix element. Single-top events have been generated with the Powheg generator at NLO in QCD with one additional matrix element parton.

Dibosons: Decays of diboson pairs (WW, WZ, ZZ) also constitute background processes. Typically, one of the bosons decays leptonically ($W \rightarrow \ell\nu, Z \rightarrow \nu\nu$) while the other boson decays hadronically, thus producing jets and p_T^{miss} in the final state. Simulated samples for WW, WZ and ZZ production have been generated at LO with Pythia 8.

QCD Multijet: QCD multijet events typically do not have large genuine p_T^{miss} . However, given the large cross section with which these events are produced, even a small fraction of events with jet mismeasurement results in a non-zero contribution of this process as background in the analysis. Simulated QCD samples have been generated at LO in QCD using the MadGraph generator in several bins of H_T .

The MC samples produced using MADGRAPH5_aMC@NLO, and POWHEG generators are interfaced with PYTHIA using the CP5 tune [1] for the fragmentation, hadronization, and underlying event description. In the case of the MADGRAPH5_aMC@NLO samples, jets from the matrix element calculations are matched to the parton shower description following the MLM [2] (FxFx [3]) prescription to match jets from matrix element calculations and parton shower description for LO (NLO) samples. The NNPDF 3.1 NNLO [4] parton distribution functions (PDFs) are used in all generated samples. The propagation of all final-state particles through the CMS detector is simulated with the GEANT 4 software [5]. The simulated events include the effects of pileup, with the multiplicity of reconstructed primary vertices matching that in data. The average number of pileup interactions per proton bunch crossing is found to be 32 for both the 2017 and 2018 data samples used in this analysis (assuming a total inelastic proton-proton cross-section).

Dataset name	Cross section (pb)	Order in QCD
WJetsToLNu_HT-70To100_TuneCP5_13TeV-madgraphMLM-pythia8	1296	LO
WJetsToLNu_HT-100To200_TuneCP5_13TeV-madgraphMLM-pythia8	1392	LO
WJetsToLNu_HT-200To400_TuneCP5_13TeV-madgraphMLM-pythia8	410.2	LO
WJetsToLNu_HT-400To600_TuneCP5_13TeV-madgraphMLM-pythia8	57.95	LO
WJetsToLNu_HT-600To800_TuneCP5_13TeV-madgraphMLM-pythia8	12.98	LO
WJetsToLNu_HT-800To1200_TuneCP5_13TeV-madgraphMLM-pythia8	5.39	LO
WJetsToLNu_HT-1200To2500_TuneCP5_13TeV-madgraphMLM-pythia8	1.08	LO
WJetsToLNu_HT-2500ToInf_TuneCP5_13TeV-madgraphMLM-pythia8	0.008098	LO
ZJetsToNuNu_HT-100To200_13TeV-madgraph	305.3	LO
ZJetsToNuNu_HT-200To400_13TeV-madgraph	91.86	LO
ZJetsToNuNu_HT-400To600_13TeV-madgraph	13.13	LO
ZJetsToNuNu_HT-600To800_13TeV-madgraph	3.242	LO
ZJetsToNuNu_HT-800To1200_13TeV-madgraph	1.501	LO
ZJetsToNuNu_HT-1200To2500_13TeV-madgraph	0.3431	LO
ZJetsToNuNu_HT-2500ToInf_13TeV-madgraph	0.005146	LO
DYJetsToLL_M-50_HT-70to100_TuneCP5_13TeV-madgraphMLM-pythia8	146.9	LO
DYJetsToLL_M-50_HT-100to200_TuneCP5_13TeV-madgraphMLM-pythia8	160.9	LO
DYJetsToLL_M-50_HT-200to400_TuneCP5_13TeV-madgraphMLM-pythia8	48.68	LO
DYJetsToLL_M-50_HT-400to600_TuneCP5_13TeV-madgraphMLM-pythia8	6.998	LO
DYJetsToLL_M-50_HT-600to800_TuneCP5_13TeV-madgraphMLM-pythia8	1.745	LO
DYJetsToLL_M-50_HT-800to1200_TuneCP5_13TeV-madgraphMLM-pythia8	0.8077	LO
DYJetsToLL_M-50_HT-1200to2500_TuneCP5_13TeV-madgraphMLM-pythia8	0.1923	LO
DYJetsToLL_M-50_HT-2500toInf_TuneCP5_13TeV-madgraphMLM-pythia8	0.003477	LO
GJets_HT-40To100_TuneCP5_13TeV-madgraphMLM-pythia8	18640	LO
GJets_HT-100To200_TuneCP5_13TeV-madgraphMLM-pythia8	8641	LO
GJets_HT-200To400_TuneCP5_13TeV-madgraphMLM-pythia8	2196	LO
GJets_HT-400To600_TuneCP5_13TeV-madgraphMLM-pythia8	258.4	LO
GJets_HT-600ToInf_TuneCP5_13TeV-madgraphMLM-pythia8	85.23	LO

Table 2: Simulated datasets for the modelling of single electroweak boson backgrounds. All datasets are accessed at the NanoAOD data tier from the v5 campaign, also known as 1Jun19.

2.3 Signal simulation samples

Simulated signal samples for invisible decays of the Higgs boson are generated using the Powheg generator at NLO in QCD. The samples are normalized to the standard model cross section for Higgs production in the given mode [6]. They are listed in Tab. 4.

3 Trigger

Events for the signal region are collected using a set of dedicated triggers designed to select events with large p_T^{miss} and large H_T^{miss} based on the online particle flow (PF) algorithm. In these dedicated trigger algorithms, identified PF muons are removed from the event before the p_T^{miss} and the H_T^{miss} objects are calculated. With this definition, the signal trigger paths can also be used to select single and double muon events for the W and Z control regions, respectively.

Electron events for the W and Z regions are selected using a single electron trigger. To ensure the trigger efficiency also for high- p_T electrons, the single electron trigger is used in combination with a single photon trigger [7]. The same photon trigger is used to select events for the photon control region.

The full list of triggers used, along with the L1 seeds and the associated primary datasets are

Data set name	Cross section (pb)	Order in QCD
EWKWMINUS2JETS_WTOLNU_M-50_TUNECP5_13TeV-madgraph-pythia8	20.35	LO
EWKWPPLUS2JETS_WTOLNU_M-50_TUNECP5_13TeV-madgraph-pythia8	25.81	LO
EWKZ2JETS_ZTOLL_M-50_TUNECP5_13TeV-madgraph-pythia8	4.321	LO
EWKZ2JETS_ZTONUNU_TUNECP5_13TeV-madgraph-pythia8	10.04	LO
AJJ_EWK_TUNECP5_13TeV_amcatnlo-pythia8	6.096	NLO
GJETS_MJJ-500_SM_5f_TUNECP5_EWK_13TeV-madgraph-pythia8	4.937	LO
GJETS_SM_5f_TUNECP5_EWK_13TeV-madgraph-pythia8	32.91	LO
TTJETS_TUNECP5_13TeV-amcatnloFXFX-pythia8	831.76	NLO
ST_t-channel_top_4f_inclusiveDecays_TUNECP5_13TeV-powhegV2-madspin-pythia8	137.458	NLO
ST_t-channel_antitop_4f_inclusiveDecays_TUNECP5_13TeV-powhegV2-madspin-pythia8	83.0066	NLO
ST_tW_top_5f_inclusiveDecays_TUNECP5_*_13TeV-powheg-pythia8	35.85	NLO
ST_tW_antitop_5f_inclusiveDecays_TUNECP5_*_13TeV-powheg-pythia8	35.85	NLO
WW_TUNECP5_13TeV-pythia8	75.91	LO
WZ_TUNECP5_13TeV-pythia8	27.56	LO
ZZ_TUNECP5_13TeV-pythia8	12.14	LO
QCD_HT1000to1500_TUNECP5_13TeV-madgraph-pythia8	1095	LO
QCD_HT1000to1500_TUNECP5_13TeV-madgraph-pythia8	1095	LO
QCD_HT100to200_TUNECP5_13TeV-madgraph-pythia8	2.369e+07	LO
QCD_HT1500to2000_TUNECP5_13TeV-madgraph-pythia8	99.27	LO
QCD_HT2000toInf_TUNECP5_13TeV-madgraph-pythia8	20.25	LO
QCD_HT200to300_TUNECP5_13TeV-madgraph-pythia8	1.554e+06	LO
QCD_HT300to500_TUNECP5_13TeV-madgraph-pythia8	324300	LO
QCD_HT300to500_TUNECP5_13TeV-madgraph-pythia8	324300	LO
QCD_HT500to700_TUNECP5_13TeV-madgraph-pythia8	29990	LO
QCD_HT50to100_TUNECP5_13TeV-madgraphMLM-pythia8	1.85e+08	LO
QCD_HT700to1000_TUNECP5_13TeV-madgraph-pythia8	6374	LO
QCD_HT700to1000_TUNECP5_13TeV-madgraph-pythia8	6374	LO

Table 3: Simulated datasets for the modelling of EWK V production and other processes. All datasets are accessed at the NanoAOD data tier from the v5 campaign, also known as 1Jun19.

Data set name	Cross section (pb)	Order in QCD
Gluglu_HToInvisible_M125_TUNECP5_13TeV_powheg_pythia8	48.58	NLO
VBF_HToInvisible_M125_13TeV_TUNECP5_powheg_pythia8	3.782	NLO

Table 4: Simulated signal datasets for the modelling of invisible Higgs boson decays. All datasets are accessed at the NanoAOD data tier from the v5 campaign, also known as 1Jun19.

121 shown in Table 5.

122 3.1 Efficiency measurement

123 3.1.1 $p_T^{\text{miss}} + H_T^{\text{miss}}$ triggers

124 The performance of the $p_T^{\text{miss}} + H_T^{\text{miss}}$ triggers is measured using single muon events. The events
 125 are selected from the SingleMuon using the HLT_IsoMu27 (HLT_IsoMu24) trigger for 2017
 126 (2018), and the offline muon is required to be well-identified and have p_T larger than 40 GeV.
 127 The same selection is required as for the single-muon control region used in the final fit (cf. sec.
 128 6.2):

- 129 1. Veto on additional leptons, photons, b jets, τ_{had} candidates.
- 130 2. $\Delta\phi(jet, \vec{p}_T^{\text{miss}}) > 0.5$ for the four leading jets with $p_T > 30$ GeV.

Table 5: HLT paths and the associated L1 seeds used in the analysis for the 2017 and 2018 datasets. The HLT paths ending in “_HT60” are backup triggers introduced to mitigate noise rate problems in 2017. Their inclusion is not strictly necessary for 2018, but is done for consistency.

Year	HLT path	L1 seed	Primary dataset
2017	HLT_PFMETNoMu120_PFMHTNoMu120_IDTight	L1_ETMHF70	MET
	HLT_PFMETNoMu120_PFMHTNoMu120_IDTight_PFHT60	L1_ETMHF80_HTT60er	MET
	HLT_Ele35_WPTight_Gsf	L1_SingleEG24	SingleElectron
		L1_SingleEG30	
	HLT_Photon200	L1_SingleJet170	SinglePhoton
2018	HLT_PFMETNoMu120_PFMHTNoMu120_IDTight	L1_SingleTau100er2p1	
		L1_ETM150	MET
		L1_ETMHF90_HTT60er	
	HLT_Ele32_WPTight_Gsf	L1_SingleIsoEG24er2p1	
		L1_SingleEG26er2p5	EGamma
		L1_SingleEG60	
	HLT_Photon200	L1_SingleEG34er2p5	
		L1_SingleJet160er2p5	
		L1_SingleJet180	
		L1_SingleTau120er2p1	
		L1_SingleEG60	EGamma

131 3. (Calo p_T^{miss} - PF p_T^{miss}) / recoil ≥ 0.5

132 4. $M_T(\ell, p_T^{\text{miss}}) < 160 \text{ GeV}$.

133 5. Leading AK4 jet with $p_T > 80 \text{ GeV}$, passing the tight jet ID.

134 6. Subleading AK4 jet with $p_T > 40 \text{ GeV}$.

135 7. $\Delta\eta_{jj} > 1.0$

136 8. $\Delta\phi_{jj} < 1.5$

137 To understand the dependence of the efficiencies on the jet kinematics, we measured the effi-
138 ciency in three different categories:

139 • Two central VBF jets: Leading two jets both satisfying $|\eta| \leq 2.4$

140 • Two forward VBF jets: Leading two jets both satisfying $|\eta| > 2.4$

141 • One central and one forward VBF jet: One of the leading jets is central with $|\eta| \leq 2.4$
142 and the other jet in the pair is forward with $|\eta| > 2.4$

143 In these three categories, efficiencies are measured as a function of M_{jj} and recoil, using both
144 data and MC samples for 2017 and 2018, separately. Figs. 60, 61, 1 and 2 show the results.

145 Fig. 1 shows the efficiencies as a function of recoil in data and MC for the three categories, for
146 2017 samples, whereas Fig. 2 shows the efficiencies as a function of recoil in data and MC for the

¹⁴⁷ three categories, for 2018 samples. Efficiencies in double muon control region, and efficiencies
¹⁴⁸ in both single and double muon regions as a function of M_{jj} can be found in B.

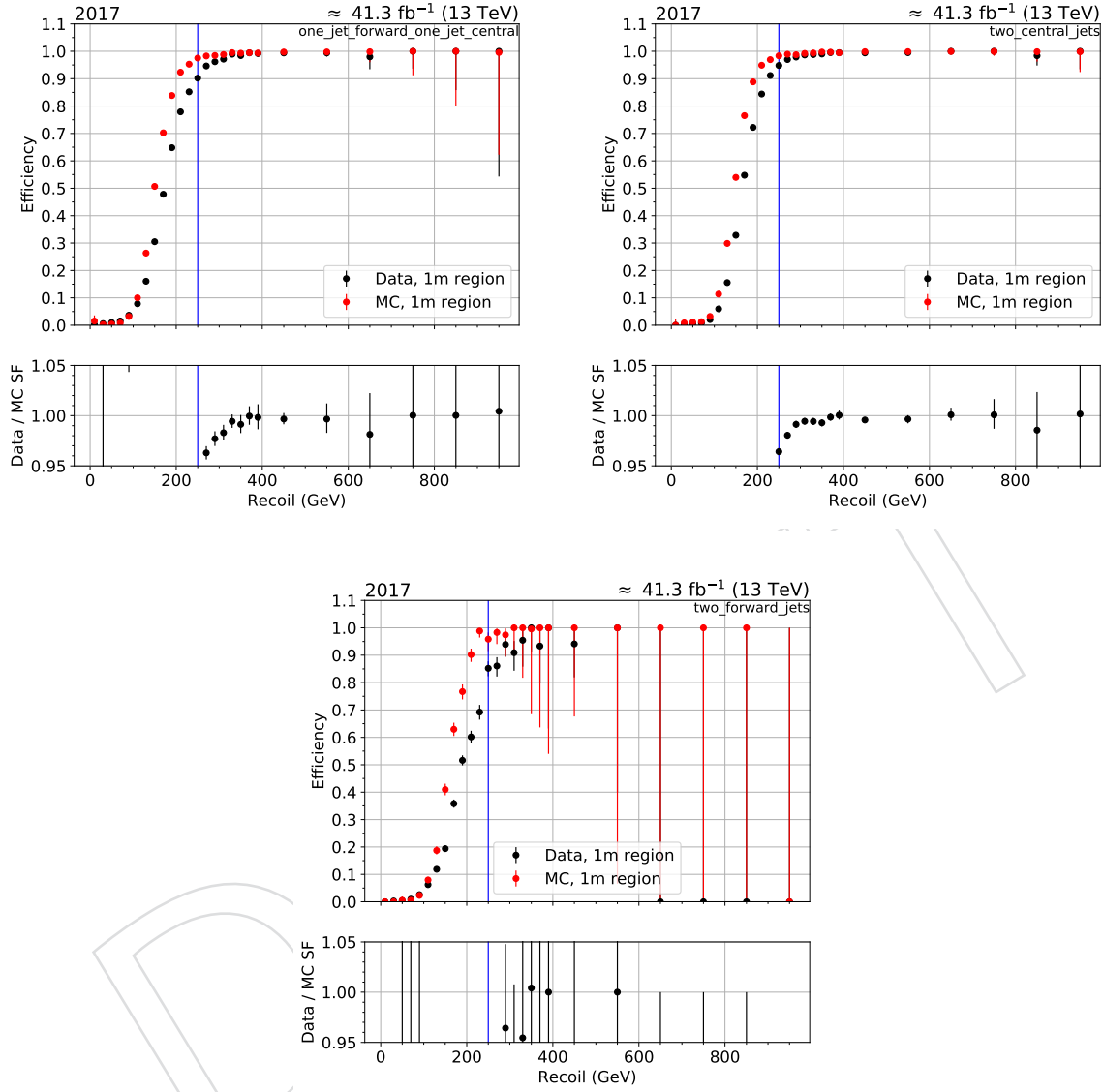


Figure 1: MET trigger efficiency as a function of recoil in three categories: One forward jet and one central jet, two central jets and two forward jets. These results are obtained from 2017 data and MC samples with the selection of single muon events.

¹⁴⁹ Using the measured efficiencies in data and MC, data-MC scale factors are measured for the
¹⁵⁰ three jet kinematic cases. Fig. 3 shows the scale factors as a function of recoil in single muon
¹⁵¹ control region, using 2017 (left) and 2018 (right) samples. We have low statistics for the two
¹⁵² forward jets category, but overall the scale factors are close to 1. The scale factors measured in
¹⁵³ the double muon region can be found in B.

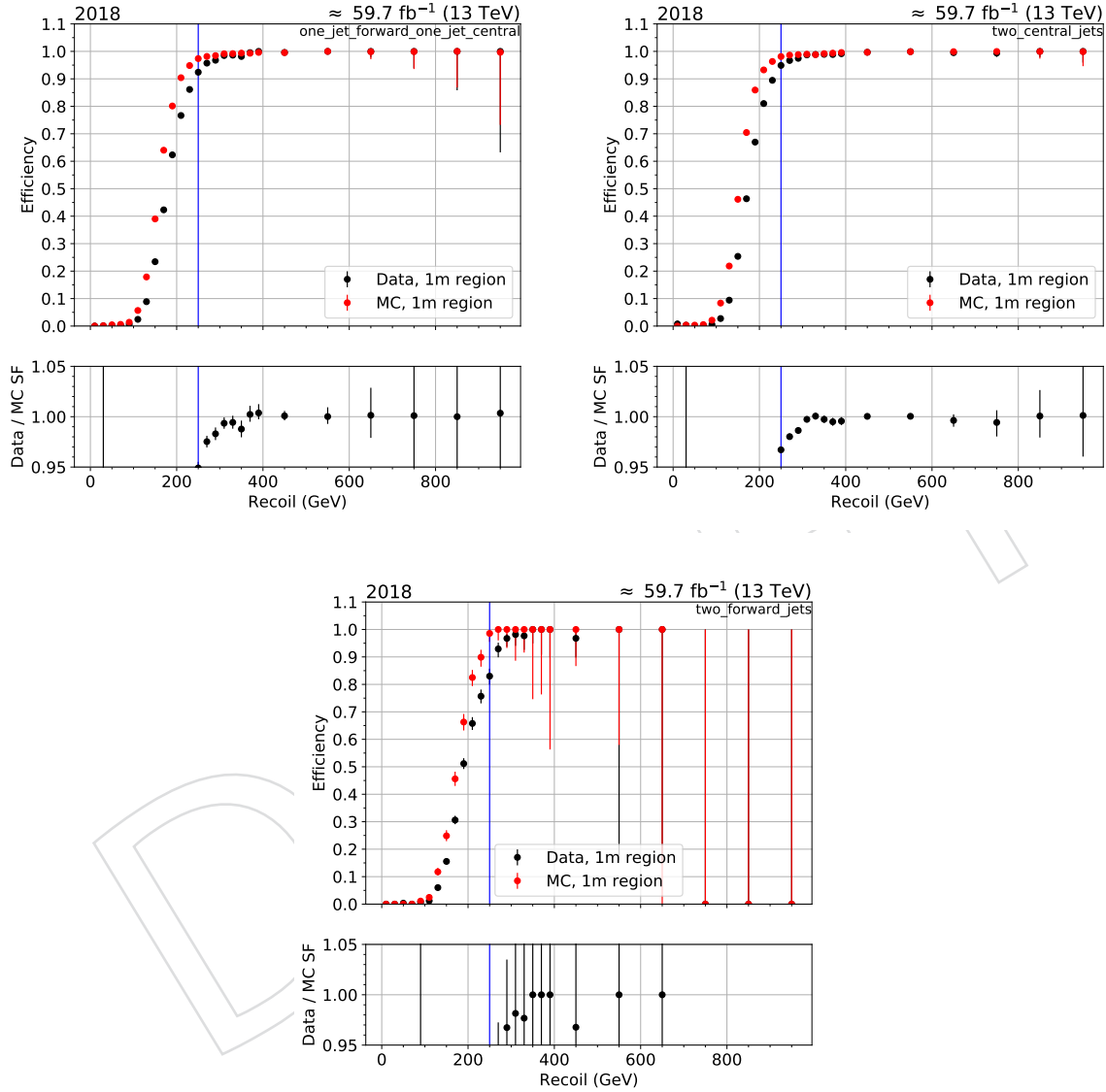


Figure 2: MET trigger efficiency as a function of recoil in three categories: One forward jet and one central jet, two central jets and two forward jets. These results are obtained from 2018 data and MC samples with the selection of single muon events.

154 **3.1.2 Photon trigger**

155 The photon trigger efficiency is measured using events from the JetHT dataset collected with
 156 the HLT_PFT1050 trigger, which was fully unprescaled in 2017 and 2018¹. Events are selected
 157 in the same way as for the photon analysis control region (cf. sec. 6.6), except for the photon
 158 p_T , recoil and trigger requirements. The trigger efficiency ϵ is then determined as:

$$\epsilon(\text{HLT_Photon200}) = \frac{\text{Offline selection \&& HLT_PFT1050 \&& HLT_Photon200}}{\text{Offline selection \&& HLT_PFT1050}}$$

159 The resulting efficiency in data and GJets H_T -binned simulation is shown in Fig. 4. The trigger
 160 efficiency in data is larger than 95% for a photon p_T of larger than 215 GeV, and larger than
 161 99% for photon p_T larger than 400 GeV. Between 250 and 400 GeV, there is a slight inefficiency
 162 amounting to approximately 1% at the most, with a larger amplitude in 2017 than in 2018. In
 163 both years, the turn-on behavior is almost immediate in simulated events, resulting in an MC-
 164 to-data scale factor almost entirely driven by the efficiency in data. The scale factor is within
 165 1% of unity for all bins except the lowest 2017 bin at 215 GeV, where it deviates from unity by
 166 about 4%.

167 Based on these results, the offline p_T cut for the photon in the photon control region is chosen
 168 to be 215 GeV.

169 **3.1.3 Electron trigger**

170 We also need to add information about the single electron trigger efficiencies

171 **4 Physics objects**

172 All physics objects are used to identify signal-like events, to suppress backgrounds and to de-
 173 fine control regions for background estimation. For the object definitions, we mostly follow the
 174 CMS POG endorsed recommendations. The physics objects and the selection requirements are
 175 described below.

¹The other, prescaled HLT_PFTXXXX paths yield lower statistical precision.

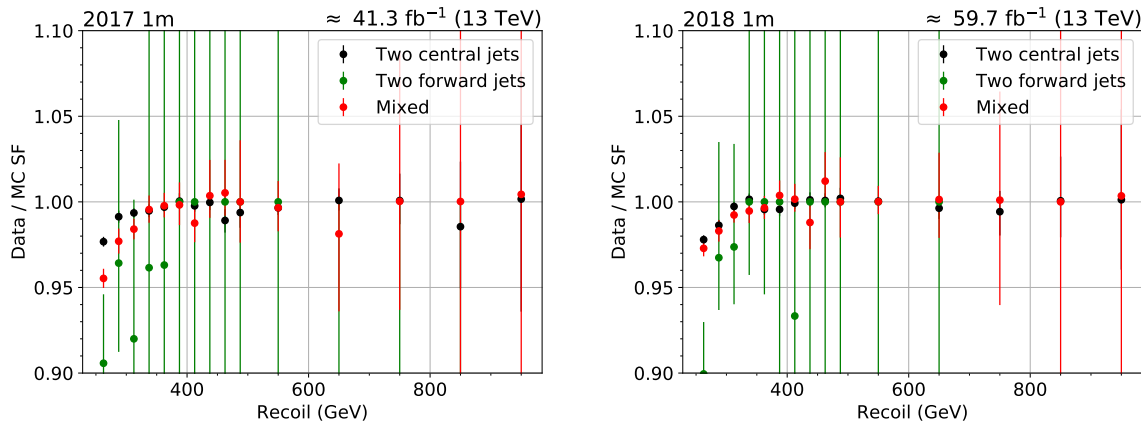


Figure 3: Data-MC scale factors for the three jet kinematic cases in the single muon control region, using 2017 (left) and 2018 (right) samples.

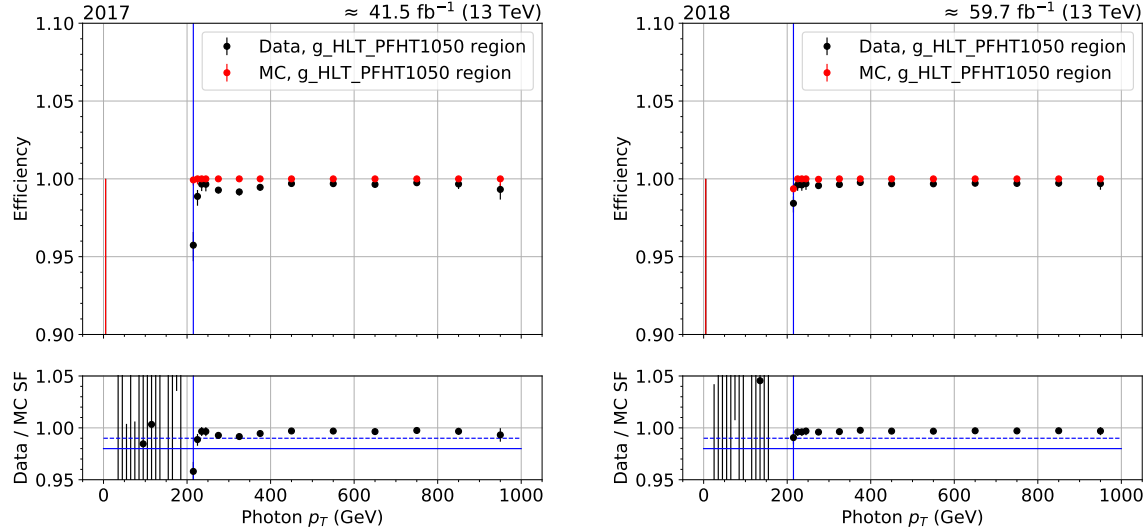


Figure 4: Efficiency of the `HLT_Photon200` trigger in data (black) and H_T -binned `GJets` simulation (red) for 2017 (left) and 2018 (right) as a function of photon p_T . The bottom panel shows the MC-to-data efficiency scale factor. The blue vertical line indicates a photon p_T of 215 GeV, which is the requirement used in the analysis selection.

176 4.1 Jets

177 In this analysis, jets are reconstructed by clustering PF candidates using the infrared and collinear
 178 safe anti- k_T algorithm [8]. Jets are clustered with a distance parameter of 0.4 and are referred
 179 to as AK4 jets. The reconstructed vertex with the largest value of summed physics-object p_T^2 is
 180 taken to be the primary pp interaction vertex. The physics objects are those returned by a jet
 181 finding algorithm [8, 9] applied to all charged PF candidates associated with the vertex, plus
 182 the corresponding associated missing transverse momentum.

183 Jet momentum is determined as the vector sum of all particle momenta in the jet, and is found
 184 from simulation to be within 5 to 10% of the true momentum over the full p_T spectrum and de-
 185 tector acceptance. An offset correction is applied to jet energies to take into account the contri-
 186 bution from additional proton-proton interactions within the same or nearby bunch crossings
 187 (pileup). Jet energy corrections are derived from simulation, and are confirmed with *in situ*
 188 measurements of the energy balance in dijet, multijet, γ +jet, and leptonic Z+jet events [10]. The
 189 Fall11_7_17Nov2017_V32 and Autumn18_V8 versions of the jet energy corrections are used for
 190 the 2017 and 2018 data sets, respectively.

191 The AK4 jets used in this analysis are required to pass loose jet identification criteria. In ad-
 192 dition, all the jets with p_T smaller than 50 GeV must pass the medium pileup ID criteria. This
 193 additional constraint on all AK4 jets is found to improve the modeling of jet distributions, es-
 194 specially in the horn regions near $|\eta| = 2.9$. The effect of this requirement is demonstrated in
 195 the sub-leading jet η distribution in Fig. 5.

196 In addition to the pileup ID requirement, JER corrections are applied to all AK4 jets. Appli-
 197 cation of this correction on all jets is observed to improve the modeling of the jets, especially
 198 near the horn regions near $|\eta| = 2.9$. The effect of JER corrections on the subleading jet eta
 199 distribution is shown in Fig. 6.

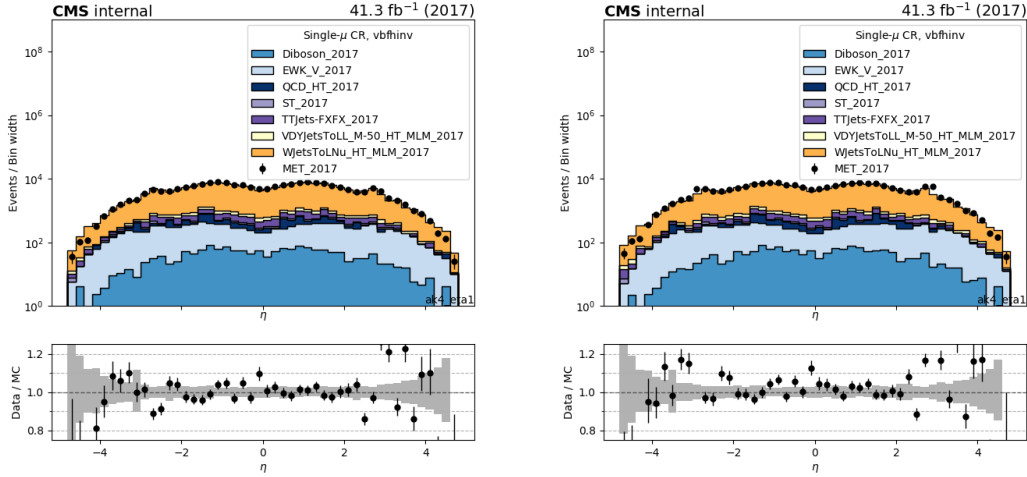


Figure 5: Subleading AK4 jet η distribution in single muon control region with pileup ID requirement (left) and without pileup ID requirement (right).

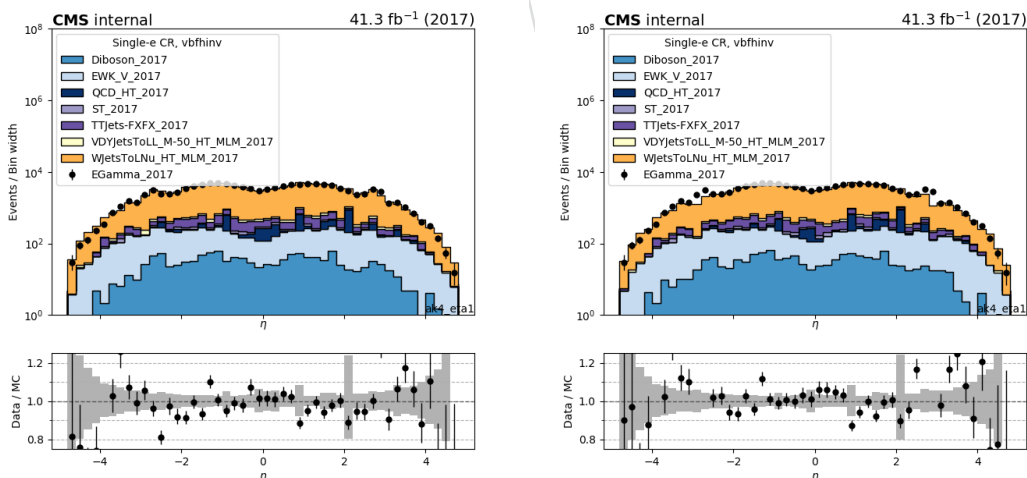


Figure 6: Subleading AK4 jet η distribution in single electron control region with JER corrections applied (left) and without JER corrections applied (right).

200 Lastly, to suppress the contributions due to non-collision backgrounds, the following require-
 201 ments are applied on the leading AK4 jet:

- 202 • Charged hadron energy fraction > 0.1
 203 • Neutral hadron energy fraction < 0.8

204 **4.1.1 b-tagged jets**

205 In this analysis b jets with $p_T > 20$ GeV and $|\eta| < 2.4$ are identified using the “DeepCSV”
 206 algorithm [11], adopting a working point (medium) corresponding to correctly identifying a
 207 b-jet with a probability of 80%, and misidentifying a light-flavor jet with a probability of 10%.
 208 This working point corresponds to the value of DeepCSV tagger to be greater than 0.4941.
 209 Events with identified b jets are rejected to reduce the contamination from top quark processes.

210 **4.2 Missing transverse momentum and recoil**

211 The vector \vec{p}_T^{miss} is defined as the imbalance in the transverse momentum of all particles that
 212 interact with the detectors. Due to momentum conservation in the plane transverse to the beam
 213 axis, \vec{p}_T^{miss} corresponds to the transverse momentum that is carried by undetected particles such
 214 as neutrinos. Practically, \vec{p}_T^{miss} is computed as the negative of the vectorial sum of transverse
 215 momenta of all PF candidates and is therefore also referred to as PF \vec{p}_T^{miss} . The magnitude of
 216 the \vec{p}_T^{miss} is referred to as p_T^{miss} .

217 Minimum energy thresholds in the calorimeters, inefficiencies in the tracker, nonlinearity of
 218 the response of the calorimeter for hadronic particles can lead to an over- or underestimation
 219 of p_T^{miss} . The bias on the p_T^{miss} measurement is reduced by propagating the effect of the jet
 220 energy corrections introduced in section 4.1 according to

$$\vec{p}_T^{\text{miss}}(\text{corr}) = \vec{p}_T^{\text{miss}} - \sum_{\text{jets}} (\vec{p}_{T,\text{jet}}(\text{corr}) - \vec{p}_{T,\text{jet}}), \quad (1)$$

221 where the “corr” refers to the scale energy corrected measurements of the related objects.

222 This “type-I” correction for \vec{p}_T^{miss} uses jet energy scale corrections for all corrected jets with
 223 $p_T > 15$ GeV that have less than 0.9 of their energy deposited in the ECAL. Furthermore, if a
 224 muon is found in a jet, its 4-momentum is subtracted from the 4-momentum of the jet when
 225 performing the correction and is added back to a corrected object.

Since signal events in this analysis contain only jets and no other reconstructed candidates, p_T^{miss} is equivalent to the total hadronic momentum in the event. For the leading backgrounds, this also corresponds to the transverse momentum of the W or Z boson. To mimic this behavior in the control regions of this analysis, the transverse momentum of the hadronic recoil \vec{U} , defined as the vectorial sum of the transverse momenta of all particles except the vector boson (or its decay products), is used. The variable is computed as

$$\vec{U} = \vec{p}_T^{\text{miss}} + \sum_{i \in \text{leptons, photons}} \vec{p}_T^i \quad (2)$$

226 where the sum takes into account the leptons and photons used to define the respective control
 227 region. The uncertainty of p_T^{miss} has a strong dependence on the event topology. Therefore,
 228 the uncertainty on p_T^{miss} is often factorized into its components of jets, leptons and unclustered
 229 energy. Each sub-component is then varied within its scale and resolution uncertainty. In this
 230 analysis, the largest contribution on the final p_T^{miss} uncertainty comes from the variations of the

jet energy scale correction and the magnitude of the uncertainty is estimated to be 4% for the $Z(\nu\nu) + \text{jets}$ events. This uncertainty is not the most recent one and it will be recalculated.

Anomalous high- p_T^{miss} events can appear due to various phenomena. In the ECAL, spurious deposits may appear due to particles striking sensors in the ECAL photodetectors, or from real showers with non-collision origins such as those caused by beam halo particles. ECAL dead cells can cause real energy to be missed, again leading to a spurious imbalance. In the HCAL, spurious energy can arise due to noise in the hybrid photodiode and readout box electronics, as well as direct particle interactions with the light guides and photomultiplier tubes of the forward calorimeter. A number of filters has been developed by the POG/DPG groups to identify and suppress anomalous high p_T^{miss} events [12]. The recommended filters are listed in Tab. 6 and are applied in the analysis.

Table 6: The p_T^{miss} filters recommended by the JME POG [12]. The recommendations apply to both 2017 and 2018. Except for the bad super cluster filter (“ee badSC”), all filters are applied both in data and simulation.

Filter	Name in NanoAOD	Applied in data (MC)
primary vertex filter	Flag_goodVertices	✓(✓)
beam halo filter	Flag_globalSuperTightHalo2016Filter	✓(✓)
HBHE noise filter	Flag_HBHENoiseFilter	✓(✓)
HBHEiso noise filter	Flag_HBHENoiseIsoFilter	✓(✓)
ECAL TP filter	Flag_EcalDeadCellTriggerPrimitiveFilter	✓(✓)
Bad PF Muon Filter	Flag_BadPFMuonFilter	✓(✓)
ee badSC noise filter	Flag_eeBadScFilter	✓(✗)
ECAL bad calibration filter update	Flag_ecalBadCalibFilterV2	✓(✓)

To further minimize the contribution of anomalous high- p_T^{miss} events (specifically due to spurious charged hadrons) in this analysis, a quantity based on the relative ratio of calorimetry based p_T^{miss} and PF based p_T^{miss} is employed. Events satisfying $|E_{\text{T calo}}^{\text{miss}} - E_{\text{T PF}}^{\text{miss}}|/U < 0.5$ are selected in this analysis.

4.3 Leptons

4.3.1 Electrons

Electrons within the geometrical acceptance of $|\eta| < 2.5$ are reconstructed by associating tracks reconstructed in the silicon detector with clusters of energy in the ECAL [13]. Well-identified electron candidates are required to satisfy additional identification criteria based on the shower shape of the energy deposit in the ECAL and the consistency of the electron track with the primary vertex [14]. Electron candidates that are identified as coming from photon conversions in the detector material are removed. An isolation variable is calculated based on the sum of the energies of the PF candidates within a cone of $\Delta R < 0.3$ around the electron. The mean energy deposit in the isolation cone of the electron coming from pileup is estimated following the method described in Ref. [13] and subtracted from the isolation sum. In this note, ‘veto’ [15] electrons with a minimum p_T of 10 GeV are selected with an average efficiency of 95% and their presence is used as a condition to reject events, whereas ‘tight’ [15] electrons with a minimum p_T of 40 GeV and an average efficiency of 70% are used to select the events in the control

260 regions. Full selection criteria are shown in Table 7.

Table 7: Tight and veto electron identification criteria.

Variable	Selection Tight	Selection Veto
	Barrel (Endcaps)	Barrel (Endcap)
Full 5x5 σ_{ijinj}	< 0.0104 (< 0.0353)	< 0.0126 (< 0.0457)
$ \Delta\eta_{in} $	< 0.00255 (< 0.00501)	< 0.00463 (< 0.00814)
$ \Delta\phi_{in} $	< 0.022 (< 0.0236)	< 0.148 (< 0.19)
H/E	$< 0.026 + 1.15/E_{SC} + 0.0324\rho/E_{SC}$ ($< 0.0188 + 2.06/E_{SC} + 0.183 * \rho/E_{SC}$)	$< 0.05 + 1.16/E_{SC} + 0.0324\rho/E_{SC}$ ($< 0.05 + 2.54/E_{SC} + 0.183\rho/E_{SC}$)
Relative isolation (ρ correction)	$< 0.0287 + 0.506/p_T$ ($< 0.0445 + 0.963/p_T$)	$< 0.198 + 0.506/p_T$ ($< 0.203 + 0.963/p_T$)
$1/E - 1/p$	< 0.159 (< 0.0197)	< 0.209 (< 0.132)
$ d_{xy}(\text{vtx}) $	< 0.050 (< 0.100)	< 0.050 (< 0.100)
$ d_z(\text{vtx}) $	< 0.100 (< 0.200)	< 0.100 (< 0.200)
Expected Inner Missing Hits	$<= 1$ ($<= 1$)	$<= 2$ ($<= 3$)
Pass conversion veto	Yes (Yes)	Yes (Yes)

261 4.3.2 Muons

262 Muons within the geometrical acceptance of $|\eta| < 2.4$ are reconstructed by combining information from the silicon tracker and the muon system [16]. The muons are required to pass set 263 of quality criteria based on the number of spatial points measured in the tracker and in the 264 muon system, the fit quality of the muon track and its consistency with the primary vertex 265 of the event. Similar to electron case, the isolation requirements for muons are also based on 266 the sum of the energies of the PF candidates, but a different cone size of a $\Delta R < 0.4$ is used. 267 The muon isolation variable is corrected for pileup effects by subtracting half of the sum of the 268 transverse momenta of charged particles that are inside the isolation cone and not associated 269 with the primary vertex. In this note, “loose” [17] muons with $p_T > 10$ GeV are selected with 270 an average efficiency of 98% and are used as a condition to reject events, whereas “tight” [18] 271 muons with $p_T > 20$ GeV are selected with an average efficiency of 95% and are used to select 272 events in the control samples. A full list of tight identification criteria is given here: 273

- 274 • Muon reconstructed as a global muon
- 275 • Muon reconstructed as a particle flow muon

- 276 • Normalized χ^2 of the global track less than 10
- 277 • At least one muon chamber hit included in the global track fit
- 278 • Muon segments in at least two muon stations
- 279 • Transverse impact parameter w.r.t. the primary vertex less than 2 mm.
- 280 • Longitudinal impact parameter w.r.t. the primary vertex less than 5 mm.
- 281 • At least one pixel hit
- 282 • Hits on at least 5 tracker layers
- 283 • $\Delta\beta$ relative isolation less than 0.15

284 4.3.3 Taus

285 Hadronically decaying τ leptons are required to pass identification criteria using the hadron-
 286 plus-strips algorithm [19]. The algorithm identifies a jet as an hadronically decaying tau lepton
 287 candidate if a subset of the particles assigned to the jet is consistent with the decay products
 288 of a τ candidate. Candidate τ jets are required to pass both the “DecayModeNewDMs” and
 289 “DecayMode” identifiers.

290 In addition, τ candidates are required to be isolated from other activity in the event. The isolation
 291 requirement is computed by summing the p_T of the charged PF candidates and PF photon
 292 candidates within an isolation cone of $\Delta R = 0.5(0.3)$, around the tau candidate direction. The
 293 charged and photon candidates associated with the tau candidate are removed from this sum
 294 and further described in Ref. [19]. The “VLoose_IsolationMVArun2v1DBnewDMwLT” isolat-
 295 ion working point [20] is employed in this analysis for tau candidates with p_T larger than
 296 18 GeV within $|\eta| < 2.3$.

297 4.4 Photons

298 Photon candidates are reconstructed from energy deposits in the ECAL using algorithms that
 299 constrain the clusters to the size and shape expected from a photon [21]. The identification of
 300 the candidates is based on shower-shape and isolation variables. For isolated photons, scalar
 301 sums of the p_T of PF candidates within a cone of $\Delta R < 0.3$ around the photon candidate are
 302 required to be below the bounds defined. Only the PF candidates that do not overlap with the
 303 EM shower of the candidate photon are included in the isolation sums.

304 Two candidate definitions are employed. “Loose” photons are used to reject events with un-
 305 wanted photons. These photons are required to pass the EGamma POG ‘loose’ identification
 306 criteria [22], have a transverse momentum of at least 15 GeV and be within $|\eta| < 2.5$. The exact
 307 identification criteria are summarized in Table 8. A “tight” photon definition is used for the
 308 photon in the dedicated photon control region. These photons are required to be in the barrel
 309 ($|\eta| < 1.479$), and have $p_T > 215$ GeV. The POG medium ID is employed, which is summarized
 310 in Table 9.

311 4.4.1 Photon purity studies

312 Photons are reconstructed from ECAL clusters, and can be discriminated from other sources of
 313 ECAL deposits due to the properties of the cluster, as well as their lack of other associated sig-
 314 natures such as tracks or HCAL deposits. This discrimination is not perfect, however, and in
 315 some cases, non-photon objects will incorrectly be identified as photons (“fakes”). The leading
 316 source of fake photons is QCD production of multijet events, where a jet is misidentified. This
 317 process is relevant mainly because of its large cross-section, which yields non-negligible con-
 318 tributions to the photon selection even if the per-jet probability of misreconstruction is small.

Variable	Selection Barrel (Endcap)
Full 5x5 $\sigma_{i\eta i\eta}$	$< 0.0106 (< 0.0272)$
H/E	$< 0.04596 (< 0.0590)$
charged hadron isolation	$< 1.694 (< 2.089)$
neutral hadron isolation	$< 24.032(19.722) + 0.01512(0.0117) \times p_T + 2.259(2.3) \times 10^{-5} \times p_T^2$
photon isolation	$< 2.876(4.162) + 0.004017(0.0037) \times p_T$
Conversion safe electron veto	Yes (Yes)

Table 8: Loose photon identification criteria.

Variable	Selection Barrel
Full 5x5 $\sigma_{i\eta i\eta}$	< 0.01015
H/E	< 0.02197
charged hadron isolation	< 1.141
neutral hadron isolation	$< 1.189 + 0.01512 \times p_T + 2.259 \times 10^{-5} \times p_T^2$
photon isolation	$< 2.08 + 0.004017 \times p_T$
Conversion safe electron veto	Yes

Table 9: Tight photon identification criteria. The criteria are only given for the barrel region since endcap photons are not taken into account.

319 To estimate the fake contribution to the photon control region, a purity measurement is per-
 320 formed. The photon purity is defined as the fraction of reconstructed photons that is actually
 321 due to an isolated photon from the hard scattering event, as opposed to a fake. The purity is
 322 obtained from a template fit to the distribution of the $\sigma_{i\eta i\eta}$ variable in data, which $\sigma_{i\eta i\eta}$ vari-
 323 able represents the width of the ECAL shower in the η direction. Due to the different shower
 324 behavior of photons and hadrons, the $\sigma_{i\eta i\eta}$ distribution shows characteristically different be-
 325 havior between these two classes of reconstructed photons: Real photons show a large peak
 326 with a cut-off around $\sigma_{i\eta i\eta} \approx 0.01$, while fake photons will have a smaller peak (stemming from
 327 actual photons inside jets), and an additional non-peaking bulk region at larger $\sigma_{i\eta i\eta}$ (stemming
 328 from hadrons interacting in the ECAL). The inputs to the fit are defined as follows:

- 329 • Photons in data are selected by applying the same identification criteria as for the
 330 tight selection defined above, with the exception of the $\sigma_{i\eta i\eta}$ requirement. By remov-
 331 ing this requirement, the full $\sigma_{i\eta i\eta}$ distribution can be observed.
- 332 • A real photon template is obtained from GJETS simulation. The same identification
 333 criteria are applied as in data.
- 334 • A fake photon template is obtained from data. In this case, the identification criteria
 335 are modified by requiring that at least one of the isolation criteria is not passed.
 336 Therefore, the photons in this template do not overlap with the the ‘data’ template,
 337 and represent reconstructed photons inside jets.

338 The templates are derived in separate bins of the photon p_T and the measurement is performed
 339 separately for 2017 and 2018. Events are selected using the following criteria:

- 340 • At least one jet with $p_T > 100$ and $|\eta| < 2.4$, which is not overlapping with a photon
 341 of interest.
- 342 • The event must pass the HLT_Photon200 trigger, as well as the MET filters.

5. Reweighting of simulated events

17

- 343 • The event must have $p_T^{\text{miss}} < 60 \text{ GeV}$.

344 The fits are shown in Figs. 7 and 8, and the resulting purity as a function of photon p_T is shown
 345 in Fig. 9. While the fits are performed in the full range of $\sigma_{\eta\eta\eta} < 0.15$, the purity is evaluated
 346 only taking into account the contributions with $\sigma_{\eta\eta\eta} < 0.01015$, which is the requirement posed
 347 in the identification criteria used in the analysis. The resulting purity ranges between 2 and 4%,
 348 with a decreasing trend with photon p_T .

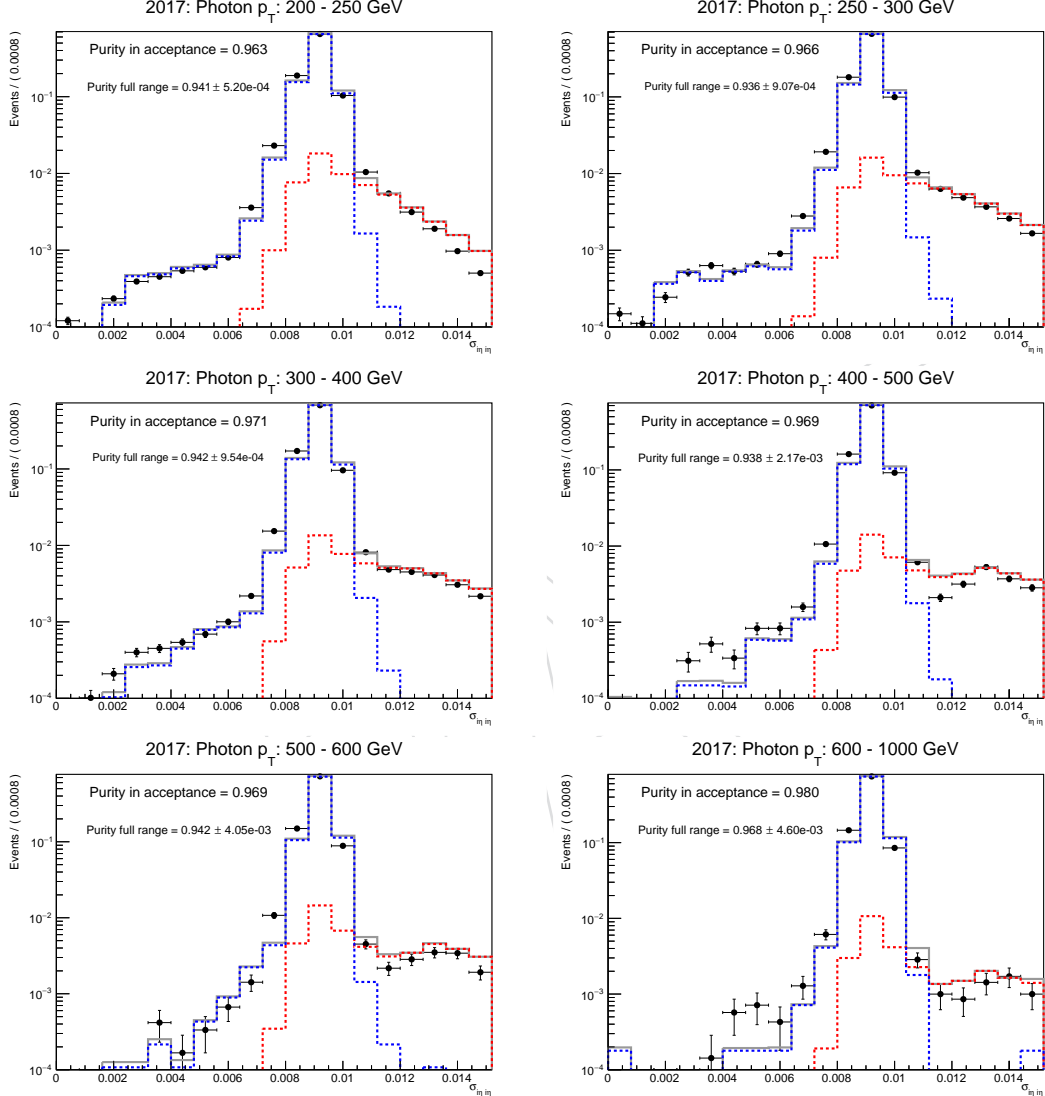


Figure 7: Template fits used to determine the photon purity in the 2017 dataset. The fits are shown in bins of photon p_T , increasing from left to right and top to bottom.

349 5 Reweighting of simulated events

350 Simulated signal and background samples are corrected for various effects through reweighting
 351 procedures outlined in this section.

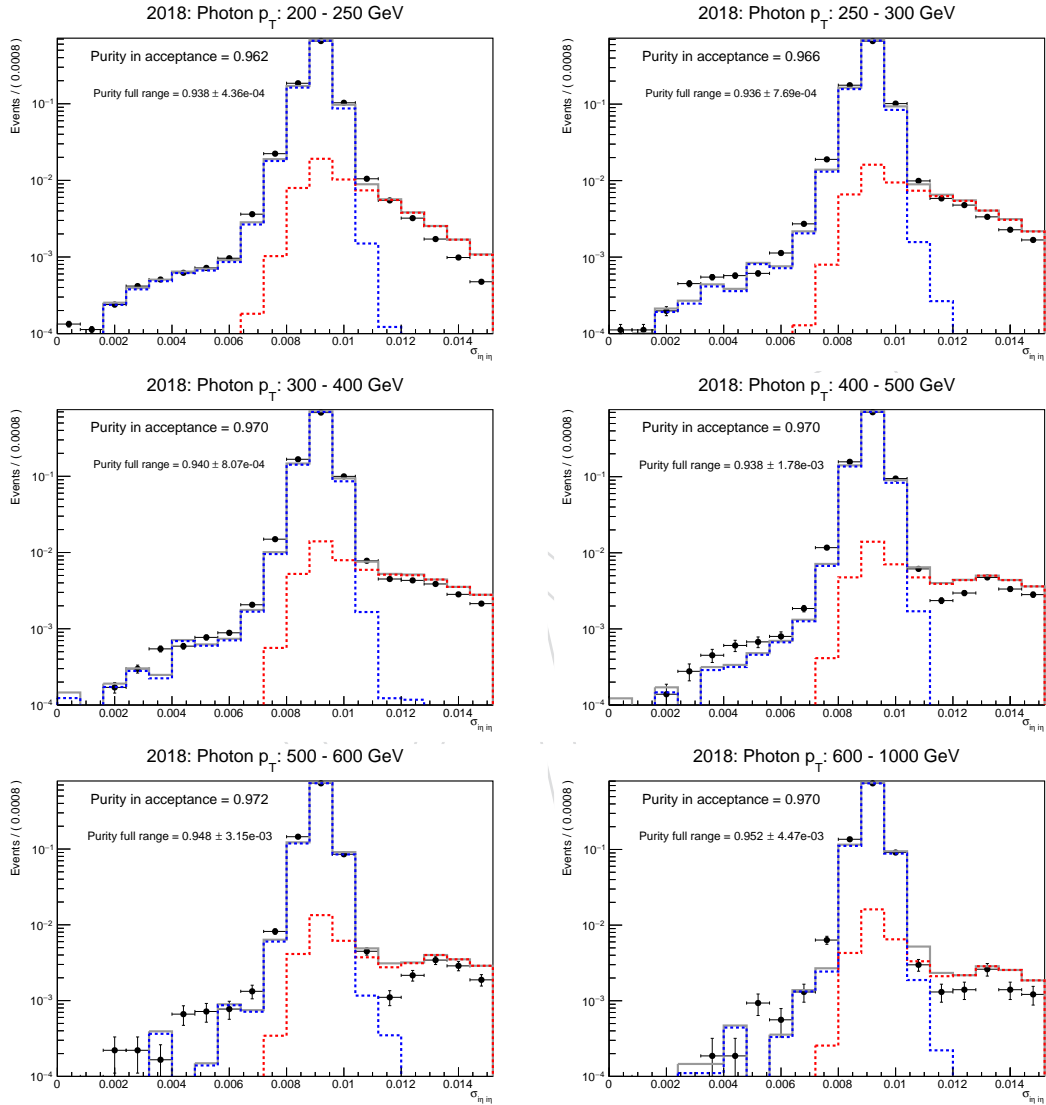


Figure 8: Template fits used to determine the photon purity in the 2018 dataset. The fits are shown in bins of photon p_T , increasing from left to right and top to bottom.

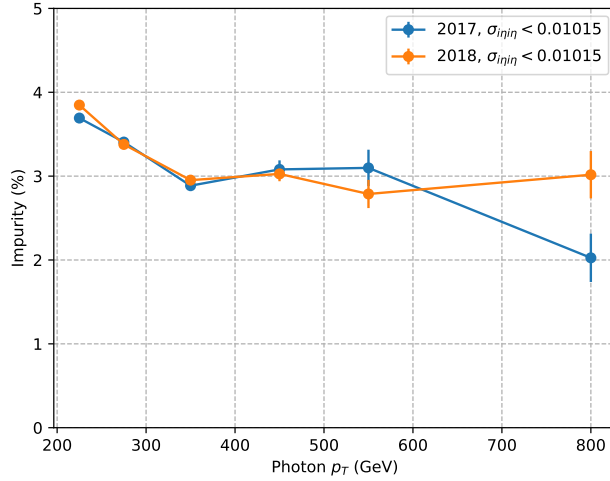


Figure 9: Photon purity as a function of photon p_T . This figure shows the aggregated results obtained from the fits shown in Figs. 7 and 8.

352 5.1 Trigger efficiency reweighting

353 The efficiency is calculated as a function of the recoil and M_{jj} . The trigger is found to be more
 354 than 95% efficient for events with a recoil larger than 250 GeV, and more than 99% efficient for
 355 events with a recoil larger than 375 GeV. The MC-to-data scale factor is found to be within 1%
 356 of unity everywhere except for the lowest recoil bin at 250 GeV, where it is within 2% (c.f. sec.
 357 3.1).

358 5.2 Pileup reweighting

359 The pileup (PU) conditions in the simulated samples are not identical to the ones observed
 360 measured in data, and a reweighting is applied to remove the difference. The reweighting is
 361 performed by matching the true pileup distribution of each simulated sample with the pileup
 362 distribution in data, obtained through the pileupCalc tool assuming a minimum bias cross
 363 section of $69.2 \pm 4.6\%$ mb, following the recommendations in Ref. [23]. The true pileup dis-
 364 tributions in data and simulation are shown in Fig. 10. The distribution of the number of
 365 reconstructed vertices for $W \rightarrow \mu\nu$ events before and after PU reweighting is shown in Fig. 11.
 366 In this variable, the PU reweighting method leads to a worse overall agreement between data
 367 and simulation. To check this behavior, the distribution of the event energy density ρ is shown
 368 in Fig. 11, again before and after PU reweighting. Here, the agreement before PU reweighting
 369 is worse than in the primary vertex distribution and the PU reweighting clearly improves the
 370 agreement.

371 5.3 Lepton and photon identification/reconstruction efficiency reweighting

372 Data-to-simulation scale factors are applied to events in the control regions to account for dif-
 373 ferences in the reconstruction, identification and isolation of leptons between data and simu-
 374 lationn. These data-to-MC scale factors are derived from the efficiencies that are measured for
 375 the electron and muon selections in bins of p_T and η in both data and simulation. These scale
 376 factors are provided by the relevant POGs.

377 The reconstruction scale factors for electrons are shown in Fig. 13. The corresponding identifi-
 378 cation scale factors for veto and tight electrons are shown in Fig. 14, and include the effect of

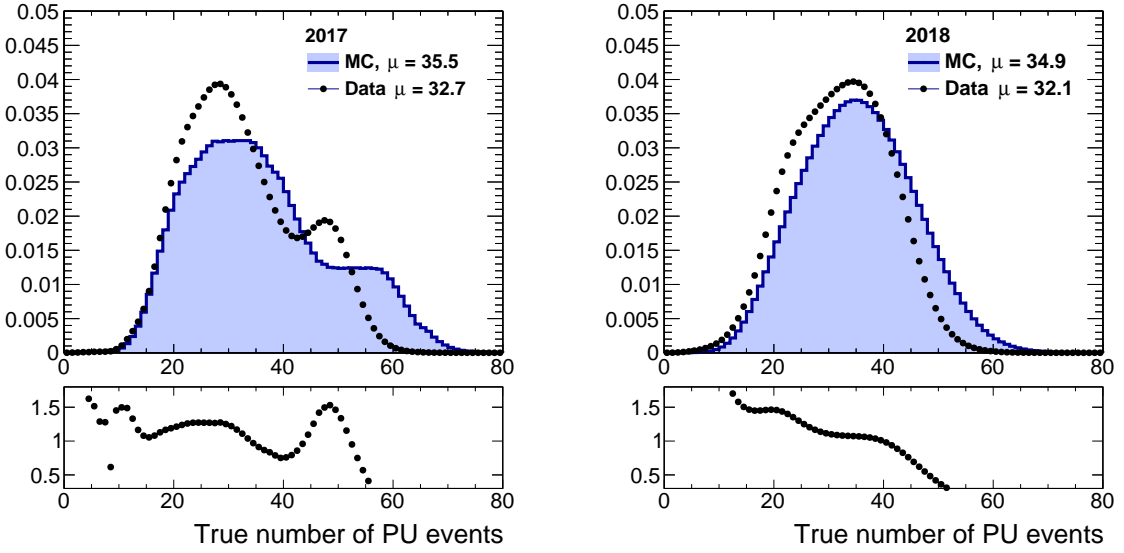


Figure 10: Distribution of the true number of PU events in data and simulation for 2017 (left) and 2018 (right). The distributions for data are extracted assuming a minimum bias cross section of 69.2 mb.

- 379 the isolation efficiency.
- 380 The identification scale factors for muons are shown in Fig. 15. Here, isolation scale factors
- 381 are applied separately and are shown in Fig. ???. The corresponding corrections for muons are
- 382 deemed negligible [24].
- 383 The scale factors for id and isolation for tight muons are shown in Fig. ???.

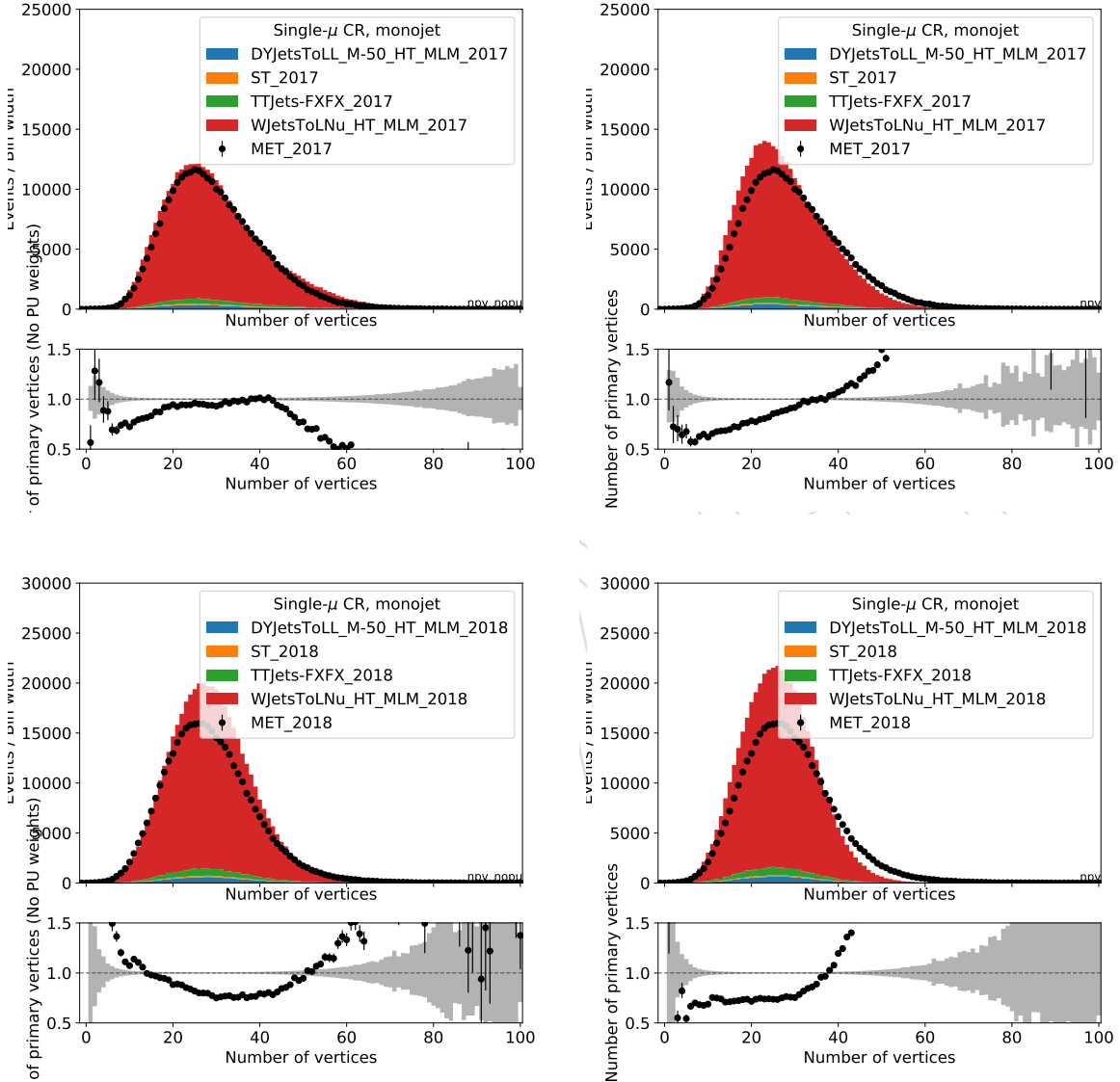


Figure 11: Distribution of the number of vertices in $W \rightarrow \mu\nu$ events in data and simulation before pileup re-weighting (left) and after pileup reweighting (right). The Monte Carlo is normalized to the luminosity of 41.53 and 59.7 fb^{-1} , respectively for 2017 and 2018.

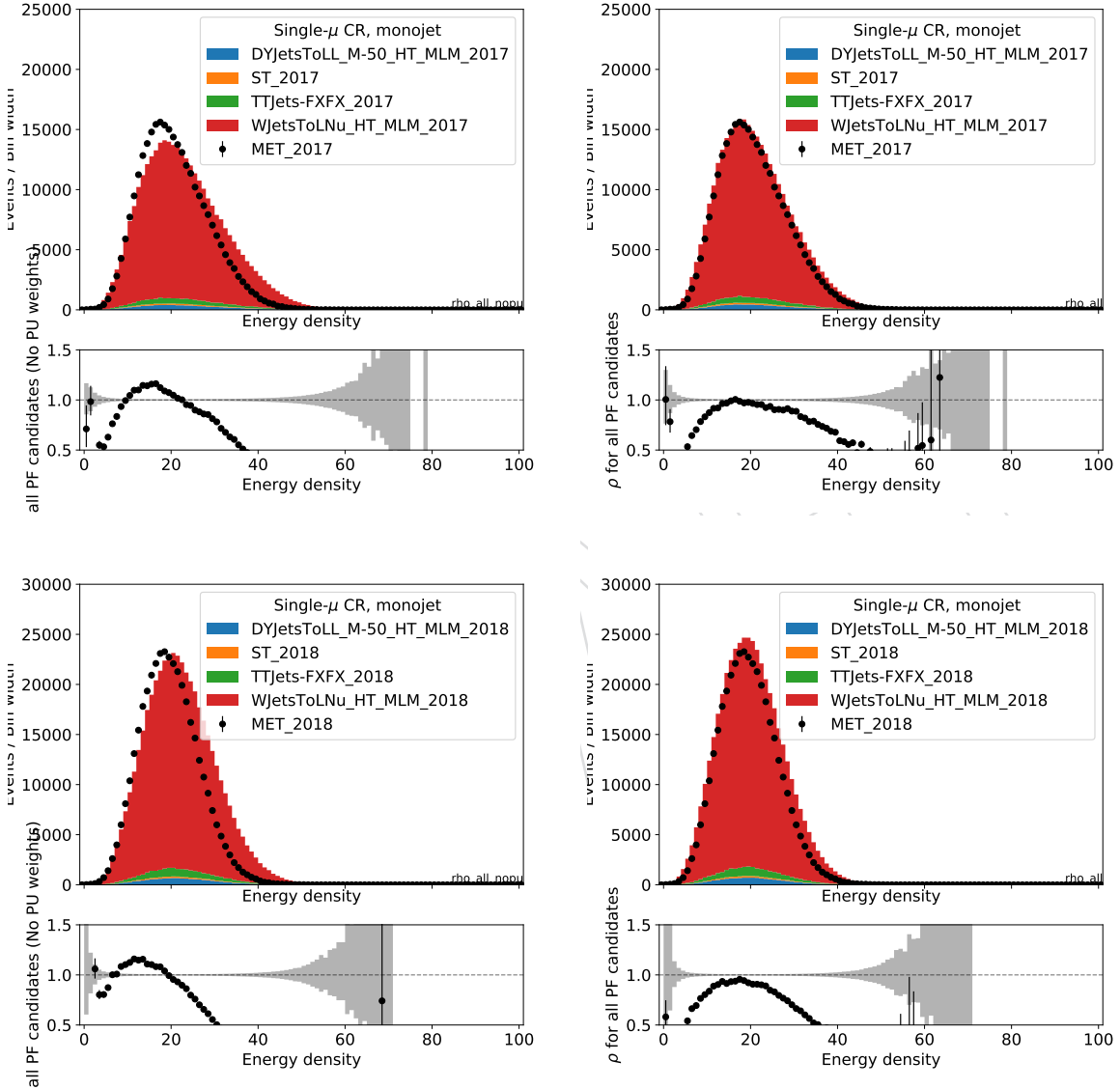


Figure 12: Distribution of the event energy density ρ in $W \rightarrow \mu\nu$ events in data and simulation before pileup re-weighting (left) and after pileup reweighting (right). The Monte Carlo is normalized to the luminosity of 41.53 and 59.7 fb^{-1} , respectively for 2017 and 2018.

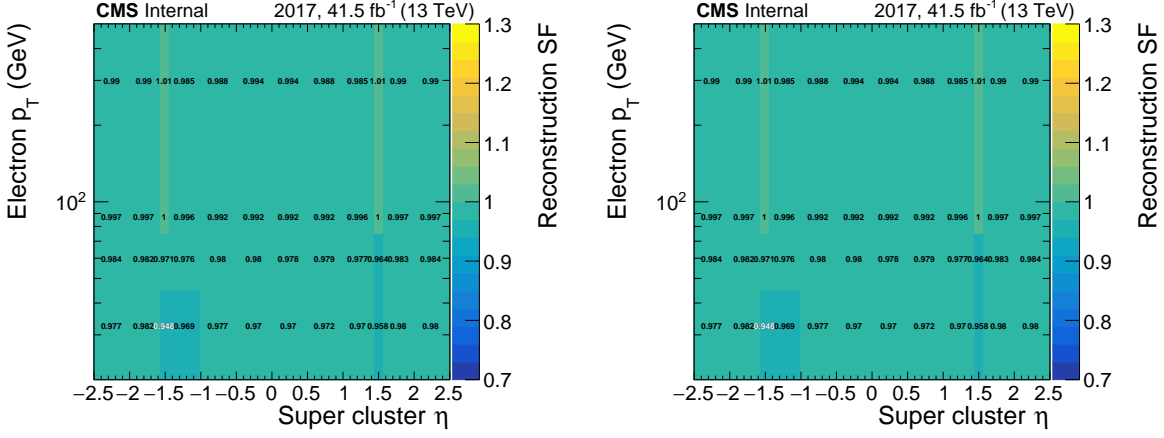


Figure 13: Scale factors for the reconstruction efficiency of electrons starting from a super cluster for 2017 (left) and 2018(right)

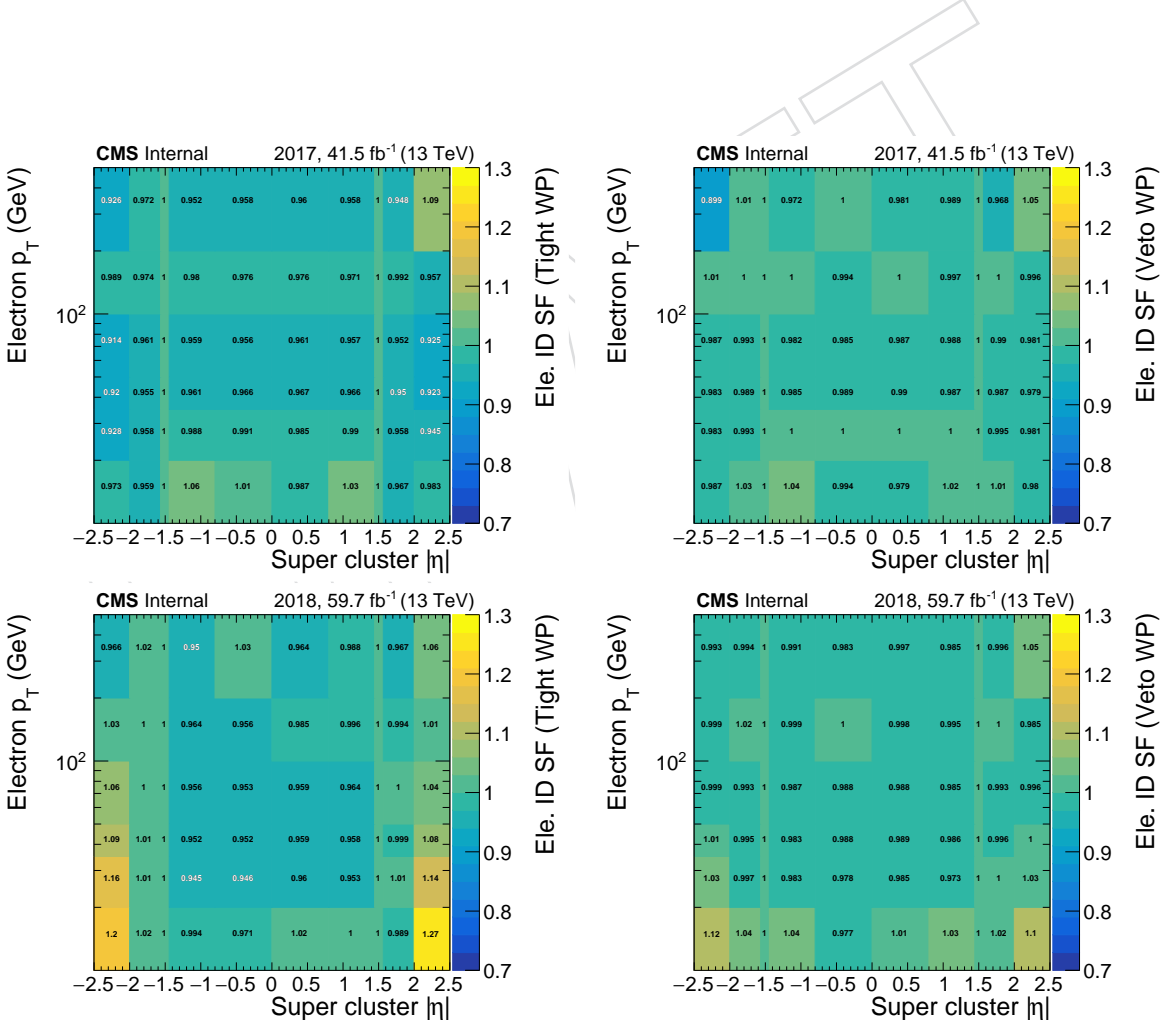


Figure 14: Scale factors for tight (left) and veto (right) electrons are shown for 2017 (top) and 2018 (bottom). The scale factors are provided in bins of electron p_T and η .

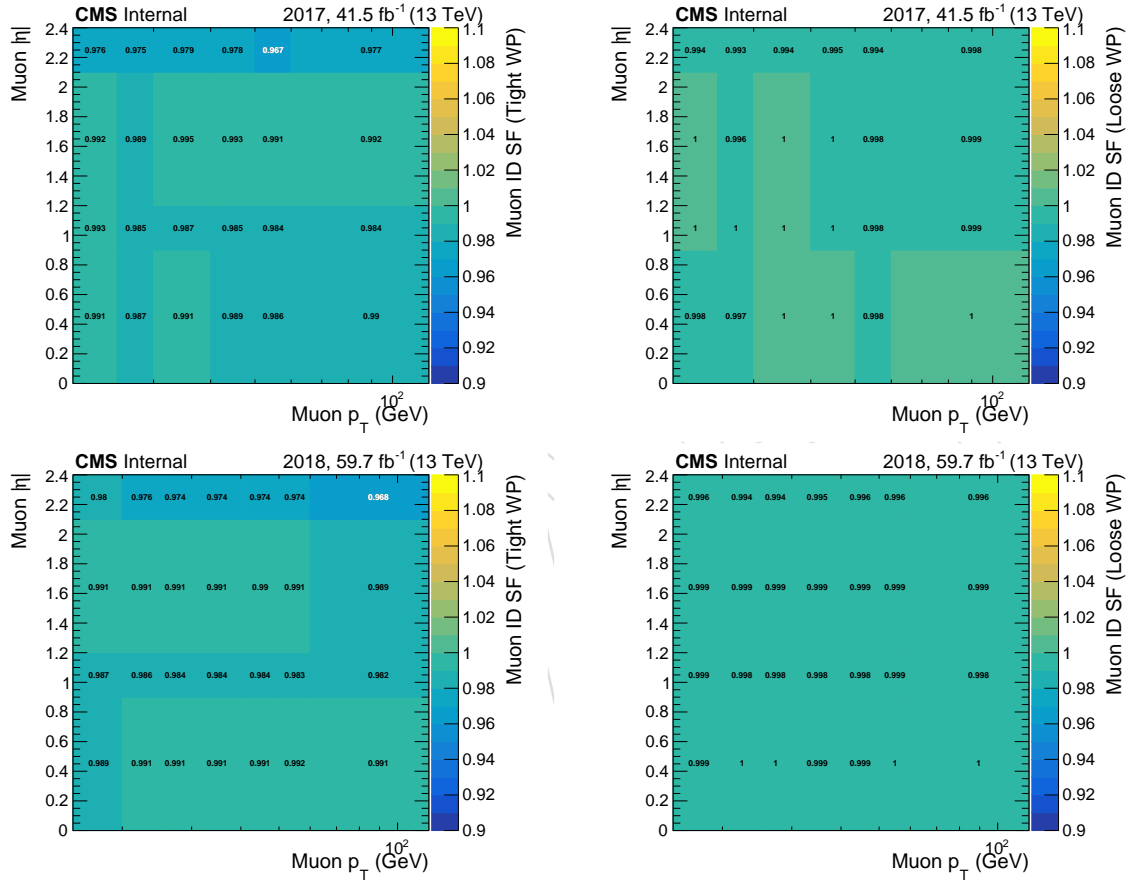


Figure 15: Scale factors for tight (left) and veto (right) muon identification are shown for 2017 (top) and 2018 (bottom). The scale factors are provided in bins of electron p_T and η .

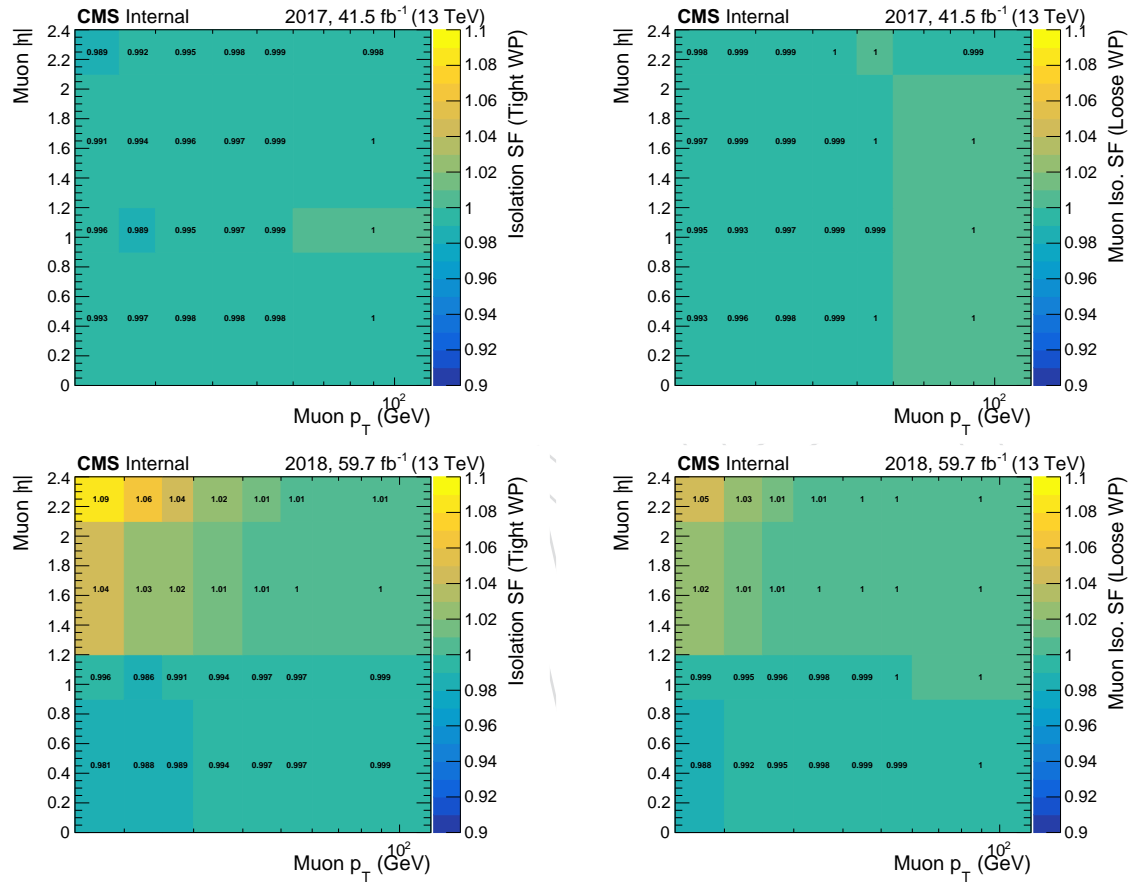


Figure 16: Scale factors for tight (left) and veto (right) muon isolation are shown for 2017 (top) and 2018 (bottom). The scale factors are provided in bins of electron p_T and η .

384 **5.4 Higher-order reweighting**

385 This analysis uses the ratios of the recoil distributions in signal and control regions to con-
 386 strain the final background estimate in a partially data driven way. As signal and control re-
 387 gions both have large statistical power, precise predictions of these ratios are necessary. To
 388 achieve this goal, the LO simulation samples for the samples W, DY and photon backgrounds
 389 are reweighted using higher-order corrections separately corresponding to NLO QCD, NLO
 390 EW and NNLO QCD terms. The individual corrections are described in more detail in this
 391 section. A concise overview of which corrections are applied to which processes is given in
 392 Tab. 10.

Table 10: Summary of higher-order corrections applied to simulated samples. For each boson production process, separate samples and corrections are available for the EWK and QCD production modes. “MC order” reflects the perturbative order used in the generation of the simulation sample, while the further columns represent corrections applied on a per-event level in the analysis process.

Boson	production mode	MC order	NLO QCD	NNLO QCD	NLO EWK
Z	QCD	LO	✓	✓	✓
	EWK	LO	✓	–	–
W	QCD	LO	✓	✓	✓
	EWK	LO	✓	–	–
γ	QCD	LO	✓	✓	✓
	EWK	LO	–	–	–

393 **5.4.1 Generator-level boson construction**

394 All theory-based corrections of the W, DY and photon backgrounds are parametrized as a func-
 395 tion of the generator-level p_T of the respective boson $p_{T,V}$. For each simulated event, this quan-
 396 tity is calculated as follows. For DY and W samples, generator-level dilepton candidates are
 397 built from:

- 398 1. “dressed” final-state electrons and muons. Lepton dressing means to collect all photons
 399 radiated off the lepton within a cone of $\Delta R < 0.1$ and adding their four-momenta back
 400 to the lepton four-momentum. This procedure is meant to undo the effect of final state
 401 photon radiation, which would otherwise distort the value of the reconstructed boson
 402 four-momentum. This effect is especially relevant as electrons and muons follow differ-
 403 ent radiation patterns. Lepton dressing is performed in central NanoAOD production
 404 following the procedure used in the RIVET software.
- 405 2. τ leptons with generator status 2. As τ leptons are unstable, they are not present as final
 406 state particles (status 1) in the generator record. The τ lepton before its decay has status
 407 2.
- 408 3. neutrinos with generator status 1.

409 The dilepton candidates are checked for flavour consistency with the desired boson candidate.
 410 If multiple candidates are found in an event, the one with the highest invariant mass is used.
 411 For photon events, the generator photon with highest p_T and status 1 is used.

412 5.4.2 QCD NLO corrections to QCD V processes

413 Scale factors corresponding to NLO QCD corrections for W and Z production are obtained
 414 from central CMS. For the DY and W processes, samples from “Fall17” campaign, while “Sum-
 415 mer16” samples are used for the γ +jets process. In both cases, all samples are generated using
 416 `MadGraph5_amc@NLO`. The LO samples are binned in HT and are equivalent to the ones used
 417 in the analysis, and are generated with up to four partons in the matrix element. The NLO
 418 samples are generated with up to two additional partons in the matrix element calculation.
 419 Further jet multiplicities are handled by the parton shower, which in both cases is performed
 420 using `Pythia8` with tune `CP5`.

421 The scale factors are derived by obtaining the distribution of interest at the generator-level in
 422 both samples, normalizing the distributions to their respective cross sections, and then divid-
 423 ing them as $SF = NLO / LO$. Identical selection criteria are applied to both samples based on
 424 the generator-level boson and generator-level AK4 jets, which are clustered using all visible
 425 generator particles with status 1. The requirements are:

- 426 1. At least two generator-level jets, with the leading (trailing) p_T of at least 80 GeV (40 GeV)
 427 and $|\eta| < 4.7$.
- 428 2. The two leading jets must be in opposite hemispheres of the detector, $\eta_1 \times \eta_2 < 0$.
- 429 3. The difference in the azimuthal angle ($\Delta\phi$) between the boson and the four leading jets in
 430 the event is required to be larger than 0.5. Only jets with $p_T > 30$ GeV are considered.

431 Compared to an inclusive derivation of the SF, the inclusion of the selection criteria leads to an
 432 increase in the value of the SF of about 10 – 12%.

433 The scale factors are derived either as a one-dimensional function of the generator-level boson
 434 $p_{T,V}$ (“1D”) or two-dimensionally in $p_{T,V}$ and M_{jj} (“2D”).

The 1D SFs are shown in Fig. 17. To protect the outcome of the reweighting procedure from
 binning effects, the binned scale factor is interpolated using a falling exponential function:

$$SF = a \times \exp(-b \times p_T) + c, \quad (3)$$

435 where p_T is the boson transverse momentum and a , b and c are determined by a fit to the scale
 436 factor histogram. The resulting values of the fit parameters, as well as the resulting interpolated
 437 shape are also shown in Fig. 17.

438 The 2D versions of the SFs are only derived for the W and DY processes, for which the available
 439 simulation samples are bigger and thus allow for finer binning. The scale factors are shown in
 440 Fig. 18.

441 5.4.3 QCD NNLO corrections to QCD V processes

442 NNLO corrections are obtained from the fixed-order calculations results in [25]. They are
 443 parametrized as a function of the generator-level boson p_T . The correction is shown in Fig. 19.

444 5.4.4 EW NLO corrections to QCD V processes

445 Scale factors corresponding to NLO EW corrections are obtained from Ref. [25] and applied as
 446 a function of the generator-level boson p_T . The scale factors are shown in Fig. 20.

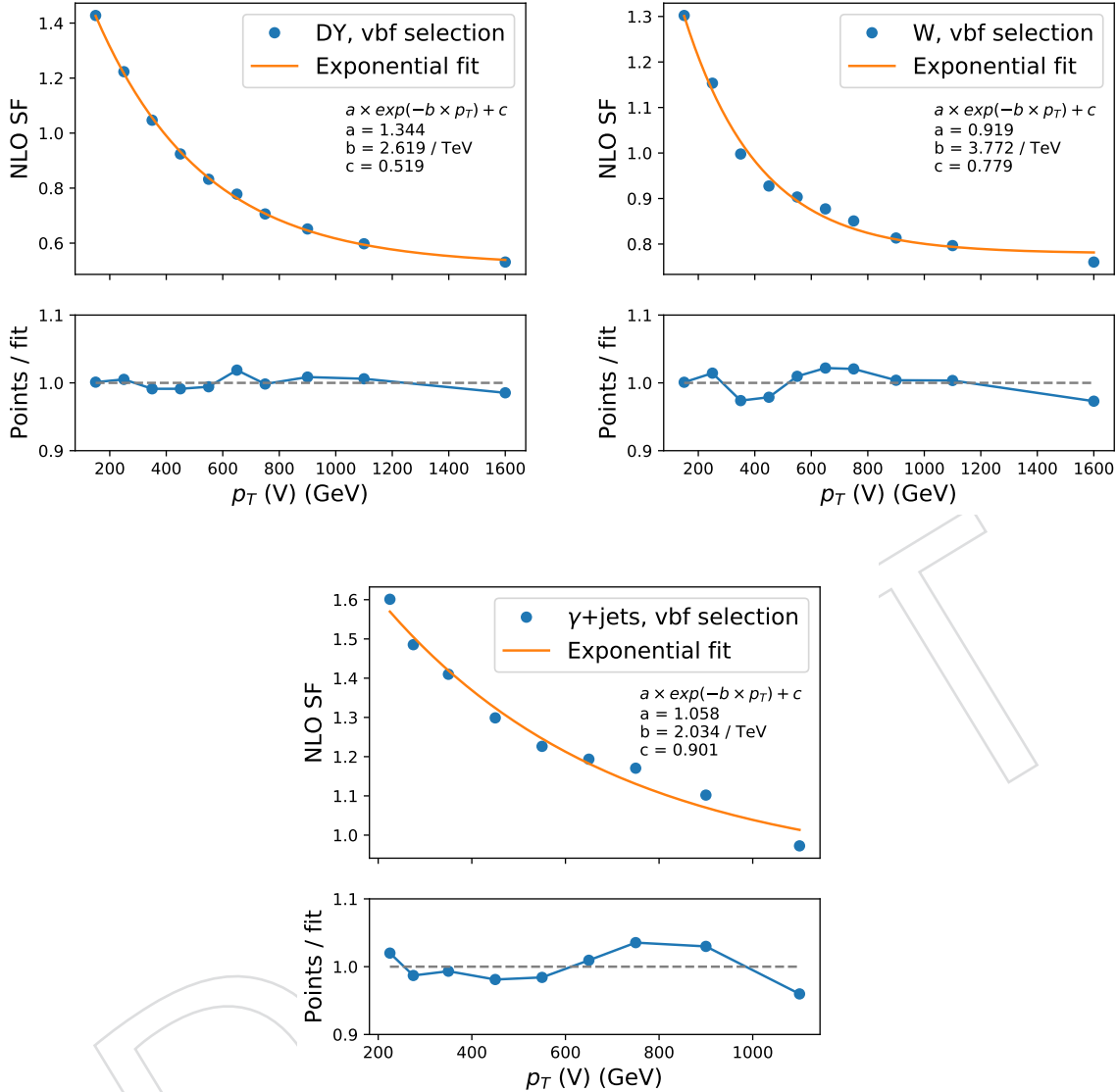


Figure 17: QCD NLO scale factors for the DY (top left), W (top right) and γ +jets processes. The k factors are derived within the generator-level VBF selection described in the text. In the top panel of each plot, the blue markers show the NLO SF derived from the simulated samples. The orange line shows a fit function used to interpolate the SF. The functional form and resulting parameters are given in the figure. In the bottom panel, the blue markers show the ratio of the histogram to the fit result in each bin.

447 5.4.5 QCD NLO corrections to EWK V processes

448 The QCD NLO corrections to EWK W and Z production have been calculated in Ref. [26] using
 449 the VBF@NLO program. They are parametrized in $p_{T,V}$ and M_{jj} and are shown in Fig. 21.

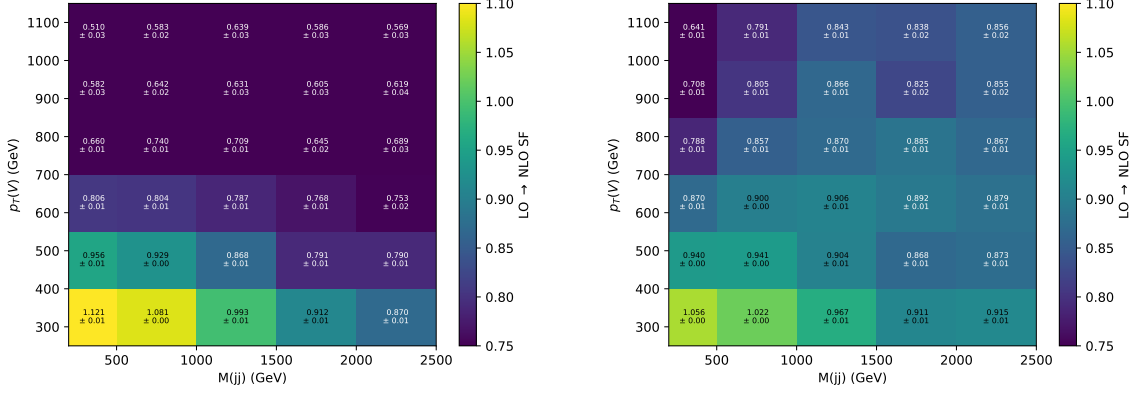


Figure 18: Same as Fig. 17, but now binned in two dimensions of the generator-level boson p_T and M_{jj} . The k factors are derived within the generator-level VBF selection described in the text. The uncertainties quoted in each bin are the statistical uncertainties due to the finite size of simulated samples.

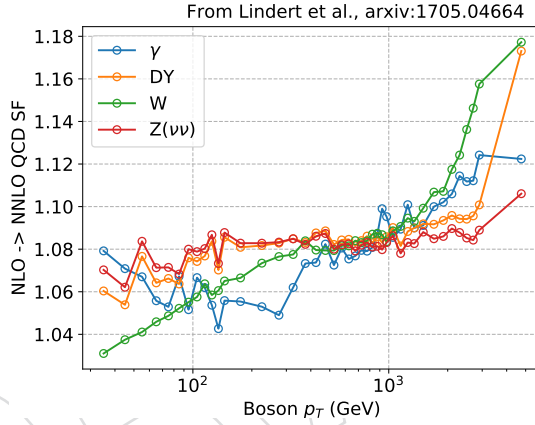


Figure 19: QCD NNLO scale factors for DY, W and photon production as a function of $p_{T,V}$.

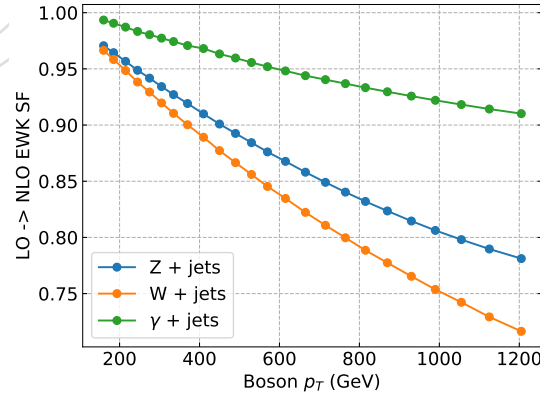


Figure 20: EW NLO scale factors for DY, W and photon production as a function of $p_{T,V}$.

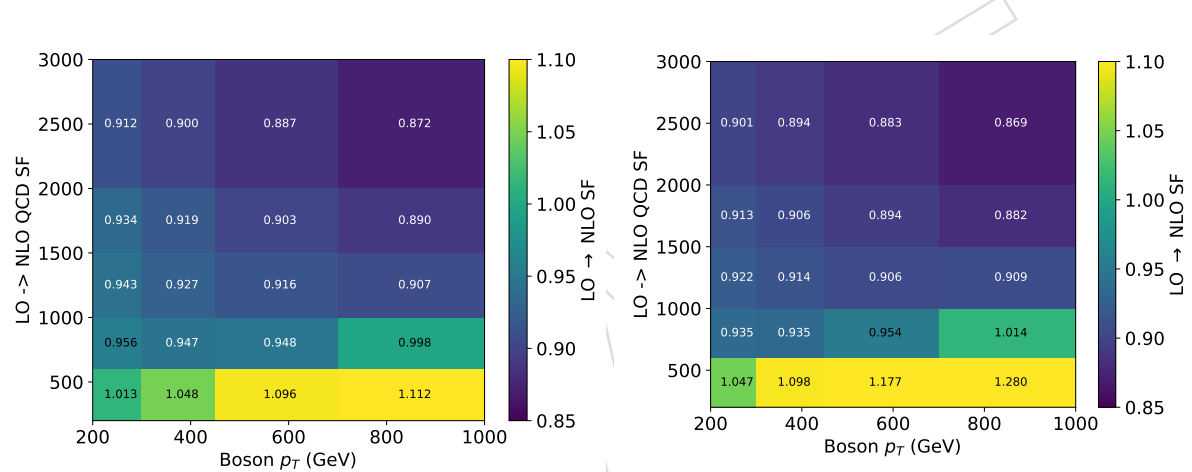


Figure 21: QCD NLO scale factors for EWK DY, W production of $p_{T,V}$ and M_{jj} .

450 6 Event selection

451 6.1 Signal region selection

452 Signal region events are selected using triggers with thresholds of 120 GeV on both $p_{\text{T},\text{trig}}^{\text{miss}}$ and
 453 $H_{\text{T},\text{trig}}^{\text{miss}}$. The $p_{\text{T},\text{trig}}^{\text{miss}}$ corresponds to the magnitude of the vector \vec{p}_{T} sum of all the PF candidates
 454 reconstructed at the trigger level, while the $H_{\text{T},\text{trig}}^{\text{miss}}$ is computed as the magnitude of the vector
 455 \vec{p}_{T} sum of jets with $p_{\text{T}} > 20$ GeV and $|\eta| < 5.0$ reconstructed at the trigger level. The energy
 456 fraction attributed to neutral hadrons in these jets is required to be smaller than 0.9. This re-
 457 quirement suppresses anomalous events with jets originating from detector noise. To be able
 458 to use the same triggers for selecting events in the muon control samples used for background
 459 prediction, muon candidates are not included in the $p_{\text{T},\text{trig}}^{\text{miss}}$ nor $H_{\text{T},\text{trig}}^{\text{miss}}$ computation. The trigger
 460 efficiency is measured to be 96% for events passing the analysis selection for $p_{\text{T}}^{\text{miss}} > 250$ GeV
 461 and becomes more than 99% efficient for events with $p_{\text{T}}^{\text{miss}} > 350$ GeV.

462 Candidate events are required to have $p_{\text{T}}^{\text{miss}} > 250$ GeV. The leading AK4 jet in the signal event
 463 is required to have $p_{\text{T}} > 80$ GeV and $|\eta| < 4.7$, and the subleading AK4 jet is required to have
 464 $p_{\text{T}} > 40$ GeV and $|\eta| < 4.7$. In addition, if the leading jet is within the tracker range, $|\eta| < 2.5$,
 465 it is required to have at least 10% of its energy coming from charged particles and less than 80
 466 % of its energy attributed to neutral hadrons, as discussed in section 4. This selection helps to
 467 remove events originating from beam-induced backgrounds. In addition, the analysis employs
 468 various event filters to reduce events with large misreconstructed $p_{\text{T}}^{\text{miss}}$ [27] originating from
 469 noncollision backgrounds.

470 For the VBF signal events, two leading jets in opposite hemispheres are expected, with large
 471 dijet mass. Furthermore, these jets are expected to have large rapidity separation and small
 472 azimuthal separation. Therefore, this analysis employs several requirements on M_{jj} , $\Delta\eta_{jj}$ and
 473 $\Delta\phi_{jj}$, which can be found in Table 11.

474 The main background processes in this search are the $Z(\nu\nu) + \text{jets}$ and $W(\ell\nu) + \text{jets}$ processes.
 475 The $Z(\nu\nu) + \text{jets}$ process is an irreducible background and constitutes the largest background
 476 in the search. In contrast, the background from $W(\ell\nu) + \text{jets}$ is suppressed by imposing a veto
 477 on events containing one or more loose muons or electrons with $p_{\text{T}} > 10$ GeV, or hadronically
 478 decaying τ leptons with $p_{\text{T}} > 18$ GeV. Events that contain a loose, isolated photon with $p_{\text{T}} >$
 479 15 GeV and $|\eta| < 2.5$ are also rejected. This helps to suppress electroweak (EW) backgrounds in
 480 which a photon is radiated from the initial state. To reduce the contamination from top quark
 481 backgrounds, events are rejected if they contain a b tagged jet with $p_{\text{T}} > 20$ GeV and $|\eta| <$
 482 2.4. These jets are identified using the DeepCSV algorithm [11, 28], adopting the “medium”
 483 working point, which corresponds to correctly identifying a jet originating from a bottom quark
 484 with a probability of 80% and misidentifying a jet originating from a charm quark (light-flavor
 485 jet) with a probability of 12 (2)%. Lastly, QCD multijet background with $E_{\text{T}}^{\text{miss}}$ arising from
 486 mismeasurements of the jet momenta is suppressed by requiring the minimum azimuthal angle
 487 between the $\vec{p}_{\text{T}}^{\text{miss}}$ direction and each of the first four leading jets with p_{T} greater than 30 GeV
 488 and $|\eta| < 2.4$ to be larger than 0.5 radians.

489 The selection requirements for this analysis are summarized in Table 11.

490 Figs. 22, 23 show the distribution of the $E_{\text{T}}^{\text{miss}}$, the number of jets, p_{T} and η distribution of the
 491 leading AK4 jet for events in the VBF signal category respectively for 2017 and 2018 datasets.

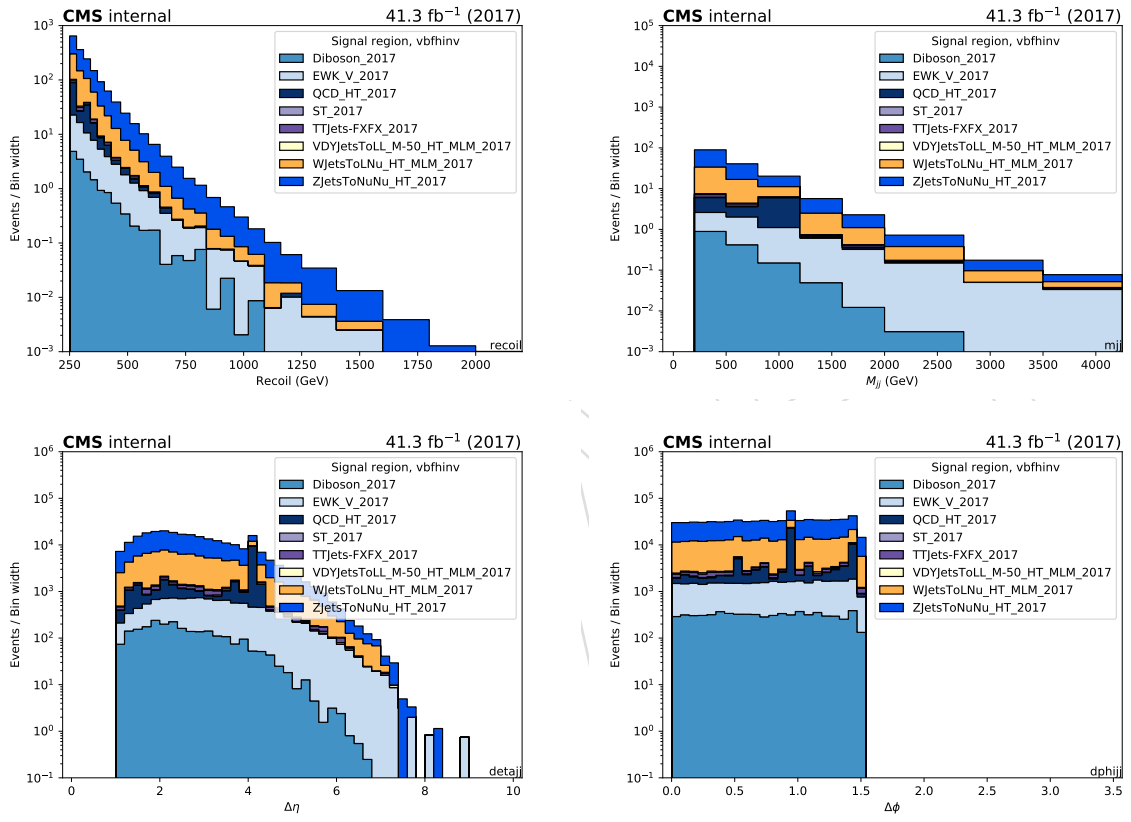


Figure 22: Recoil distribution, M_{jj} distribution, $\Delta\eta_{jj}$ and $\Delta\phi_{jj}$ distribution in the VBF signal region, using 2017 dataset.

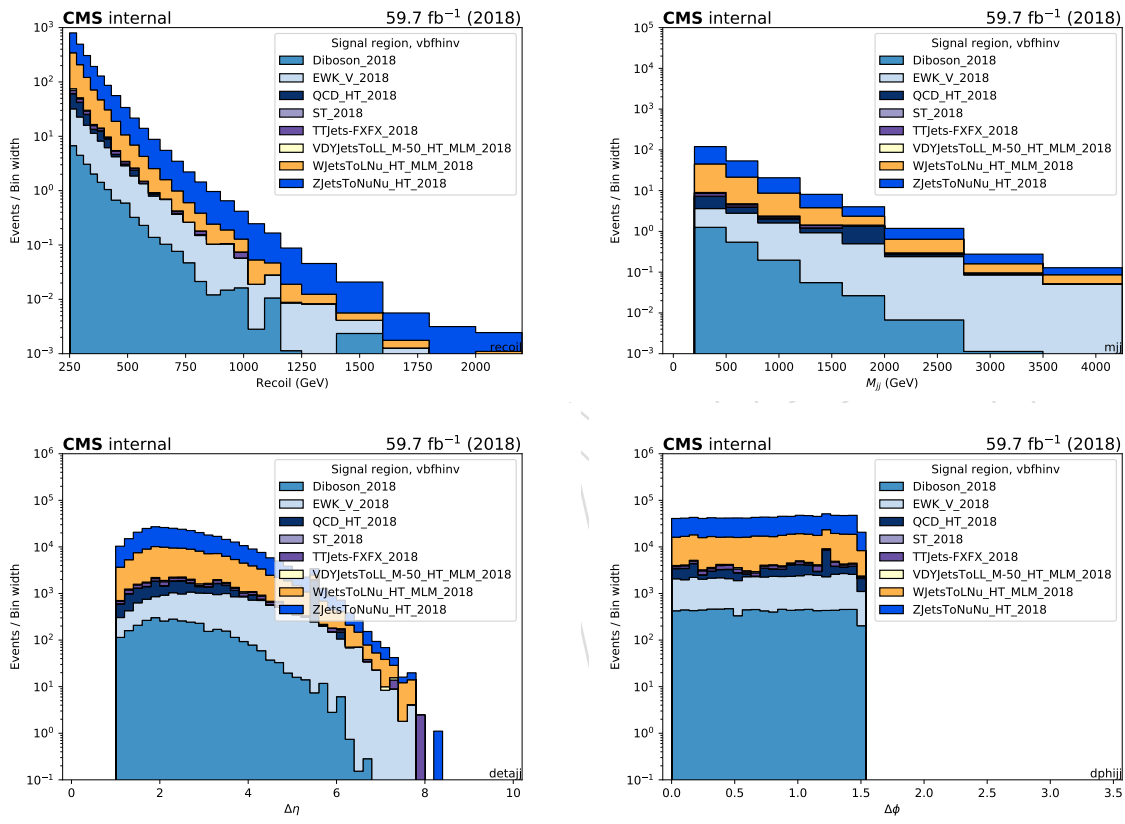


Figure 23: Recoil distribution, M_{jj} distribution, $\Delta\eta_{jj}$ and $\Delta\phi_{jj}$ distribution in the VBF signal region, using 2018 dataset.

Table 11: Summary of the common selection requirements

Variable	Selection	Target background
Muon (electron) veto	$p_T > 10 \text{ GeV}, \eta < 2.4(2.5)$	$Z(\ell\ell) + \text{jets}, W(\ell\nu) + \text{jets}$
τ lepton veto	$p_T > 18 \text{ GeV}, \eta < 2.3$	$Z(\ell\ell) + \text{jets}, W(\ell\nu) + \text{jets}$
Photon veto	$p_T > 15 \text{ GeV}, \eta < 2.5$	$\gamma + \text{jets}$
Bottom jet veto	DeepCSV medium $< 0.4941/0.4184$ (2017 / 2018) for all jets with $p_T > 20 \text{ GeV}, \eta < 2.4$	Top quark
p_T^{miss}	$> 250 \text{ GeV}$	QCD, top quark, $Z(\ell\ell) + \text{jets}$
$\Delta\phi(\vec{p}_T^{\text{jet}}, \vec{p}_T^{\text{miss}})$	$> 0.5 \text{ radians}$	QCD
Leading AK4 jet p_T and η	$> 80 \text{ GeV} \text{ and } \eta < 4.7$	All
Subleading AK4 jet p_T and η	$> 40 \text{ GeV} \text{ and } \eta < 4.7$	All
M_{jj}	$> 200 \text{ GeV}$	
$\Delta\eta_{jj}$	> 1.0	
$\Delta\phi_{jj}$	< 1.5	

492 6.2 Single muon control region selection

493 Single-muon control sample events are selected using full signal region criteria of VBF selec-
 494 tion with the exception of the muon veto. The p_T^{miss} requirement is replaced by an identical
 495 requirement on the hadronic recoil, which is defined as the sum of \vec{p}_T^{miss} and the muon \vec{p}_T , and
 496 thus corresponds to the distribution of the $W p_T$. In the single-muon control sample, exactly
 497 one tightly identified, isolated muon with $p_T > 20 \text{ GeV}$ is required. No additional loose muons
 498 or electrons with $p_T > 10 \text{ GeV}$ are allowed. In addition, the transverse mass of the muon- \vec{p}_T^{miss}
 499 system is required to be smaller than than 160 GeV. The transverse mass (M_T) is computed as
 500 $M_T = \sqrt{2E_T^{\text{miss}} p_T^\mu (1 - \cos\Delta\phi)}$, where p_T^μ is the p_T of the muon, and $\Delta\phi$ is the angle between \vec{p}_T^μ
 501 and \vec{p}_T^{miss} .

502 Figs. 24 and 26 show the distributions of the recoil, M_{jj} , $\Delta\eta_{jj}$ and $\Delta\phi_{jj}$ of the two leading AK4
 503 jets for events in the single-muon control sample for the VBF category in 2017 and 2018 datasets,
 504 respectively. Figs. 25 and 27 show the distributions of the leading muon p_T and η , as well as
 505 the muon- \vec{p}_T^{miss} transverse mass, again for 2017 and 2018, respectively.

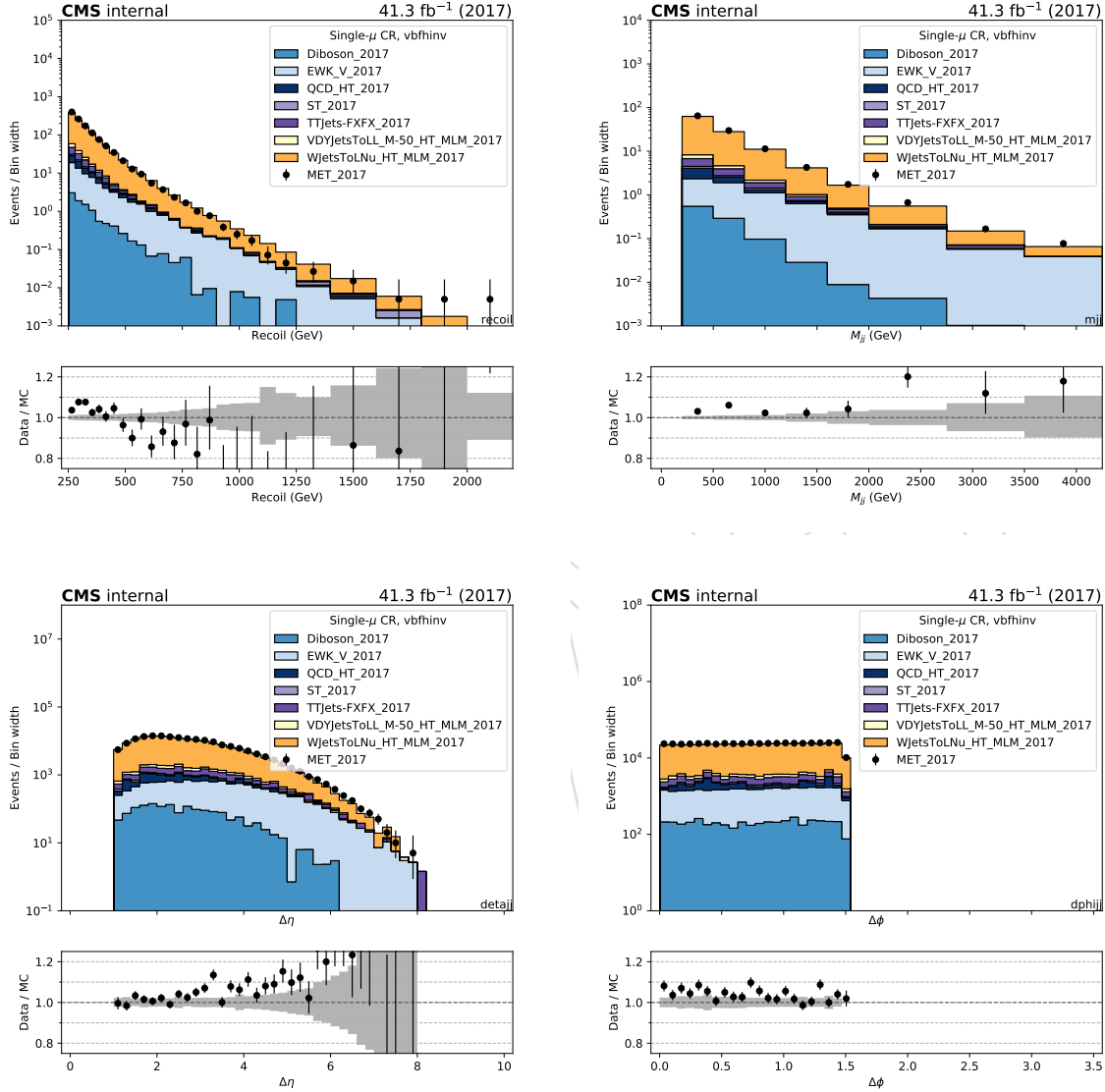


Figure 24: Comparison between 2017 data and Monte Carlo simulation in the single muon control sample for the recoil distribution, the M_{jj} distribution, $\Delta\eta_{jj}$ distribution and $\Delta\phi_{jj}$ distribution for the two leading AK4 jets with the VBF selection.

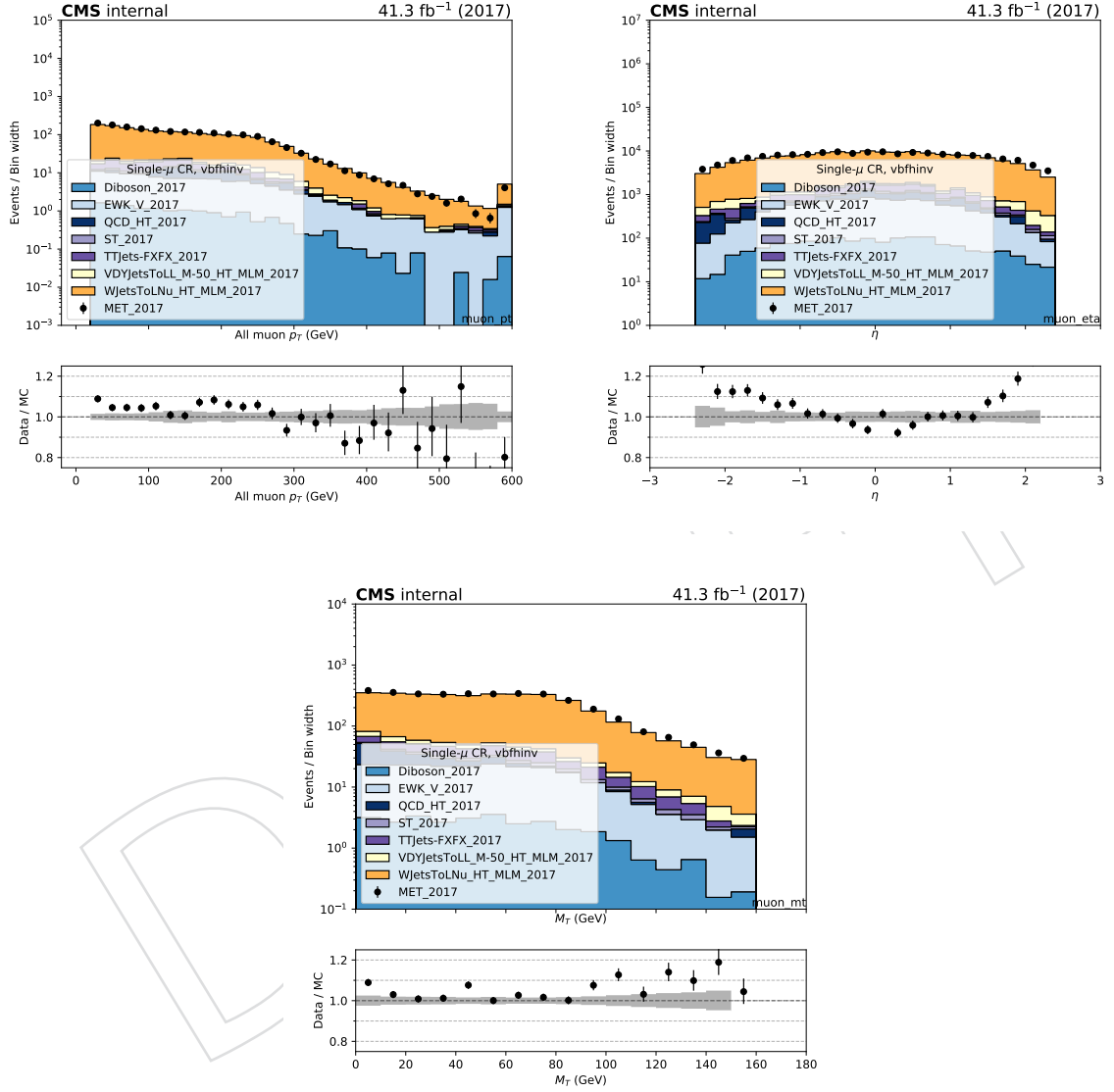


Figure 25: Comparison between 2017 data and Monte Carlo simulation in the single muon control sample for the p_T and η of the leading muon and the transverse mass distribution with the VBF selection.

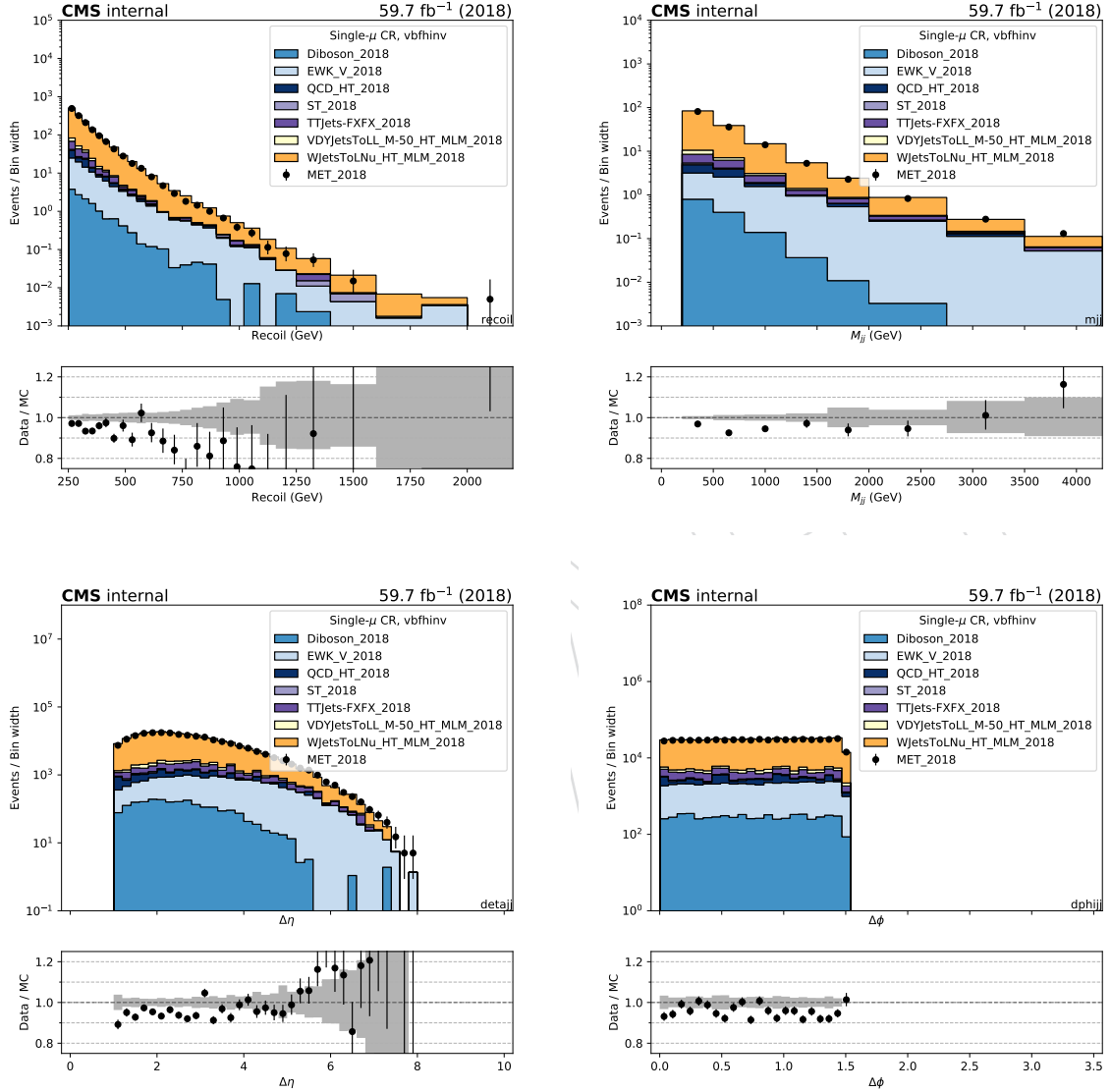


Figure 26: Comparison between 2018 data and Monte Carlo simulation in the single muon control sample for the recoil distribution, the M_{jj} distribution, $\Delta\eta_{jj}$ distribution and $\Delta\phi_{jj}$ distribution for the two leading AK4 jets with the VBF selection.

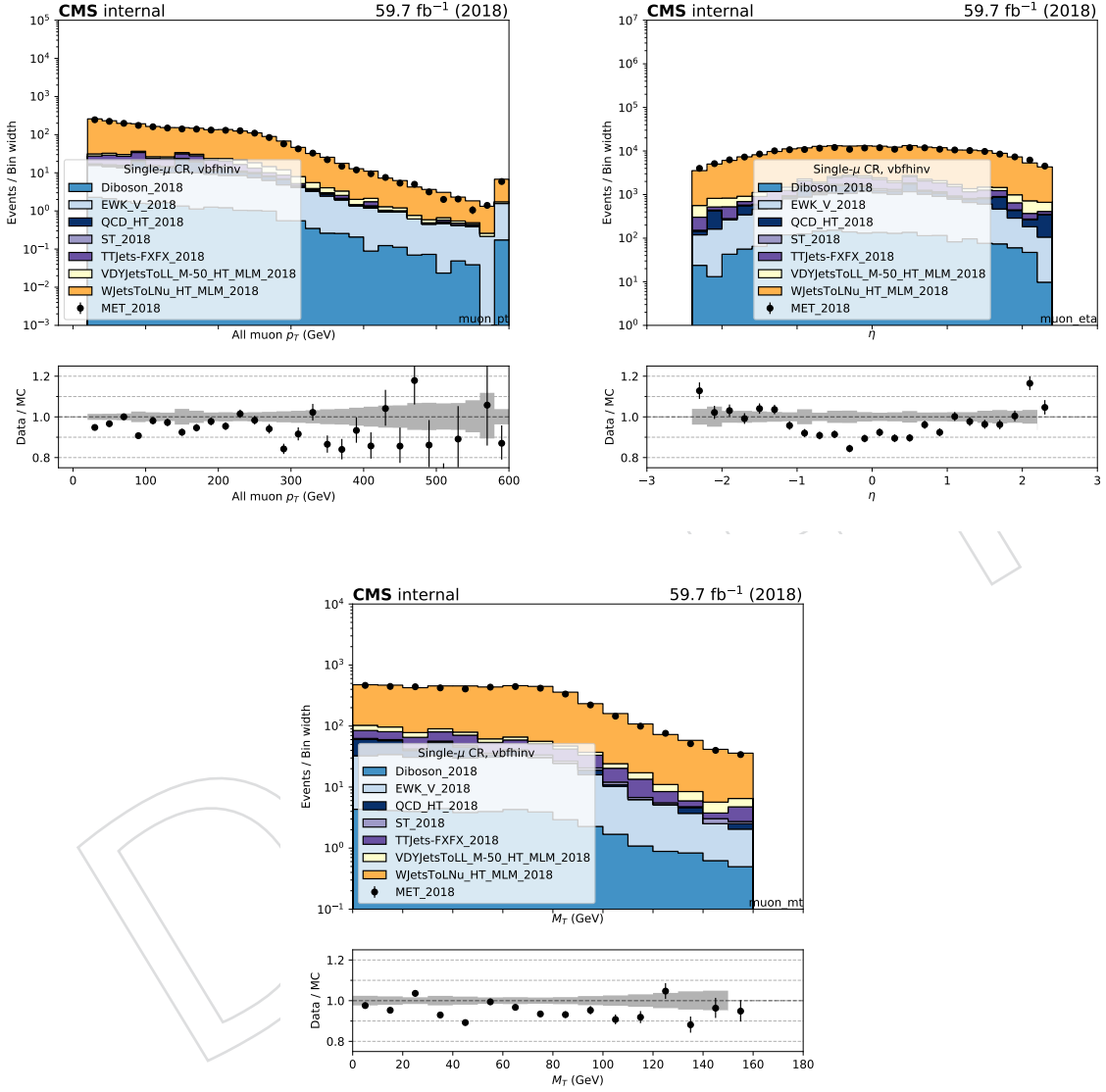


Figure 27: Comparison between 2018 data and Monte Carlo simulation in the single muon control sample for the p_T and η of the leading muon and the transverse mass distribution with the VBF selection.

6.3 Single electron control region selection

Events for the single-electron control sample are collected with the single-electron and photon triggers described in Sec. 2. The p_T^{miss} requirement is replaced with an identical requirement on the hadronic recoil, which is defined as the sum of \vec{p}_T^{miss} and the electron \vec{p}_T , and thus corresponds to the distribution of the $W p_T$. The events in the single-electron control sample are required to contain exactly one tightly identified and isolated electron with $p_T > 40$ GeV. In addition, the contamination from QCD multijet events in this control sample is suppressed by requiring $E_T^{\text{miss}} > 50$ GeV and $M_T < 160$ GeV.

Figs. 28 and 30 show the distributions of the recoil, M_{jj} , $\Delta\eta_{jj}$ and $\Delta\phi_{jj}$ of the two leading AK4 jets for events in the single-electron control sample for the VBF category in 2017 and 2018 datasets, respectively. Figs. 29 and 31 show the distributions of the leading electron p_T and η , as well as the electron- p_T^{miss} transverse mass, again for 2017 and 2018, respectively.

DRAFT

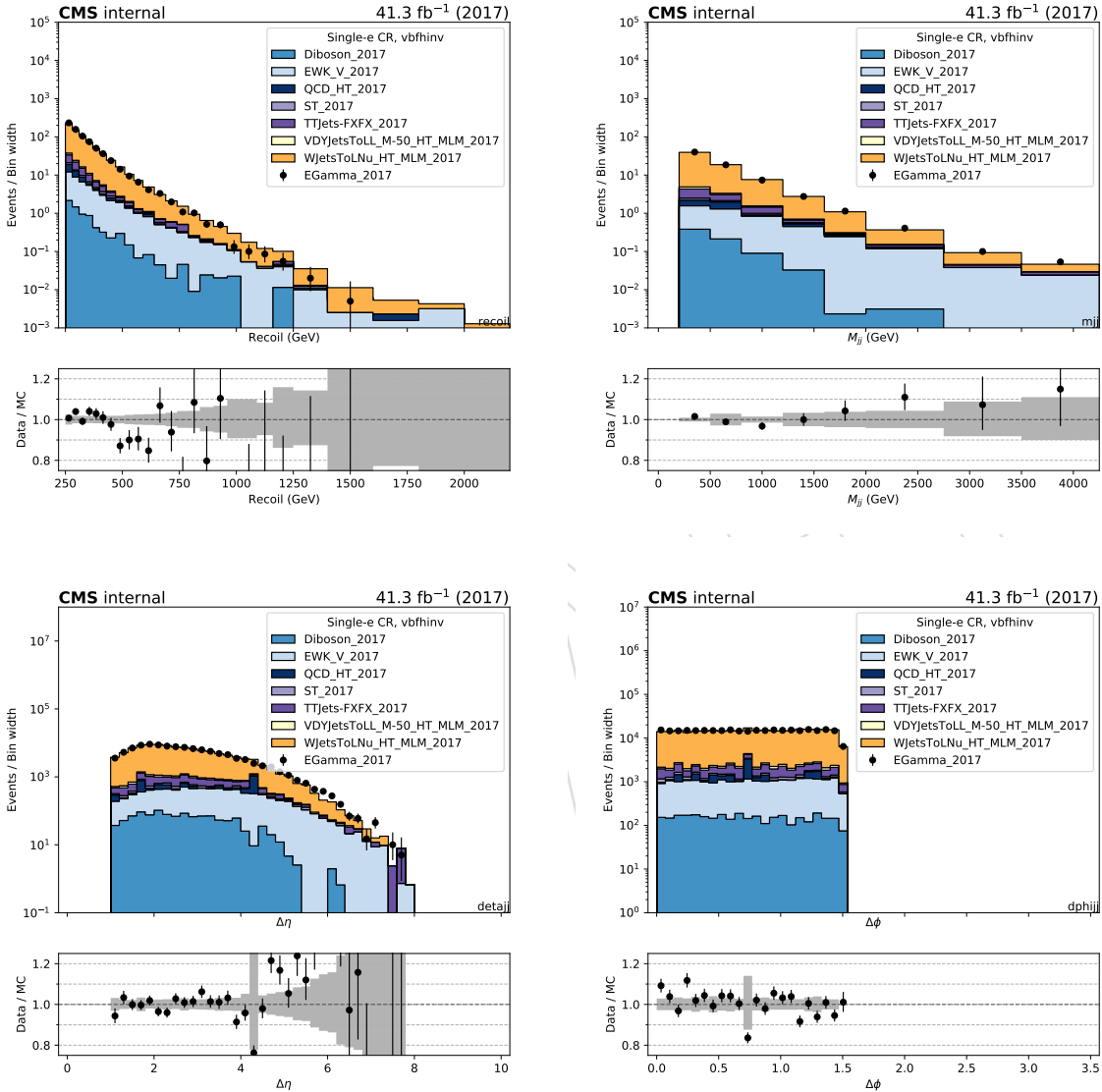


Figure 28: Comparison between 2017 data and Monte Carlo simulation in the single electron control sample for the recoil distribution, the M_{jj} distribution, $\Delta\eta_{jj}$ distribution and $\Delta\phi_{jj}$ distribution for the two leading AK4 jets with the VBF selection.

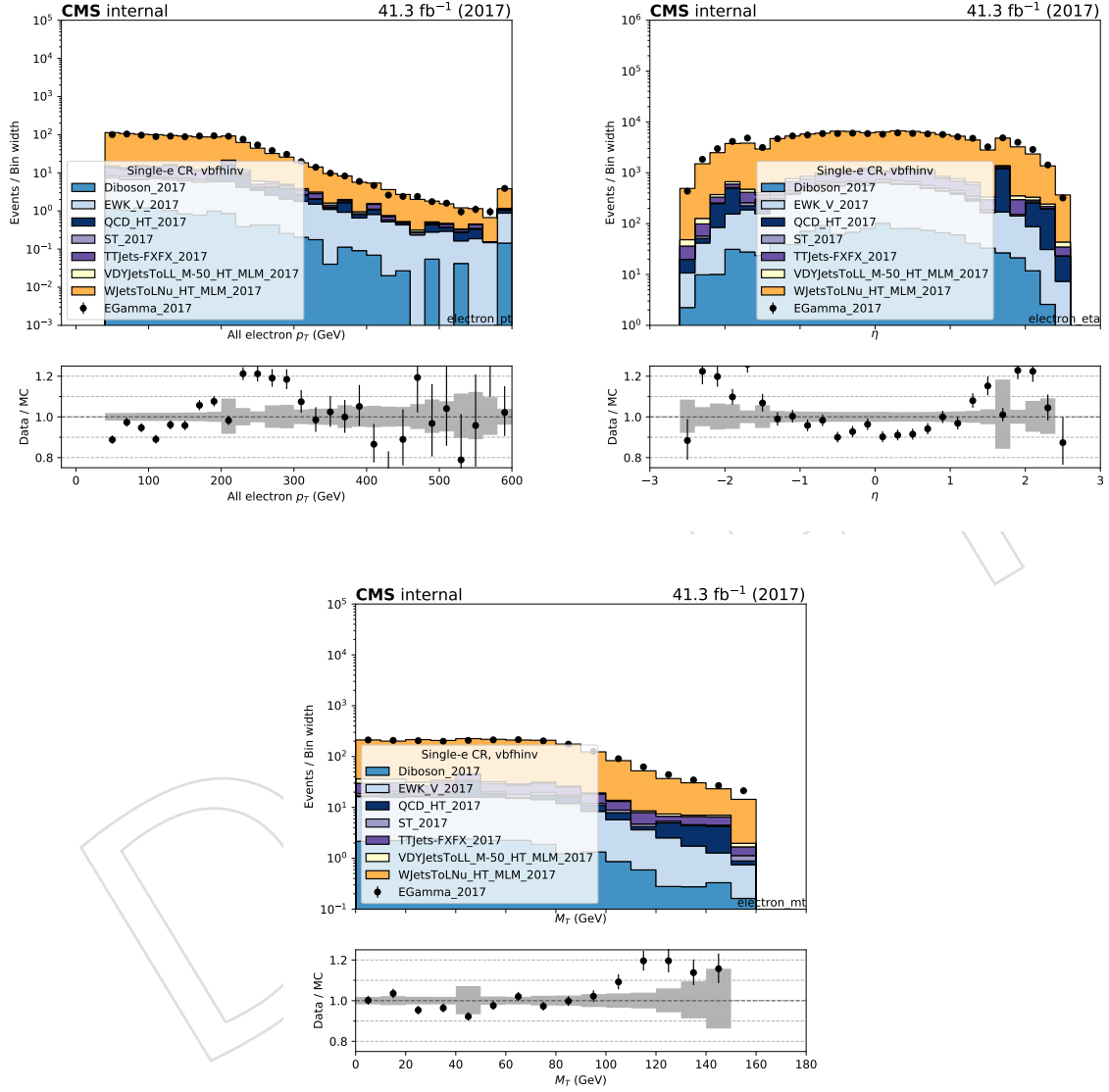


Figure 29: Comparison between 2017 data and Monte Carlo simulation in the single electron control sample for the p_T and η of the leading electron and the transverse mass distribution with the VBF selection.

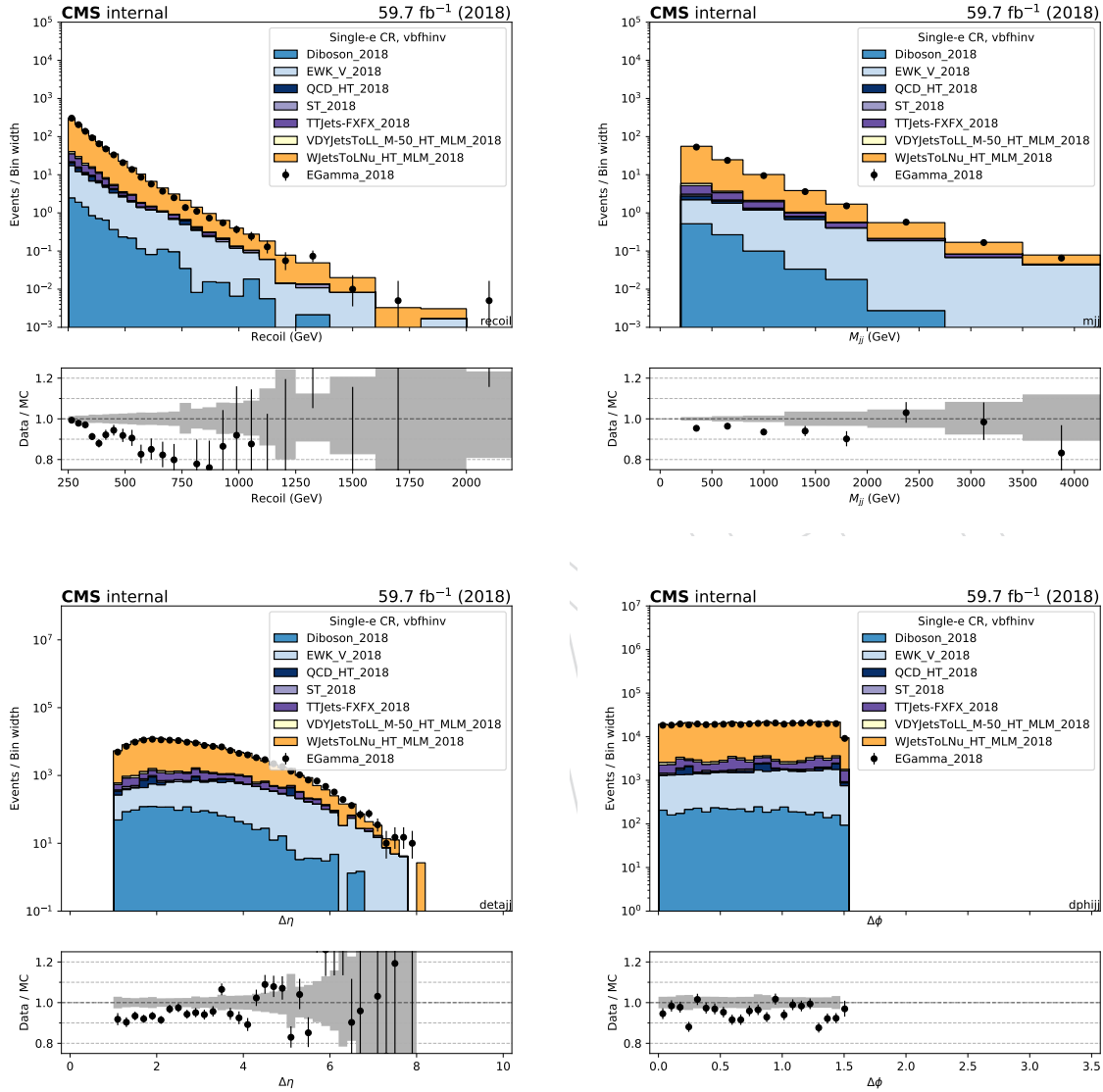


Figure 30: Comparison between 2018 data and Monte Carlo simulation in the single electron control sample for the recoil distribution, the M_{jj} distribution, $\Delta\eta_{jj}$ distribution and $\Delta\phi_{jj}$ distribution for the two leading AK4 jets with the VBF selection.

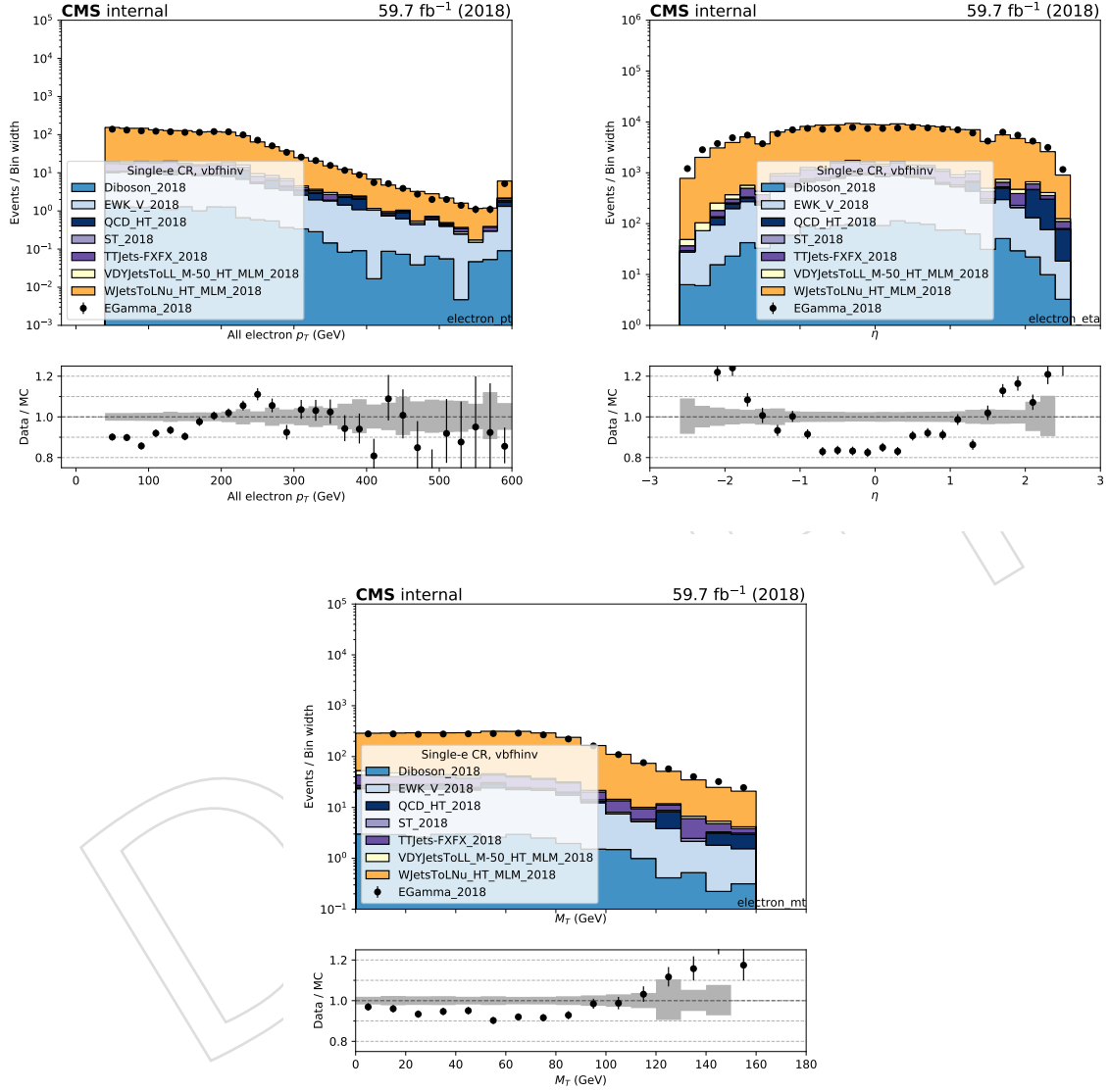


Figure 31: Comparison between 2018 data and Monte Carlo simulation in the single electron control sample for the p_T and η of the leading electron and the dilepton mass distribution with the VBF selection.

518 **6.4 Double muon control region selection**

519 Double-muon control sample events are selected using full signal region criteria of VBF cate-
520 gory with the exception of the muon veto. In the double-muon control sample, events are se-
521 lected requiring leading (subleading) muon p_T greater than 20 (10) GeV and an invariant mass
522 in the range 60 to 120 GeV, compatible with a Z boson decay. At least one of the two muons
523 is required to pass the tight candidate definition. Events are rejected if there is an additional
524 loose muon or electron with $p_T > 10$ GeV. The SR p_T^{miss} requirement is replacement an identical
525 requirement on the hadronic recoil, which is defined as the sum of \vec{p}_T^{miss} and the muon \vec{p}_T , and
526 thus corresponds to the distribution of the Z p_T smeared with the p_T^{miss} resolution.

527 Figs. 32 and 34 shows the distributions of the recoil, M_{jj} , $\Delta\eta_{jj}$ and $\Delta\phi_{jj}$ of the two leading
528 AK4 jets for events in the double-muon control sample for the VBF category in 2017 and 2018
529 datasets, respectively. Figs. 33 and 35 show the distributions of the leading muon p_T and η , as
530 well as the dimuon mass and p_T , again for 2017 and 2018, respectively.

DRAFT

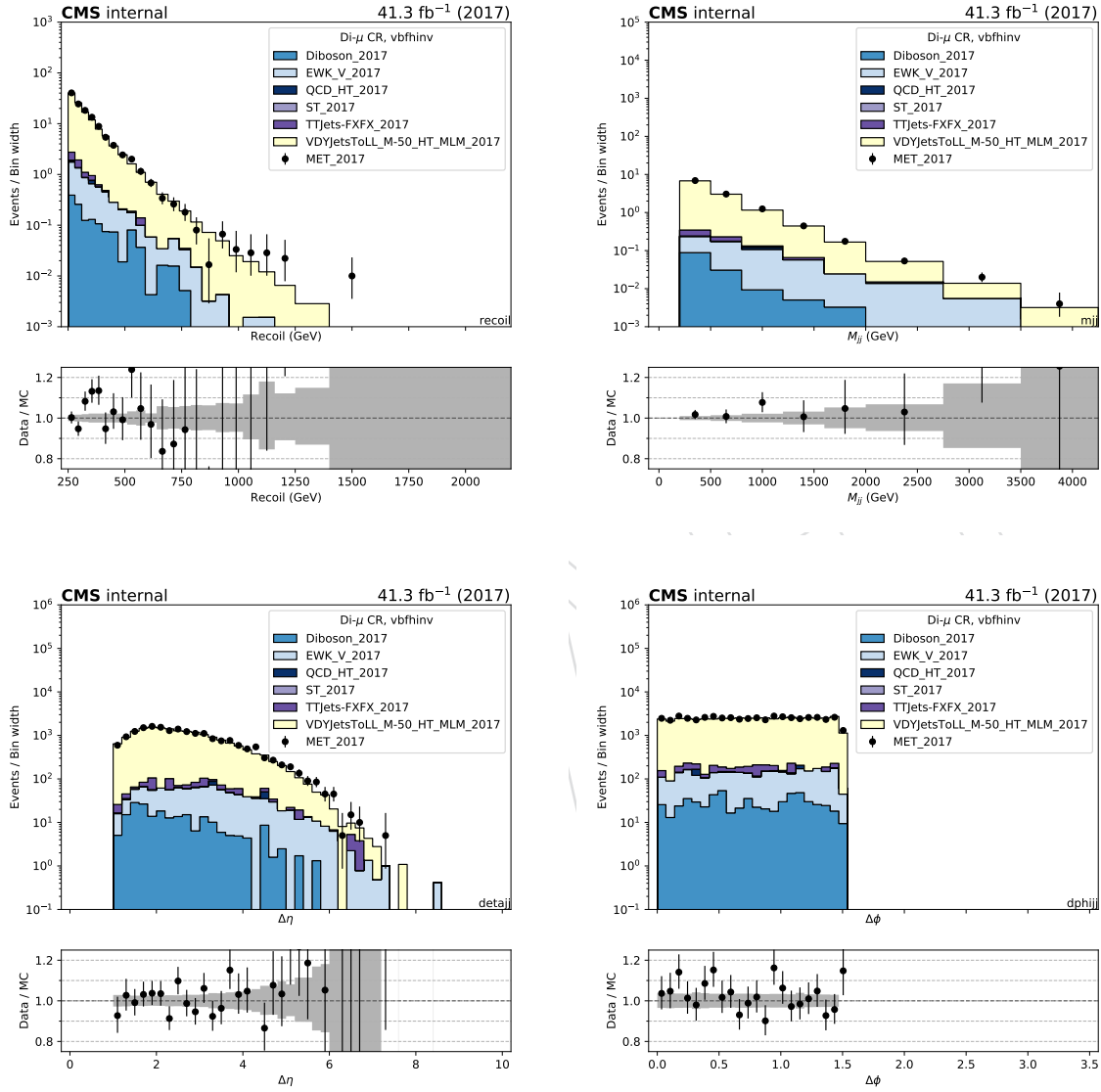


Figure 32: Comparison between 2017 data and Monte Carlo simulation in the double muon control sample for the recoil distribution, the M_{jj} distribution, $\Delta\eta_{jj}$ distribution and $\Delta\phi_{jj}$ distribution for the two leading AK4 jets with the VBF selection.

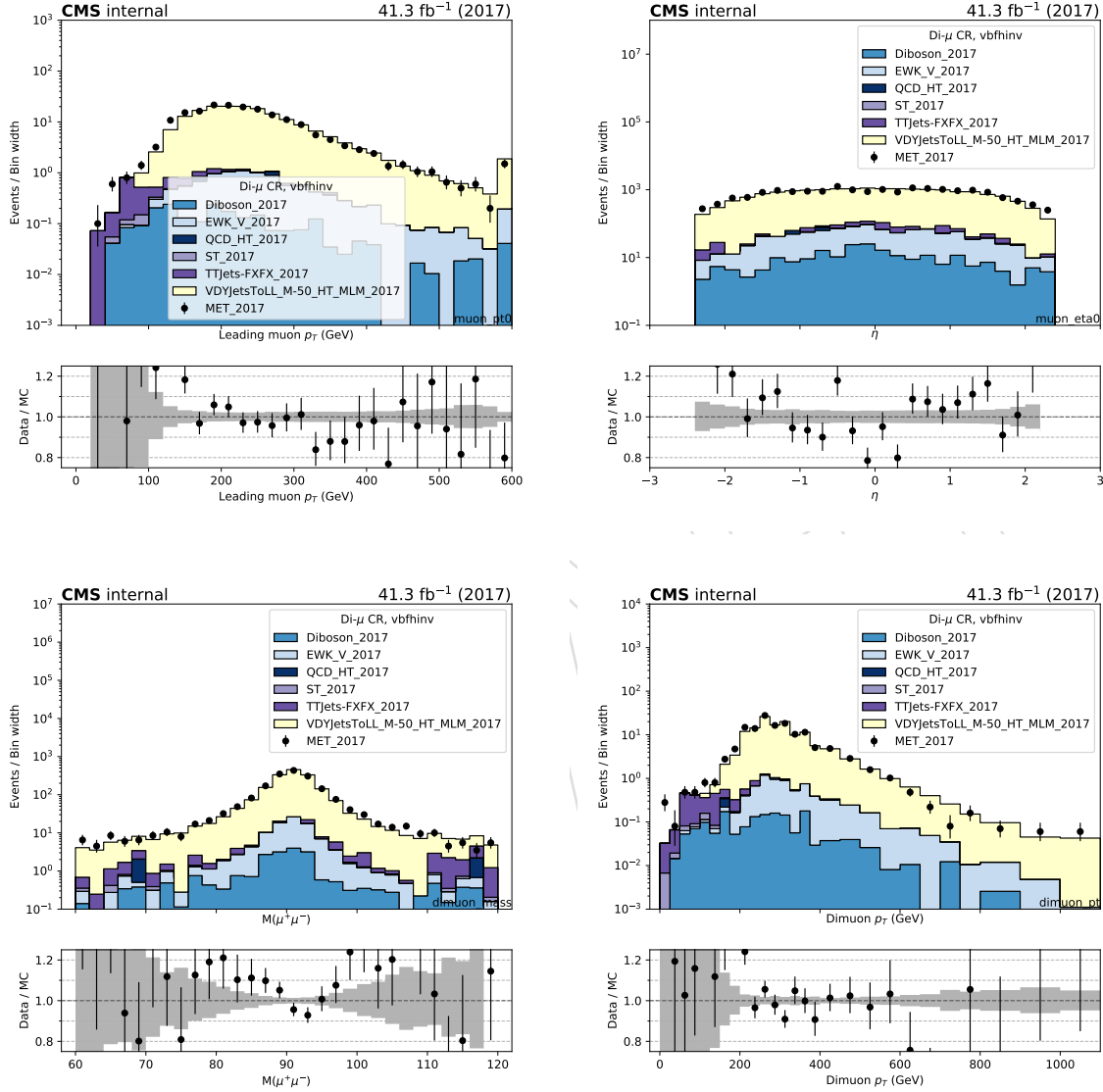


Figure 33: Comparison between 2017 data and Monte Carlo simulation in the double muon control sample for the p_T and η of the leading muon and the transverse mass and p_T of the dimuon candidate with the VBF selection.

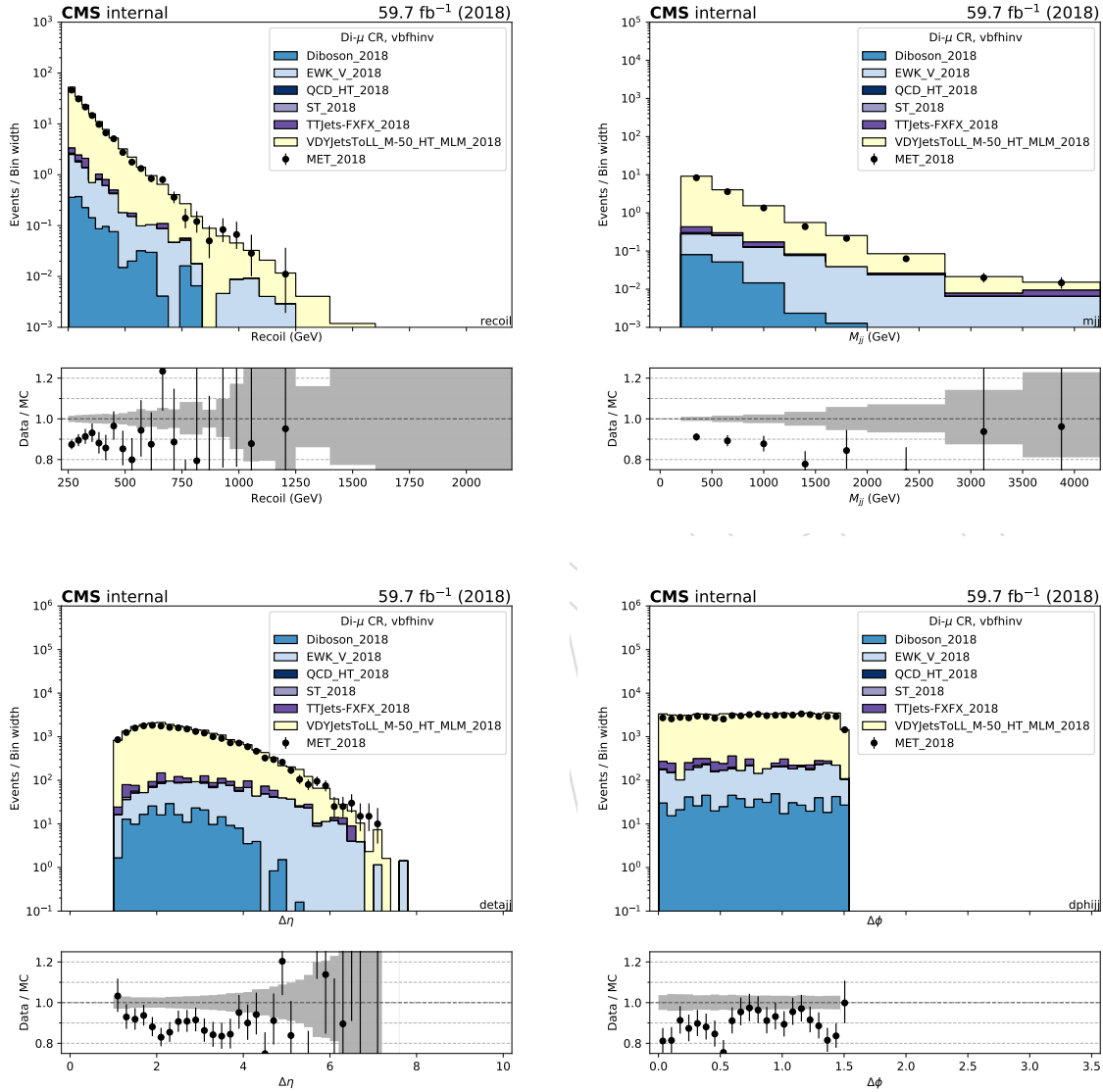


Figure 34: Comparison between 2018 data and Monte Carlo simulation in the double muon control sample for the recoil distribution, the M_{jj} distribution, $\Delta\eta_{jj}$ distribution and $\Delta\phi_{jj}$ distribution for the two leading AK4 jets with the VBF selection.

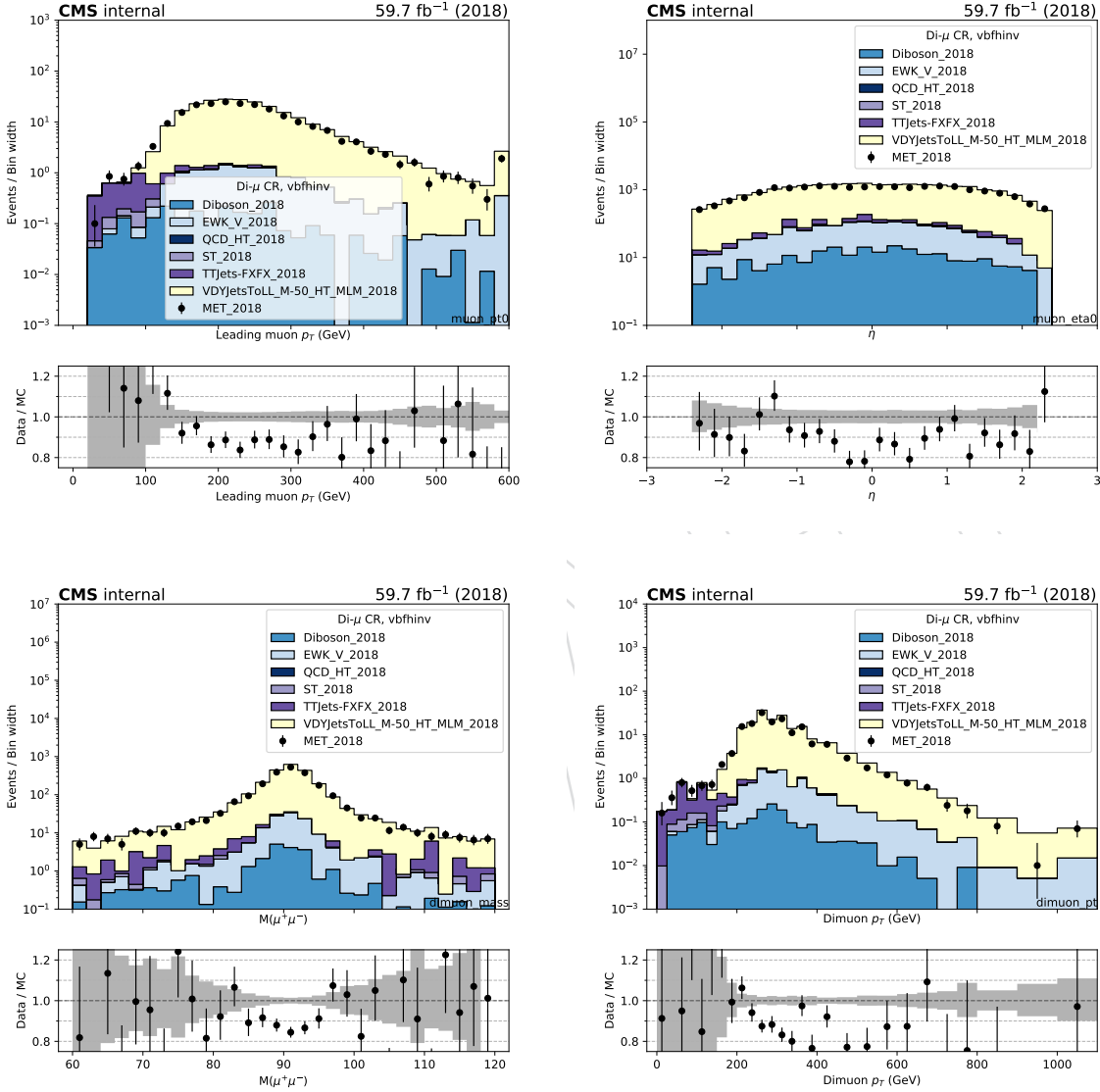


Figure 35: Comparison between 2018 data and monte carlo simulation in the double muon control sample for the p_T and η of the leading muon and the transverse mass and p_T of the dimuon candidate with the VBF selection.

531 6.5 Double electron control region selection

532 Events for the double-electron control sample are collected with the single-electron and photon
533 triggers described in Sec. 2. In the offline analysis, events in the dielectron control sample are
534 required to contain exactly two oppositely charged electrons with leading (trailing) electron p_T
535 greater than 40 (10) GeV, with at least one of the two passing the tight candidate definition. The
536 SR p_T^{miss} requirement is replacement an identical requirement on the hadronic recoil, which is
537 defined as the sum of \vec{p}_T^{miss} and the muon \vec{p}_T , and thus corresponds to the distribution of the Z
538 p_T smeared with the p_T^{miss} resolution. Similar to the dimuon control sample case, the invariant
539 mass of the dielectron system is required to be between 60 and 120 GeV to be consistent with a
540 Z boson decay.

541 Figs. 36 and 38 shows the distributions of the recoil, M_{jj} , $\Delta\eta_{jj}$ and $\Delta\phi_{jj}$ for the two leading
542 AK4 jets for events in the double-electron control sample for the VBF category in 2017 and 2018
543 datasets, respectively. Figs. 37 and 39 show the distributions of the leading electron p_T and η ,
544 as well as the dielectron mass and p_T , again for 2017 and 2018, respectively.

DRAFT

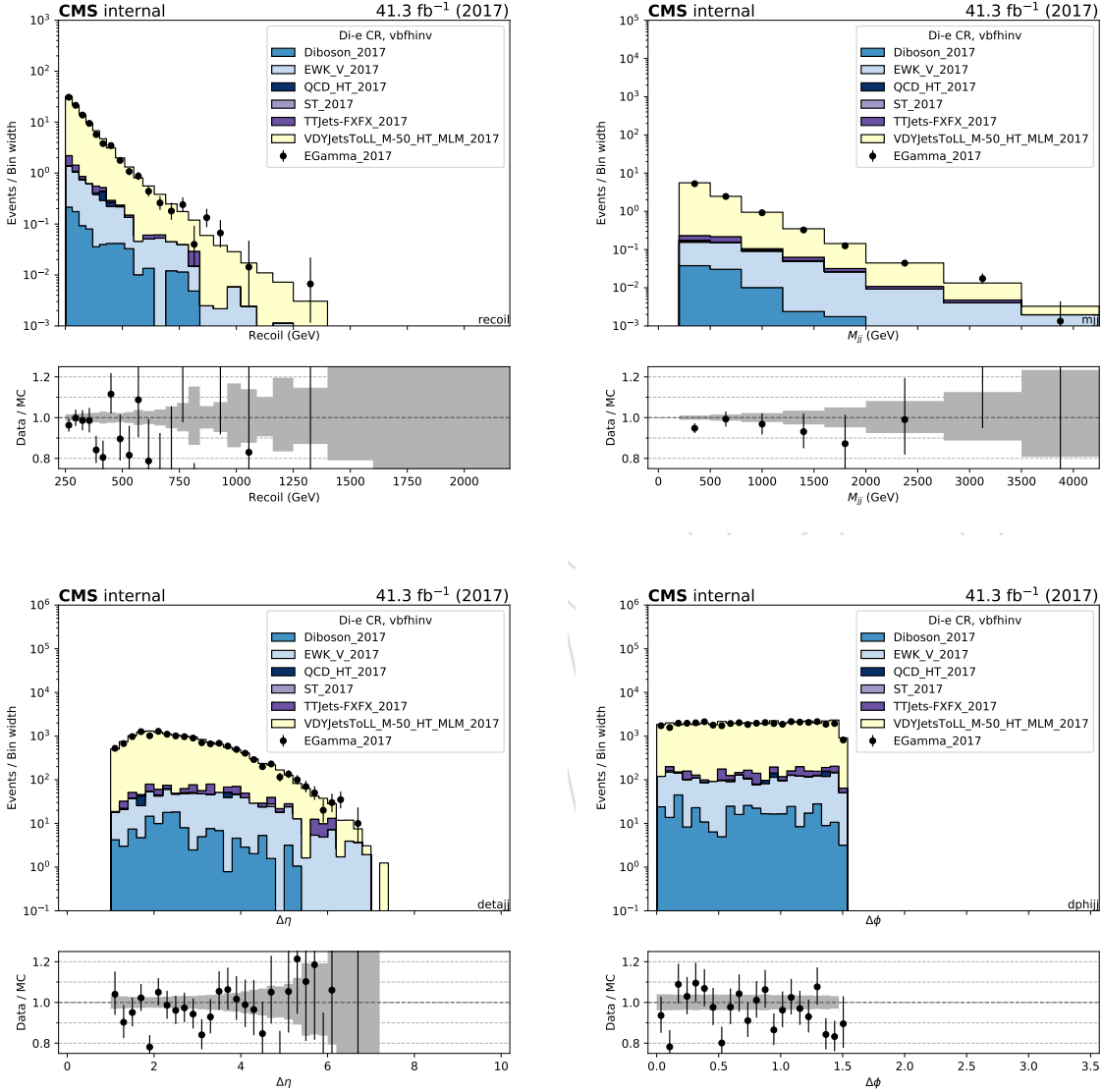


Figure 36: Comparison between 2017 data and Monte Carlo simulation in the double electron control sample for the recoil distribution, the M_{jj} distribution, $\Delta\eta_{jj}$ distribution and $\Delta\phi_{jj}$ distribution for the two leading AK4 jets with the VBF selection.

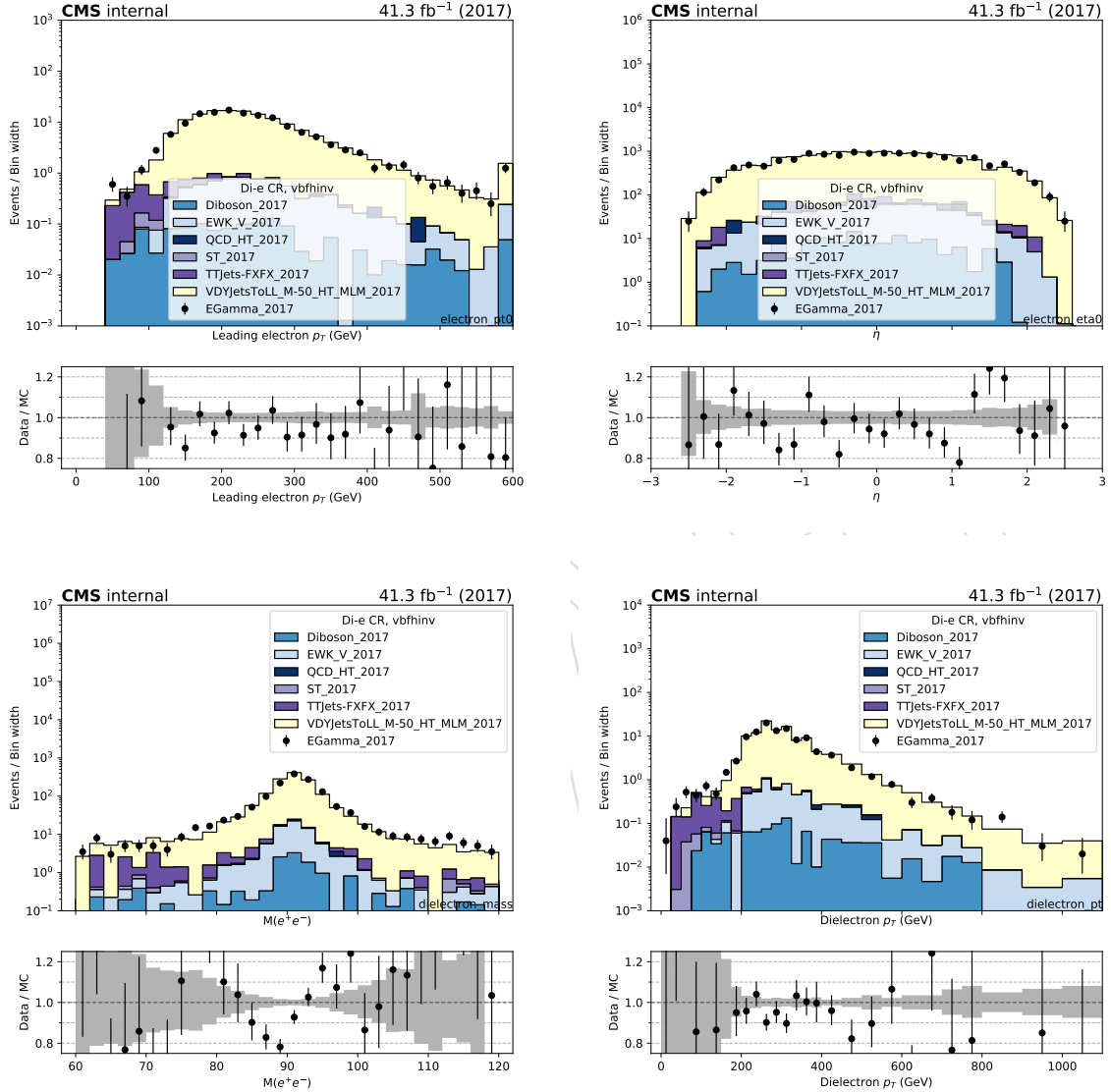


Figure 37: Comparison between 2017 data and Monte Carlo simulation in the double electron control sample for the p_T and η of the leading electron and the transverse mass and p_T of the dielectron candidate with the VBF selection.

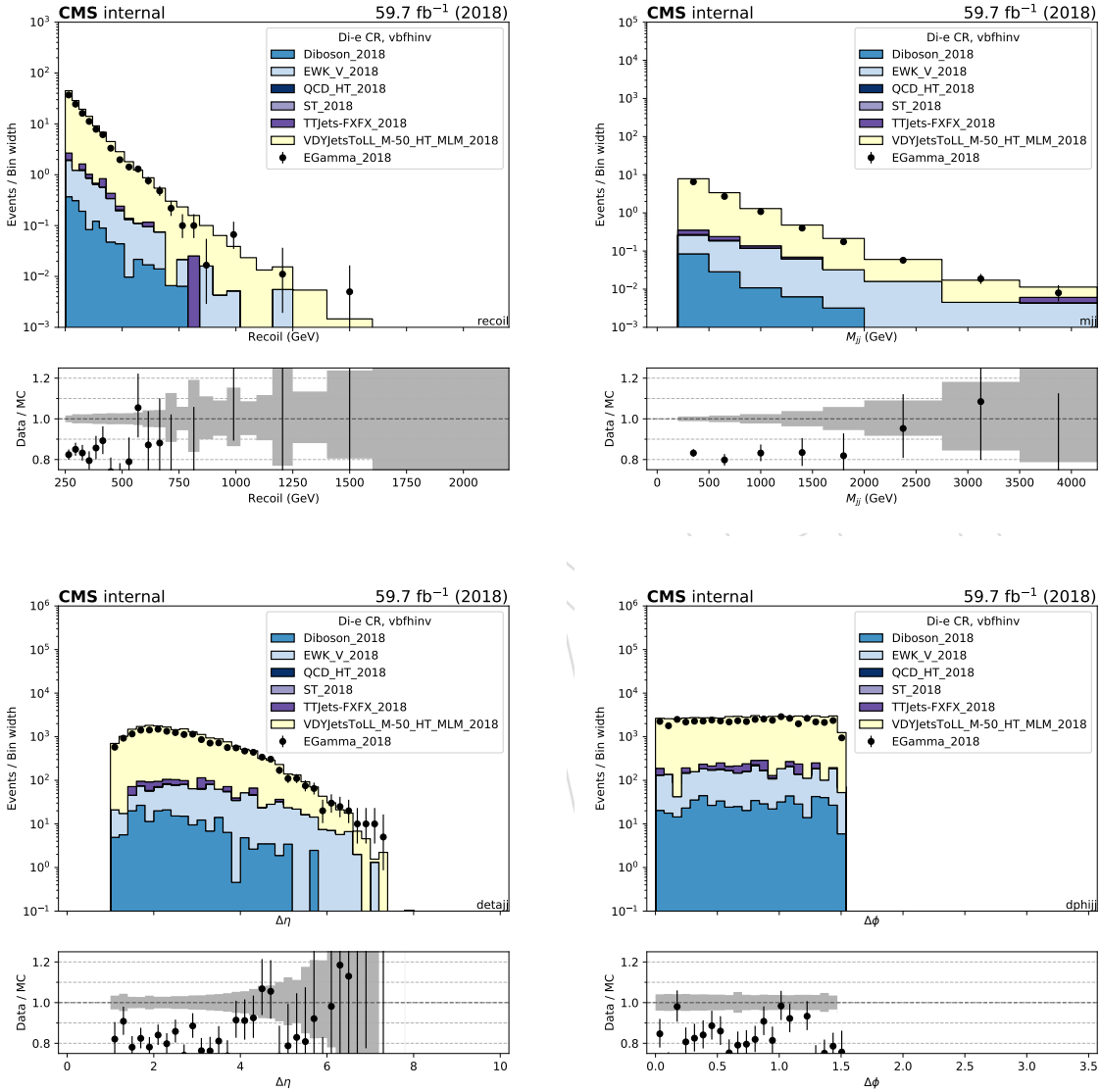


Figure 38: Comparison between 2018 data and Monte Carlo simulation in the double electron control sample for the recoil distribution, the M_{jj} distribution, $\Delta\eta_{jj}$ distribution and $\Delta\phi_{jj}$ distribution for the two leading AK4 jets with the VBF selection.

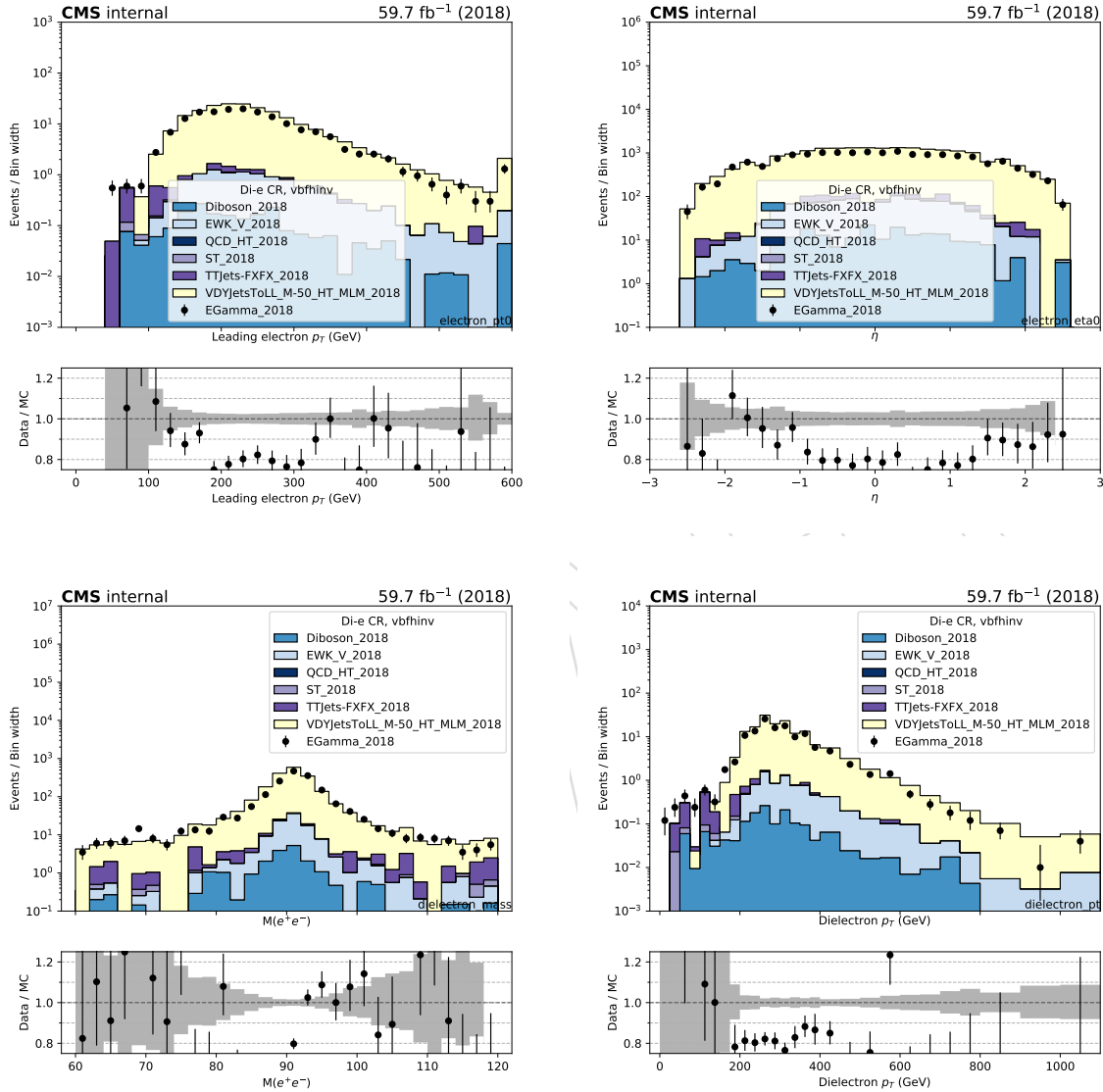


Figure 39: Comparison between 2018 data and Monte Carlo simulation in the double electron control sample for the p_T and η of the leading electron and the transverse mass and p_T of the dielectron candidate with the VBF selection.

545 6.6 Photon control region

546 The $\gamma + \text{jets}$ control sample is selected using events with one high- p_T photon collected using
 547 single-photon triggers with p_T thresholds of 165 or 175 GeV, depending on the data taking
 548 conditions. The photon is required to have $p_T > 175$ GeV and to pass tight identification and
 549 isolation criteria, to ensure a high trigger efficiency of 98%.

550 Figs. 40 and 40 show the distributions of the recoil, M_{jj} , $\Delta\eta_{jj}$ and $\Delta\phi_{jj}$ distribution of the two
 551 leading AK4 jets for events in the photon control sample for the VBF category in the 2017 and
 552 2018 datasets, respectively. Similarly, Figs. 41 and 43 show the distributions of the photon p_T
 553 and η .

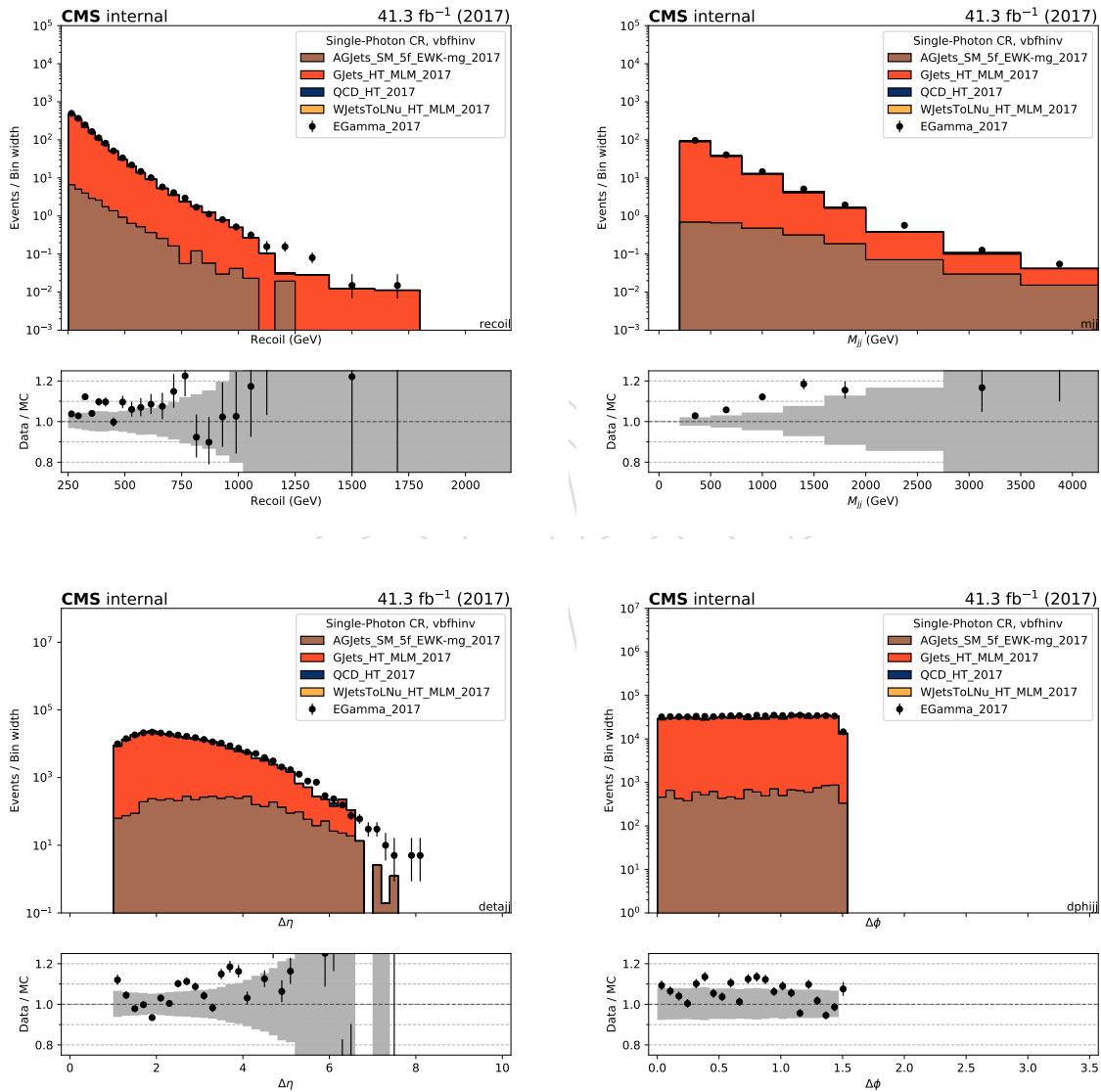


Figure 40: Comparison between 2017 data and Monte Carlo simulation in the photon control sample for the recoil distribution, the M_{jj} distribution, $\Delta\eta_{jj}$ distribution and $\Delta\phi_{jj}$ distribution for the two leading AK4 jets with the VBF selection.

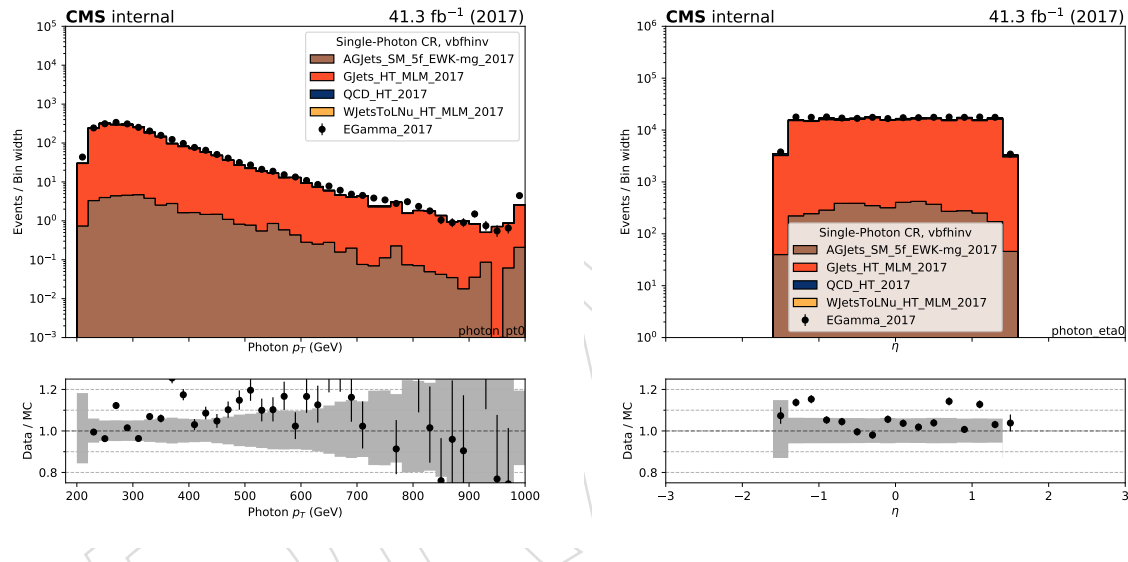


Figure 41: Comparison between 2017 data and Monte Carlo simulation in the photon control sample for the p_T and η of the leading photon with the VBF selection.

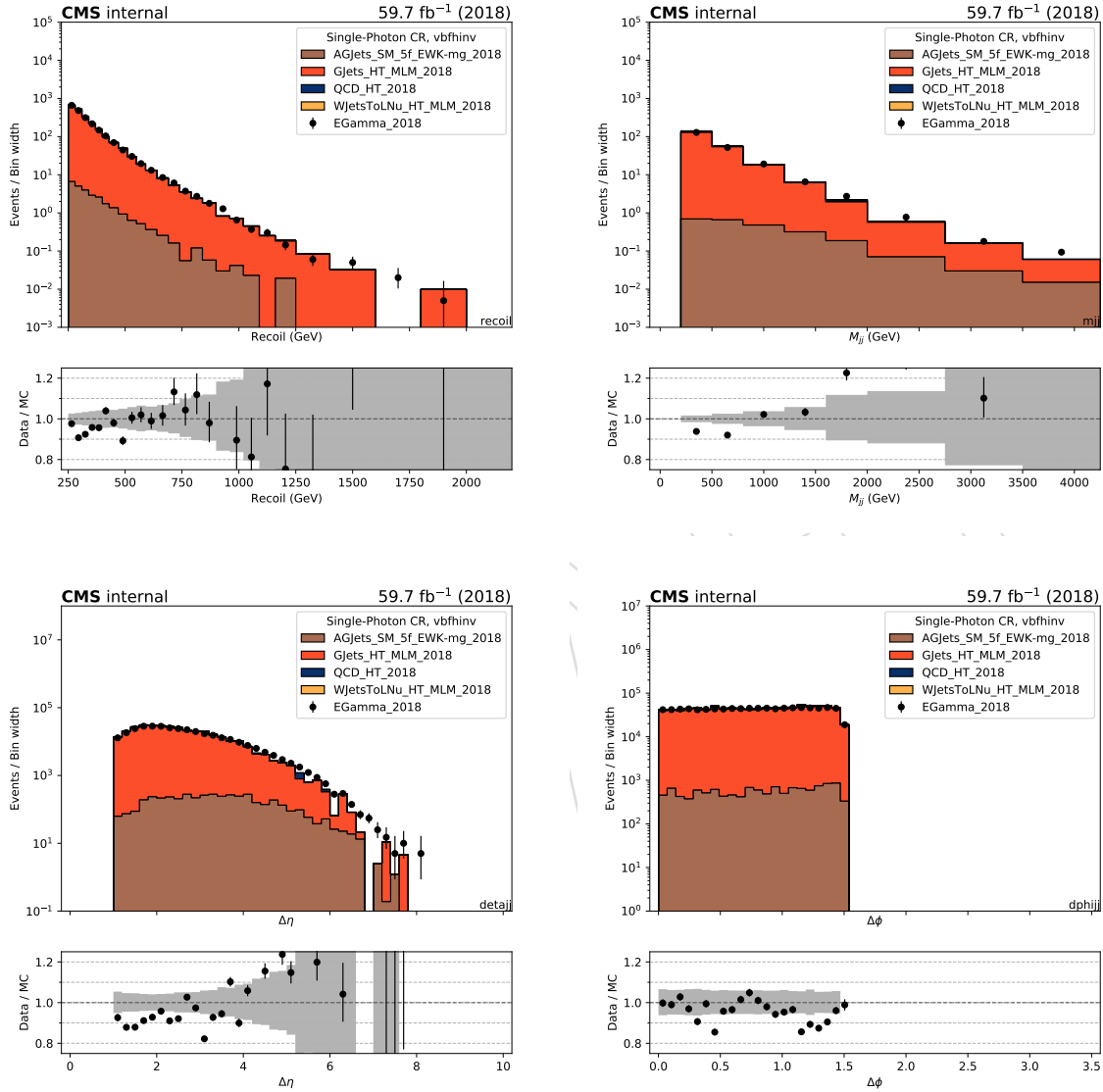


Figure 42: Comparison between 2018 data and Monte Carlo simulation in the photon control sample for the recoil distribution, the M_{jj} distribution, $\Delta\eta_{jj}$ distribution and $\Delta\phi_{jj}$ distribution for the two leading AK4 jets with the VBF selection.

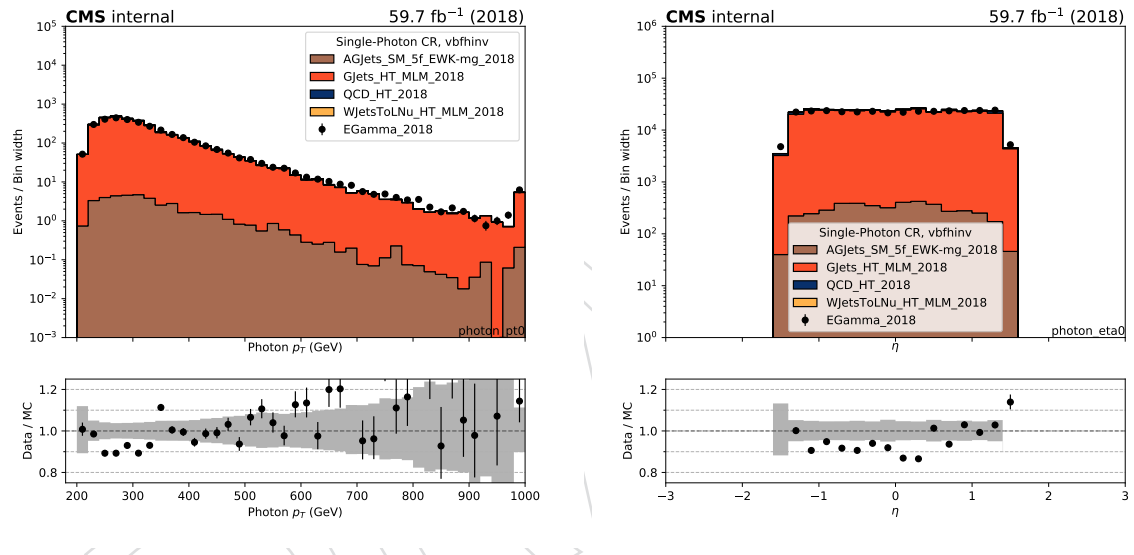


Figure 43: Comparison between 2018 data and Monte Carlo simulation in the photon control sample for the p_T and η of the leading photon with the VBF selection.

554 7 Background estimation

555 The largest background contributions from $Z(\nu\nu) + \text{jets}$ and $W(\ell\nu) + \text{jets}$ processes are esti-
 556 mated using data from four mutually exclusive control samples selected from dimuon, dielec-
 557 tron, single-muon, and single-electron states, as explained below.

558 The remaining backgrounds that contribute to the total event yield in the signal region are
 559 much smaller than those from $Z(\nu\nu) + \text{jets}$ and $W(\ell\nu) + \text{jets}$ processes. These backgrounds in-
 560 clude QCD multijet events which are measured from data using a $\Delta\phi$ extrapolation method [29,
 561 30], and top-quark and diboson processes, which are obtained directly from simulation and are
 562 explained in the previous sections.

563 7.1 Signal extraction strategy

564 A binned likelihood fit to the data (constructed as a product of poisson probabilities) as pre-
 565 sented here:

$$\mathcal{L}(\mu^{Z \rightarrow \nu\nu}, \mu, \theta) = \prod_i \text{Pois}\left(d_i | B_i(\theta) + (1 + f_i(\theta)_{\text{QCD}})\mu_i^{Z \rightarrow \nu\nu} + R_i^{Z \rightarrow \circ \circ} (1 + f_i(\theta)_{\text{EW}})\mu_i^{Z \rightarrow \nu\nu} + \mu S_i(\theta)\right) \times \\ \prod_i \text{Pois}\left(d_i^Z | B_i^Z(\theta) + \frac{\mu_i^{Z \rightarrow \nu\nu}}{R_i^Z(\theta)_{\text{QCD}}} + \frac{\mu_i^{Z \rightarrow \nu\nu}}{R_i^Z(\theta)_{\text{EW}}}\right) \\ \prod_i \text{Pois}\left(d_i^W | B_i^W(\theta) + \frac{f_i(\theta)_{\text{QCD}} \mu_i^{Z \rightarrow \nu\nu}}{R_i^W(\theta)_{\text{QCD}}} + \frac{f_i(\theta)_{\text{EW}} \mu_i^{Z \rightarrow \nu\nu}}{R_i^W(\theta)_{\text{EW}}}\right) \times \quad (4)$$

566 The fit is performed simultaneously in the four different control samples and in the signal re-
 567 gion, for events selected in the vbf category, to estimate the $Z(\nu\nu) + \text{jets}$ and $W(\ell\nu) + \text{jets}$ rate in
 568 each m_{jj} bin. In this likelihood, the expected number of $Z(\nu\nu) + \text{jets}$ events in each bin of m_{jj} are
 569 the free parameters of the fit. The $Z(\nu\nu) + \text{jets}$ and $W(\ell\nu) + \text{jets}$ rates are estimated separately
 570 for the QCD and EW components separately in each m_{jj} bin. However the fit is constrained
 571 using the $R_i^{Z \rightarrow \circ \circ}$ which demonstrates the ratio between the QCD and EW components of the
 572 $Z(\nu\nu) + \text{jets}$ background. This ratio does not have any additional uncertainty. The systematic
 573 uncertainties (θ) enter the likelihood as additive perturbations to the transfer factors $R_i^{Z/W}$,
 574 and are modeled as Gaussians. The parameter $\mu_i^{Z \rightarrow \nu\nu}$ represents the yield of the $Z(\nu\nu) + \text{jets}$
 575 background in the i dijet mass bin into the signal region, and is left freely floating in the fit. The
 576 function $f_i(\theta)$ is the transfer factor between the $Z(\nu\nu) + \text{jets}$ and $W(\ell\nu) + \text{jets}$ backgrounds in
 577 the signal region and represents a constraint between these backgrounds. The likelihood also
 578 includes the signal region with B_i representing all the backgrounds, S representing the nominal
 579 signal prediction, and μ being the signal strength parameter also left floating in the fit.

580 7.2 Transfer factors

Transfer factors, derived from simulation, are used to link the yields of the $Z(\ell\ell) + \text{jets}$ and $W(\ell\nu) + \text{jets}$ processes in the control regions with the $Z(\nu\nu) + \text{jets}$ and $W(\ell\nu) + \text{jets}$ background estimates in the signal region. These transfer factors are defined as the ratio of expected yields of the target process in the signal region and the process being measured in the control sample. As an example:

$$R_i^Z = \frac{N_{i,MC}^{Z \rightarrow \mu^+ \mu^-}}{N_{i,MC}^{Z \rightarrow \nu\nu}} \quad (5)$$

581 where N_i is the number of events in bin i of the dijet mass distribution, R_i is the transfer fac-
 582 tor between the dimuon control region and $Z \rightarrow \nu\nu$ background. Other transfer factors are
 583 constructed in similar manner.

584 To estimate the $W(\ell\nu) + \text{jets}$ background in the signal region, the transfer factors between
 585 the $W(\mu\nu) + \text{jets}$ and $W(e\nu) + \text{jets}$ event yields in the single-lepton control samples and the
 586 $W(\ell\nu) + \text{jets}$ background estimates in the signal region are constructed. These transfer factors
 587 take into account the impact of lepton acceptances and efficiencies, lepton veto efficiencies, and
 588 the difference in the trigger efficiencies in the case of the single-electron control sample. These
 589 transfer factors are shown in Figure 44. The dotted red (blue) line shows the ratio of the pro-
 590 cesses where the V-boson is produced via EW (QCD) production where as the solid lines show
 591 the ratio of the processes where the V-boson is produced both via EW and QCD production.

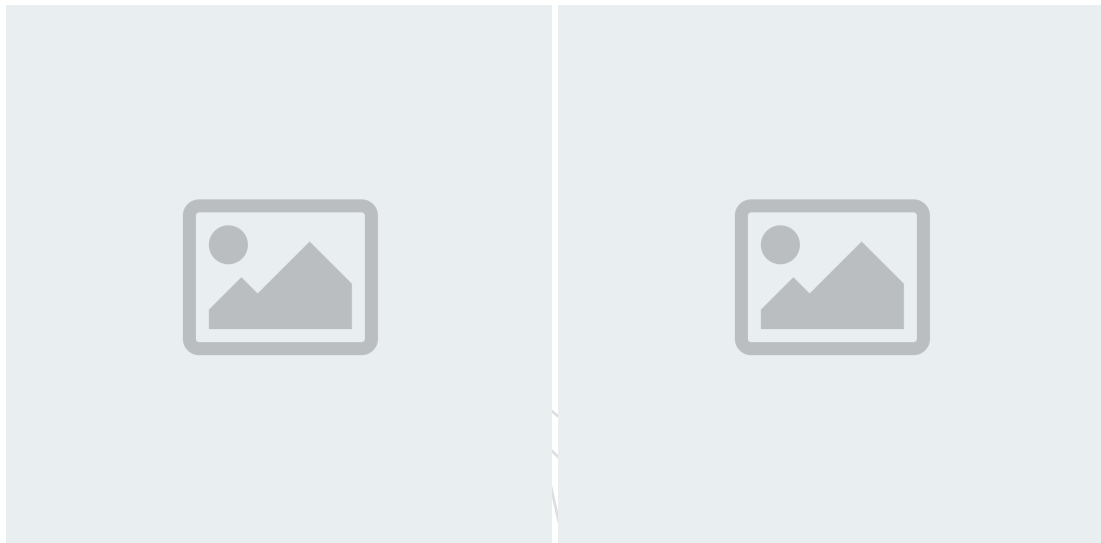


Figure 44: Transfer factors for the $W \rightarrow \ell\nu$ background as a function of the dijet mass using the single muon and single electron control regions for the vbf final state. The grey band shows the statistical and systematic uncertainties on the ratios.

592 The $Z \rightarrow \nu\nu$ background prediction in the signal region is connected to the yields of $Z \rightarrow$
 593 $\mu^+ \mu^-$ and $Z \rightarrow e^+ e^-$ events in the dilepton control samples. The associated transfer factors ac-
 594 count for the differences in the branching ratio of Z bosons to charged leptons relative to neutrino-
 595 nos and the impact of lepton acceptance and selection efficiencies. In the case of dielectron
 596 events, the transfer factor also takes into account the difference in the trigger efficiencies. The
 597 resulting constraint on the $Z \rightarrow \nu\nu$ background from the dilepton control samples is limited by
 598 the statistical uncertainty in the dilepton control samples due to the large branching fraction
 599 difference of the Z boson decays to muons and electrons compared to that to neutrinos. These
 600 transfer factors are shown in Figure 45. The dotted red (blue) line shows the ratio of the pro-
 601 cesses where the V-boson is produced via EW (QCD) production where as the solid lines show
 602 the ratio of the processes where the V-boson is produced both via EW and QCD production.

603 Finally, a transfer factor is also defined to connect the $Z(\nu\nu) + \text{jets}$ and $W(\ell\nu) + \text{jets}$ background
 604 yields in the signal region to further benefit from larger statistical power that $W(\ell\nu) + \text{jets}$ back-
 605 ground has making it possible to experimentally constrain $Z(\nu\nu) + \text{jets}$ production at high dijet
 606 masses. These transfer factors are shown in Figure 46. The dotted red (blue) line shows the
 607 ratio of the processes where the V-boson is produced via EW (QCD) production where as the
 608 solid lines show the ratio of the processes where the V-boson is produced both via EW and
 609 QCD production.

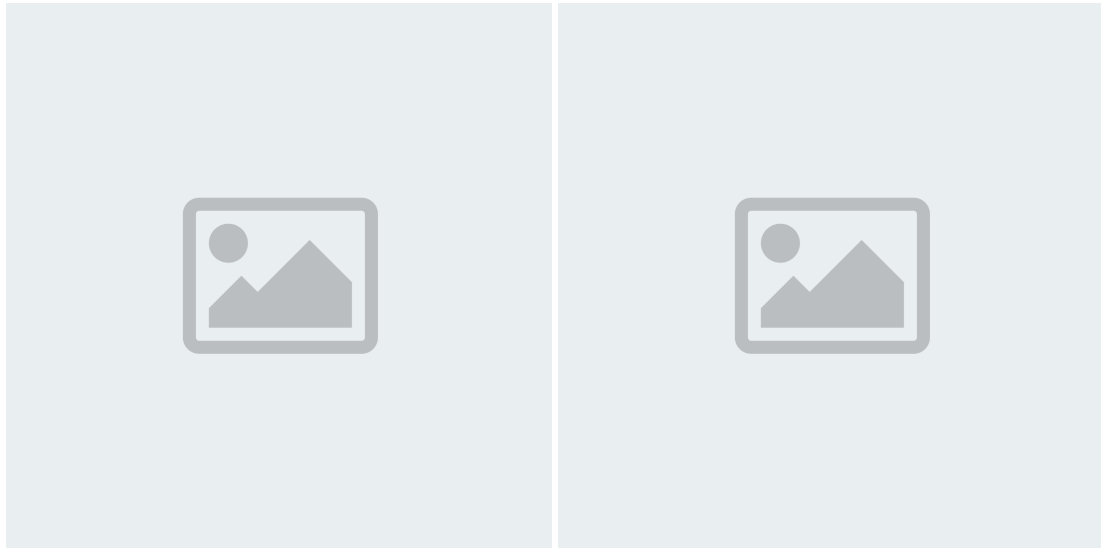


Figure 45: Transfer factors for the $Z(\nu\nu) + \text{jets}$ background as a function of the dijet mass using the dimuon, and dielectron control regions in vbf final state. The grey band shows the statistical and systematic uncertainties on the ratios.

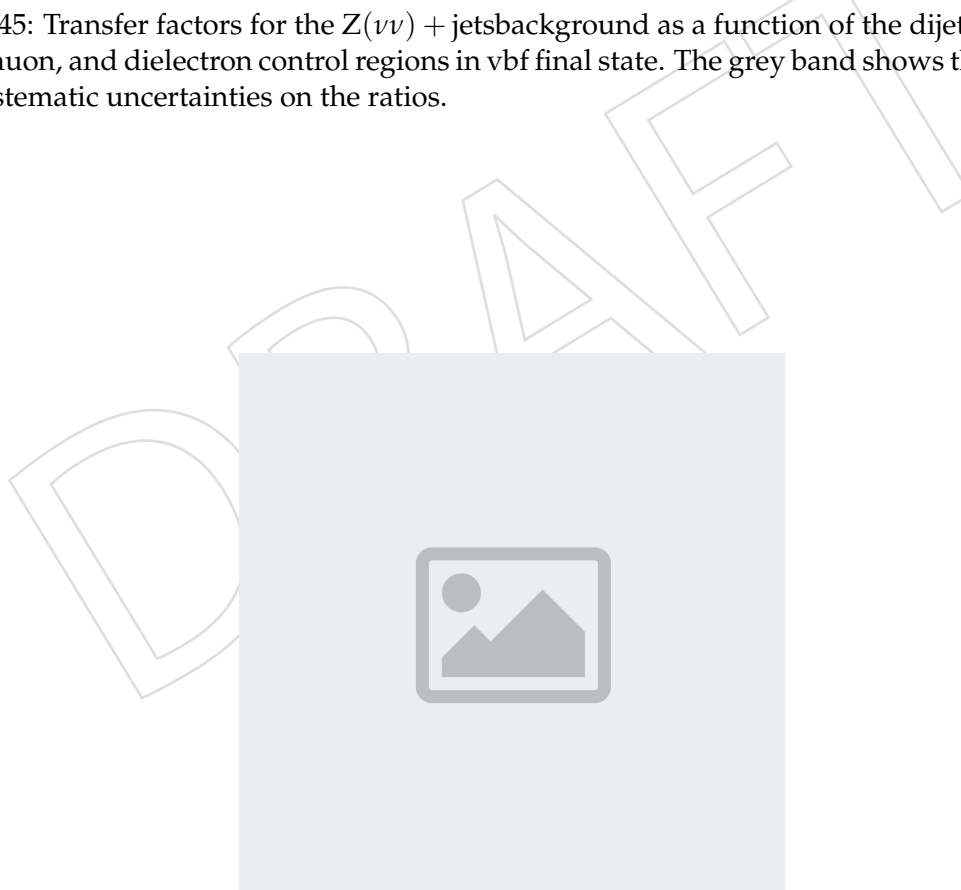


Figure 46: Transfer factors for the to estimate the $Z(\nu\nu)+\text{jets}$ background from $W+\text{jets}$ in the signal region as a function of the dijet mass for the vbf final state. The grey band shows the statistical and systematic uncertainties on the ratios.

610 7.3 Systematic uncertainties

611 Systematic uncertainties in the transfer factors are modeled as constrained nuisance parameters
612 and include both experimental and theoretical uncertainties in the $W + \text{jets}$ to $Z + \text{jets}$ differen-
613 tial cross section ratios.

614 7.3.1 Theoretical uncertainties

615 Theoretical uncertainties in $V + \text{jets}$ processes include effects from QCD and EW higher-order
616 corrections along with PDF modeling uncertainty. One of the uncertainties considered comes
617 from the variations around the central renormalization and factorization scale choice. It is eval-
618 uated by taking the differences in the NLO cross section as a function of boson p_T after chang-
619 ing the renormalization and factorization scales by a factor of two and a factor of one-half with
620 respect to the default value. These constant scale variations mainly affect the overall normal-
621 ization of the boson p_T distributions. This uncertainty is treated to be uncorrelated across the
622 $Z + \text{jets}$, $W + \text{jets}$ processes, but correlated across the bins of the dijet mass distribution.

623 The PDF uncertainty has been estimated using the standard deviations of weights provided in
624 the NNPDF3.0 parton distribution set and using the RMS of each bin of the distribution after
625 varying the full spectra by these weights. This uncertainty is treated to be correlated across the
626 $Z + \text{jets}$, $W + \text{jets}$ processes, and the bins of the dijet mass distribution.

627 The uncertainty due the EW corrections is assumed to be the full correction itself as a conser-
628 vative approach. The uncertainty is treated correlated across the processes and across the bins
629 of the dijet mass spectra.

630 These uncertainties are applied to the QCD and EW $V + \text{jets}$ processes, but are assumed to be
631 uncorrelated. That is, the QCD $W + \text{jets}$ component has a factorization scale uncertainty that is
632 the same size as the factorization scale uncertainty on the EW $W + \text{jets}$ component, but the two
633 are treated as separate nuisances in the signal extraction fit.

634 The summary of the aforementioned theoretical uncertainties including their magnitude per
635 process and on the ratio are shown in Figure 47

636 7.3.2 Experimental uncertainties

637 **Check numbers for 2017/18** Experimental uncertainties including the reconstruction efficiency
638 (1% per muon or electron), and selection efficiencies of leptons (1% per muon and 2% per
639 electron), and hadronically decaying τ leptons (5%) are incorporated to the analysis. These
640 reconstruction and selection efficiencies further translate into an uncertainty in the lepton veto
641 efficiency of 3%. The lepton veto uncertainties in the transfer factors and are estimated through
642 propagating the overall uncertainty on the tagging scale factor (loose-muon ID, veto-electron
643 ID and loose MVA-tau ID) into the vetoed selection based on both the flavour composition
644 of the $W + \text{jets}$ process the acceptance of the lepton. The overall magnitude of the lepton-
645 veto uncertainty is found to be around 3 (4)% and is found to be dominated by the τ -veto
646 uncertainty.

647 The uncertainty in the modeling of E_T^{miss} in simulation [31] is estimated to be 1-2% on the ratios
648 and is dominated by the uncertainty on the jet energy scale. The jet energy scale uncertainties
649 found to be not-cancelling in the ratio due to the differences in the jet kinematics between
650 control and signal regions. The resulting jet energy scale uncertainties in the ratios can be seen
651 in Figure 48

652 Lastly, uncertainties in the efficiency of the electron (2%), and p_T^{miss} (2%) triggers, are included

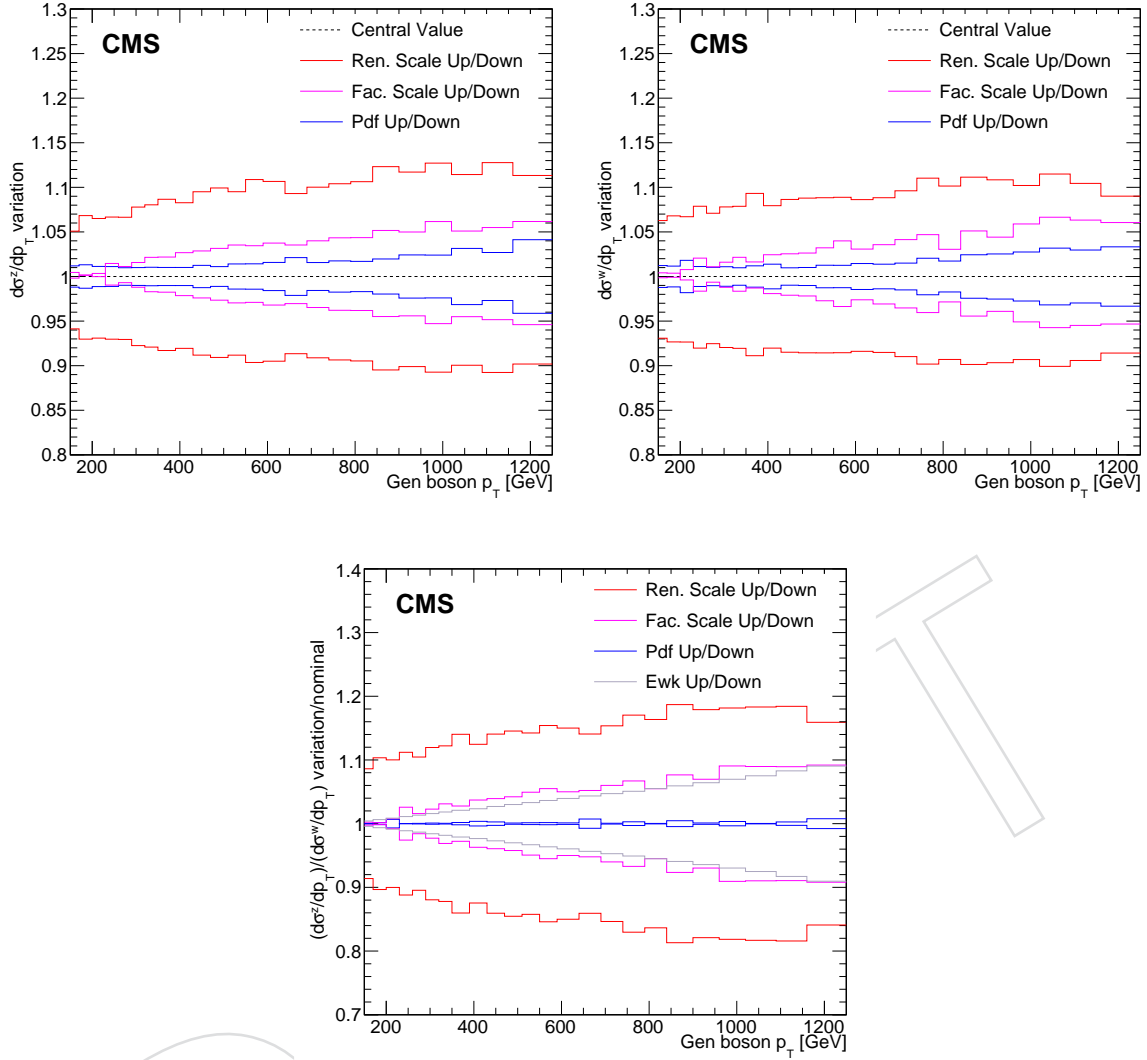


Figure 47: Theoretical uncertainties due to QCD and EW higher-order corrections and the PDF variation is shown for individual processes and for the ratio.

and are fully correlated across all the bins of dijet mass distribution.

The remaining uncertainties are for the monte carlo based backgrounds. A systematic uncertainty of 10% for the top quark background due to the modeling of the top quark p_T distribution in simulation. The uncertainty in the efficiency of the b jet veto is estimated to be 3% (1%) for the top quark (diboson) background. In addition, systematic uncertainties of 10 and 20% are included in the normalizations of the top quark [32] and diboson backgrounds [33, 34], respectively, to account for the uncertainties in their cross sections in the relevant kinematic phase space. Lastly, the uncertainty in the QCD multijet background estimate is found to be between 50–150% due to the variations of the jet response and the statistical uncertainty of the extrapolation factors.

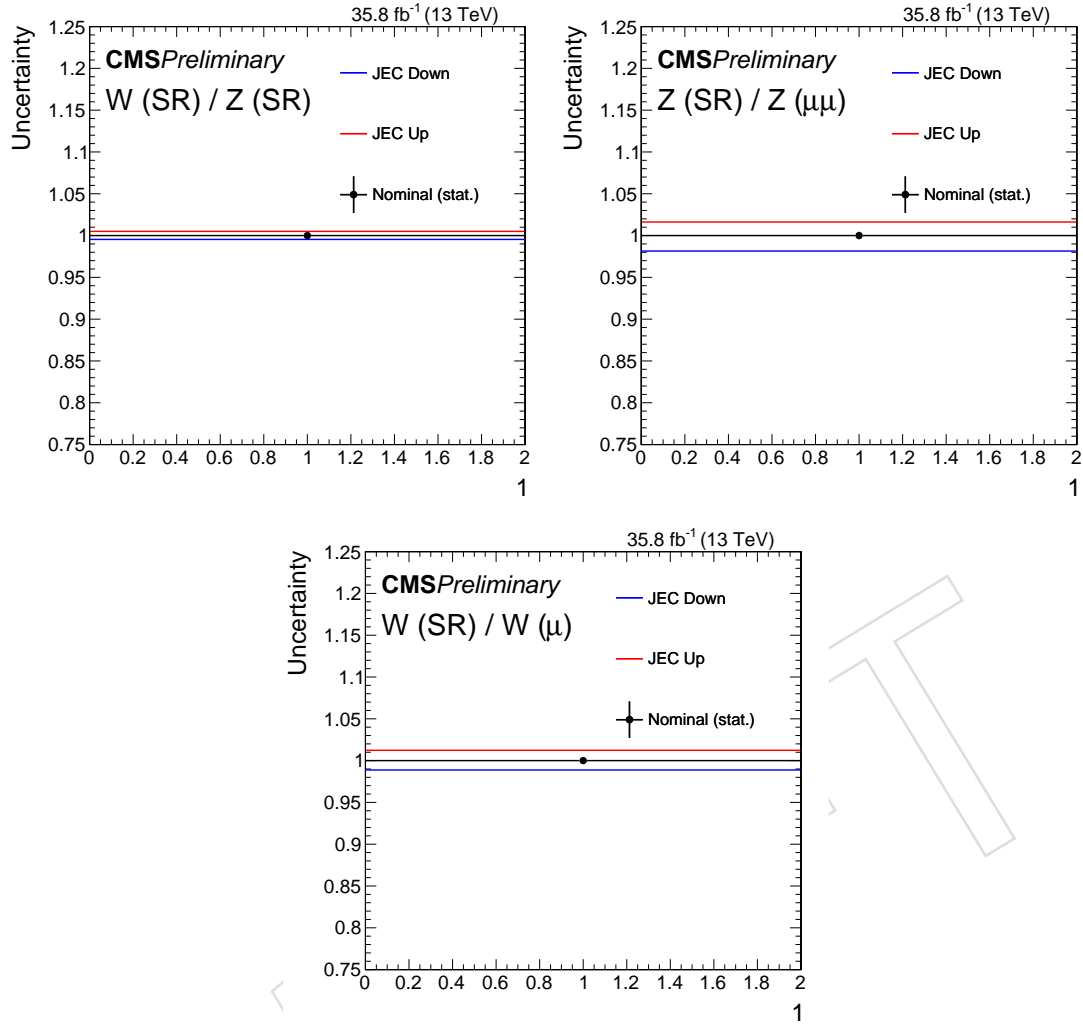


Figure 48: Redo for 2017/18 The resulting jet energy scale uncertainties in the ratios of W_{SR}/Z_{vv} , $Z_{vv}/Z_{\mu\mu}$ and $W_{\text{SR}}/W_{\mu\nu}$, respectively.

663 7.4 Control sample validation

664 An important cross-check of the application of p_T -dependent NLO QCD and EW corrections is
 665 represented by the agreement between data and simulation in the ratio of $Z + \text{jets}$ events and
 666 $W + \text{jets}$ events in the control samples as a function of m_{jj} .

667 Figure 49 shows the ratio between $Z(\mu\mu) + \text{jets}$ and $W(\mu\nu) + \text{jets}$ (left), and the one between
 668 $Z(ee) + \text{jets}$ and $W(ev) + \text{jets}$ processes (right) as a function of the dijet mass distribution for
 669 events selected both using 2017 samples (top) and 2018 samples (bottom). Good agreement is
 670 observed between data and simulation after the application of the NLO corrections.

671 7.5 QCD multijet estimation

672 Update for 2017/18

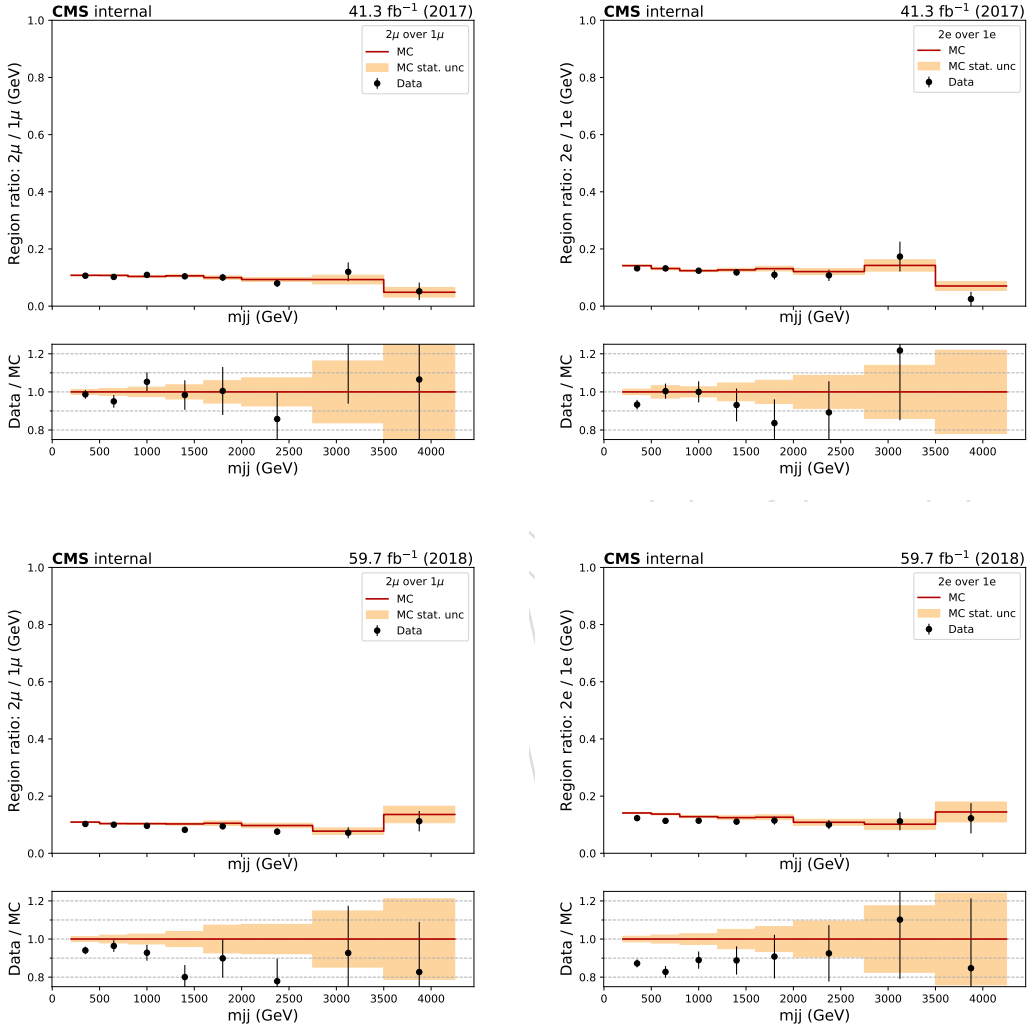


Figure 49: Comparison between data and MC simulation for $Z(\mu\mu) + \text{jets}$ and $W(\mu\nu) + \text{jets}$ (left), $Z(ee) + \text{jets}$ and $W(e\nu) + \text{jets}$ processes (right) ratio as a function of m_{jj} , using 2017 samples (top) and 2018 samples (bottom). The gray bands include both the pre-fit systematic uncertainties and the statistical uncertainty in the simulation.

Source	Process	Uncertainty
Electron trigger E_T^{miss} trigger	$W_{SR}/W_{ev}, Z_{vv}/Z_{ee}$	1%
	$W_{SR}/W_{CR}, Z_{vv}/Z_{CR}, Z/W,$	2%
Muon-reco efficiency	$W_{SR}/W_{\mu\nu}, Z_{vv}/Z_{\mu\mu}$	1% (per leg)
Muon-ID efficiency	$W_{SR}/W_{\mu\nu}, Z_{vv}/Z_{\mu\mu}$	1% (per leg)
Muon-Iso efficiency	$W_{SR}/W_{\mu\nu}, Z_{vv}/Z_{\mu\mu}$	0.5% (per leg)
Electron-reco efficiency	$W_{SR}/W_{ev}, Z_{vv}/Z_{ee}$	1% (per leg)
Electron-IDiso efficiency	$W_{SR}/W_{ev}, Z_{vv}/Z_{ee}$	1.5% (per leg)
Lepton veto	W_{LSR}	3% (QCD), 5.0% (EW)
Jet energy scale	W_{CR}/W_{SR}	2%
Jet energy scale	Z_{CR}/Z_{SR}	1%

Table 12: **Check numbers for 2017/18** Summary of experimental uncertainties affecting used in the analysis.

673 **8 Results**

DRAFT

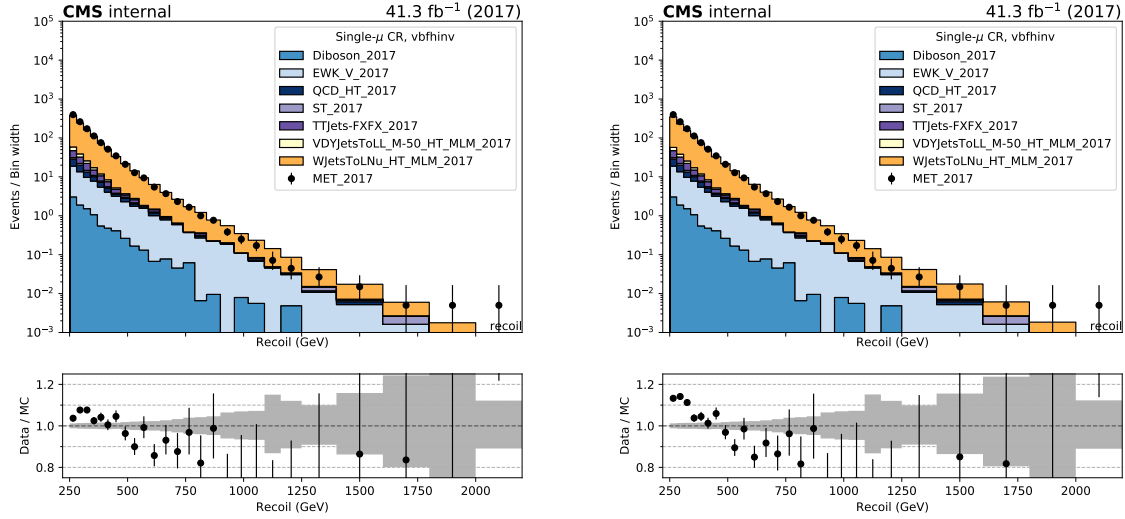


Figure 50: The recoil distribution in the single muon CR for the case in which 1D k-factors are used (left), compared to the case in which 2D k-factors are used (right), using 2017 samples.

674 A Comparison of 1D and 2D QCD k-factors

675 In this appendix, several distributions such as recoil, M_{jj} and $\Delta\eta_{jj}$ are compared for two cases
676 in the single muon control region:

- 677 • Plots with 1D k-factors applied: Function of gen-boson p_T
- 678 • Plots with 2D k-factors applied: Function of gen-boson p_T and M_{jj}

679 Both k-factors are derived from samples in which the VBF selections are applied at the gen level.
680 1D k-factor is a function of generator level vector boson p_T , whereas 2D k-factor is a function
681 of both generator level boson p_T and M_{jj} . The distributions are shown in the following pages.

682 Fig. 50 shows the comparison of the recoil distribution with 2017 samples, while Fig. 51 shows
683 the same comparison with 2018 samples. Fig. 52 shows the comparison of the M_{jj} distribution
684 with 2017 samples, while Fig. 53 shows the same comparison with 2018 samples. Fig. 54 shows
685 the comparison of the $\Delta\eta_{jj}$ distribution with 2017 samples, while Fig. 55 shows the same com-
686 parison with 2018 samples. Fig. 56 shows the comparison of the muon p_T distribution with
687 2017 samples, while Fig. 57 shows the same comparison with 2018 samples. Fig. 58 shows
688 the comparison of the muon η distribution with 2017 samples, while Fig. 59 shows the same
689 comparison with 2018 samples.

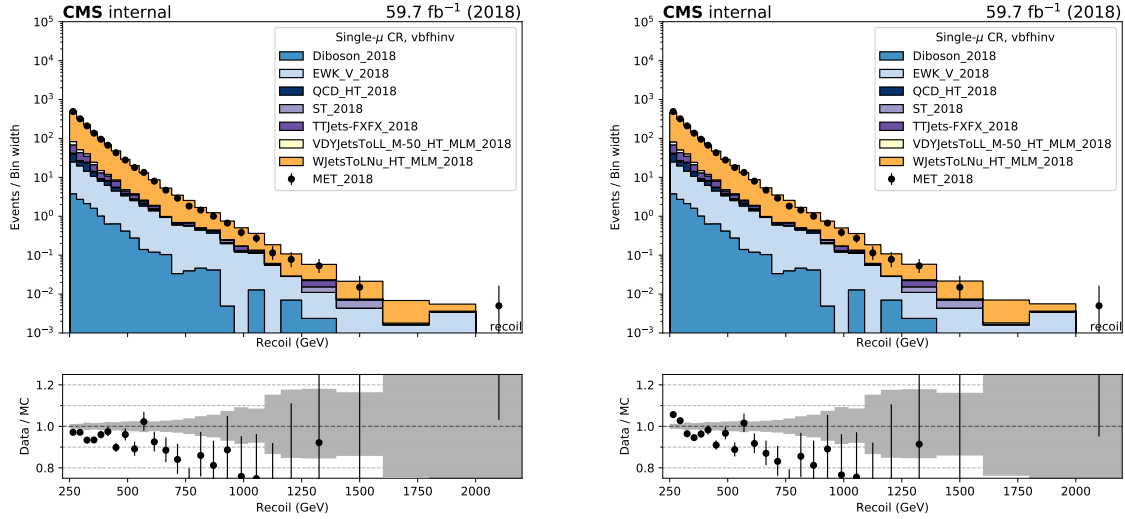


Figure 51: The recoil distribution in the single muon CR for the case in which 1D k-factors are used (left), compared to the case in which 2D k-factors are used (right), using 2018 samples.

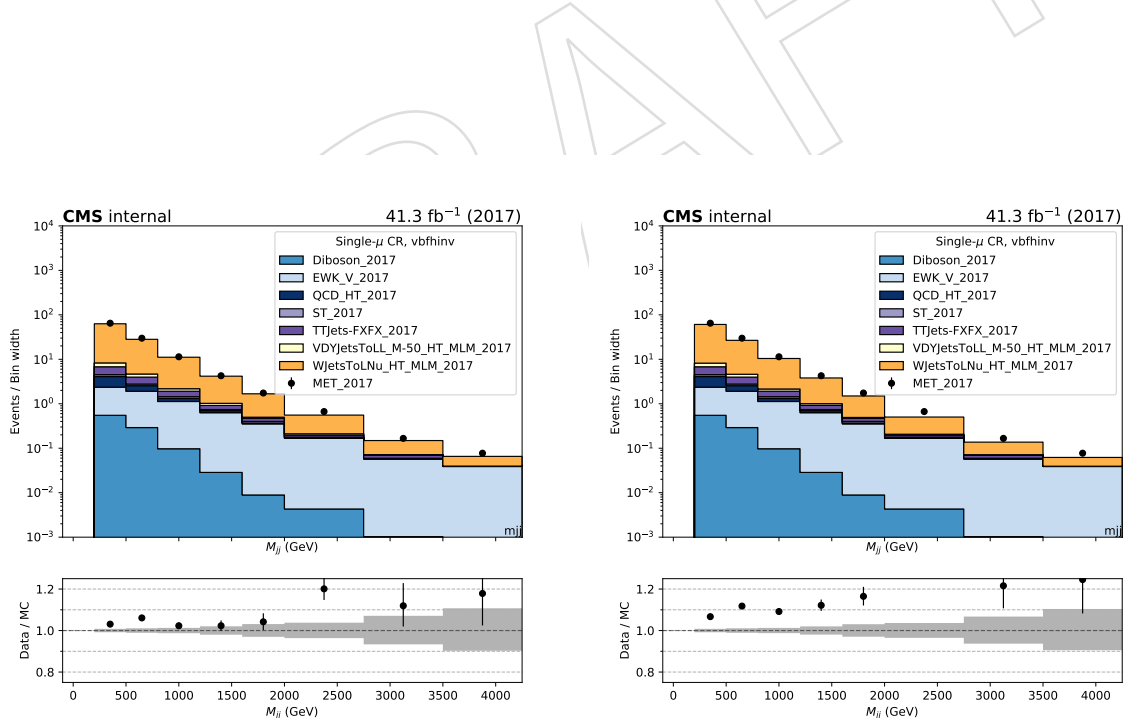


Figure 52: The M_{jj} distribution in the single muon CR for the case in which 1D k-factors are used (left), compared to the case in which 2D k-factors are used (right), using 2017 samples.

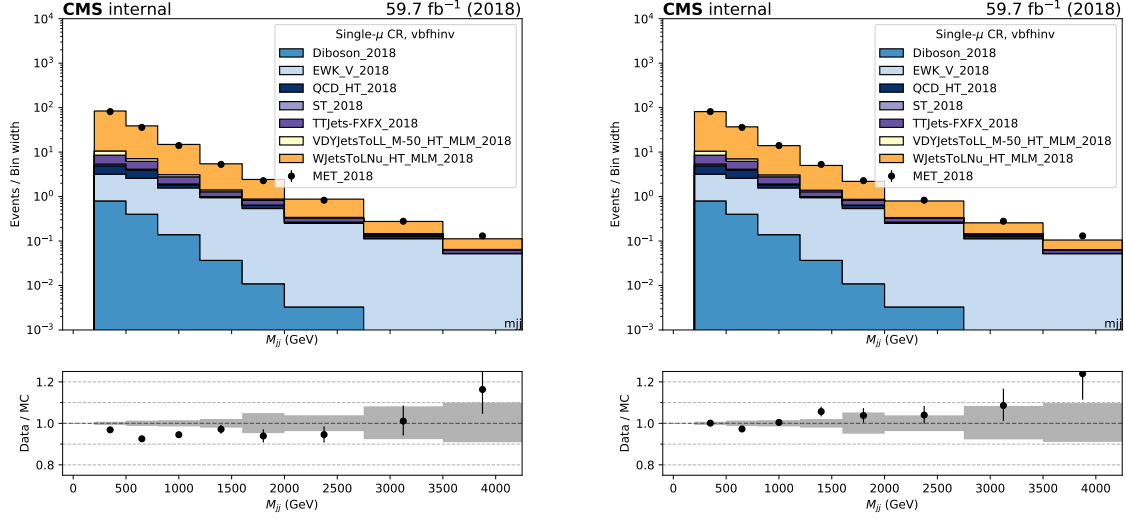


Figure 53: The M_{jj} distribution in the single muon CR for the case in which 1D k-factors are used (left), compared to the case in which 2D k-factors are used (right), using 2018 samples.

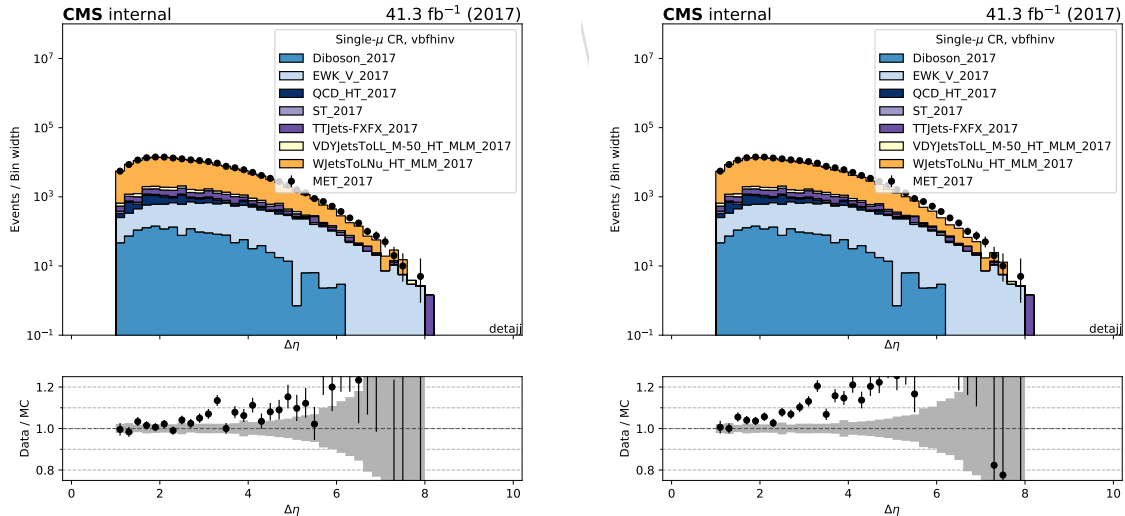


Figure 54: The $\Delta\eta_{jj}$ distribution in the single muon CR for the case in which 1D k-factors are used (left), compared to the case in which 2D k-factors are used (right), using 2017 samples.

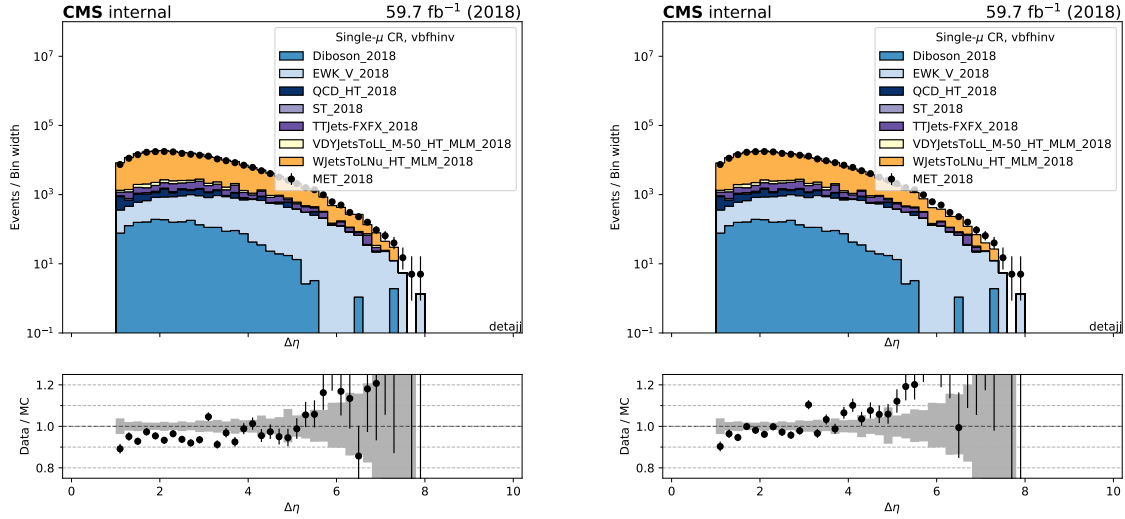


Figure 55: The $\Delta\eta_{jj}$ distribution in the single muon CR for the case in which 1D k-factors are used (left), compared to the case in which 2D k-factors are used (right), using 2018 samples.

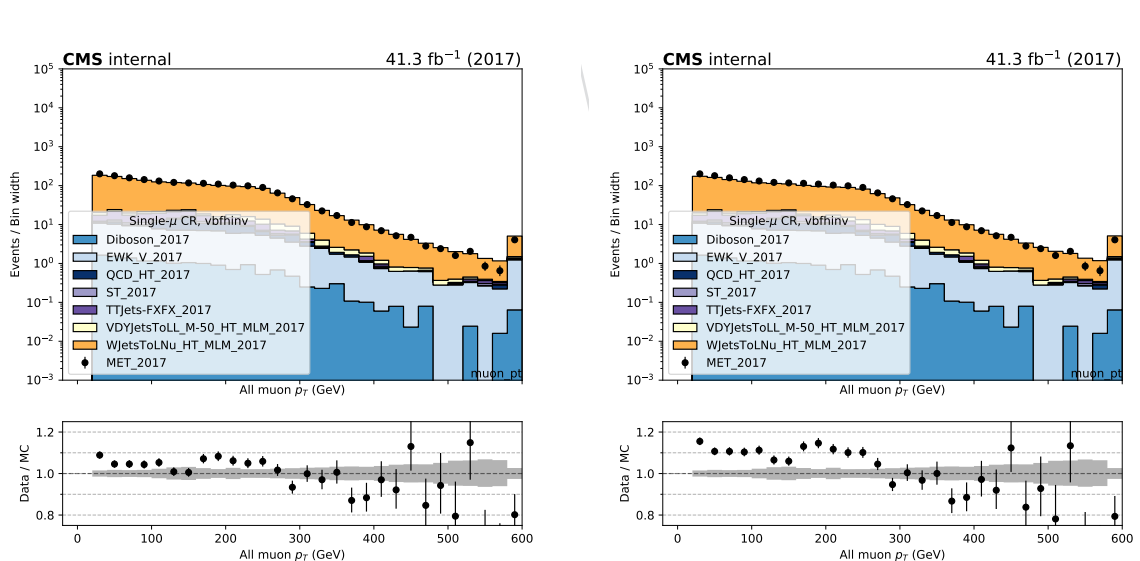


Figure 56: The muon p_T distribution in the single muon CR for the case in which 1D k-factors are used (left), compared to the case in which 2D k-factors are used (right), using 2017 samples.

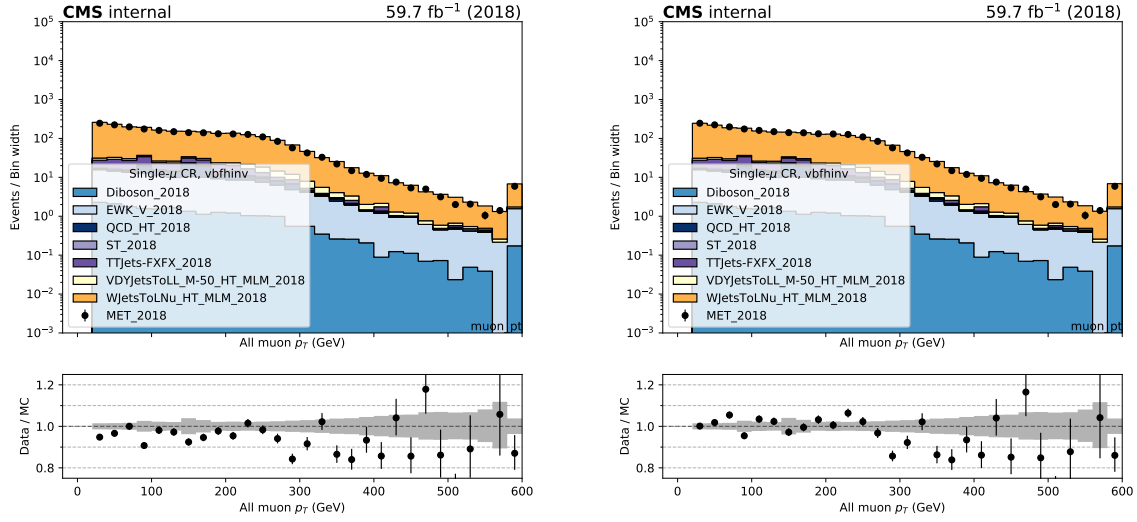


Figure 57: The muon p_T distribution in the single muon CR for the case in which 1D k-factors are used (left), compared to the case in which 2D k-factors are used (right), using 2018 samples.

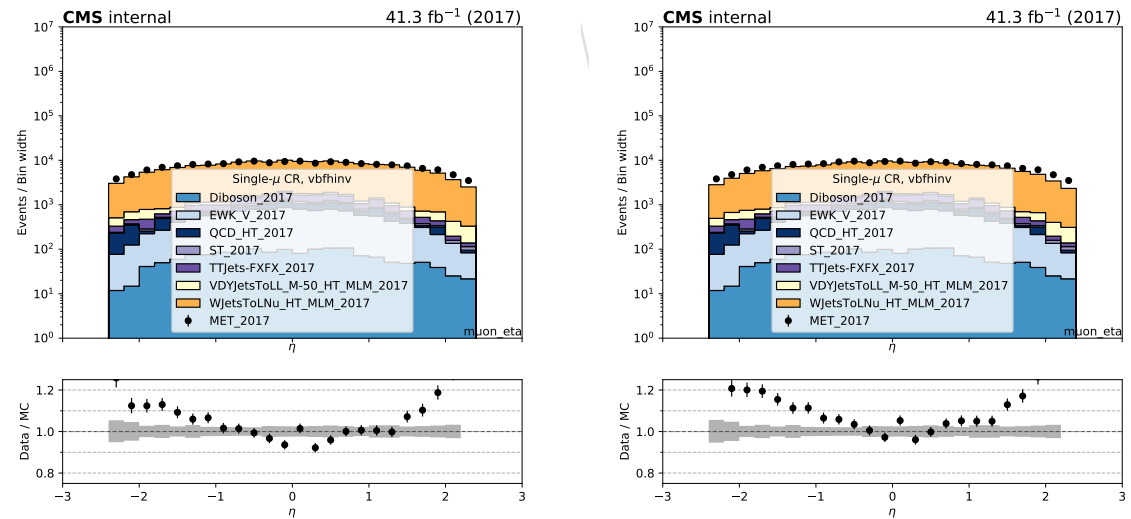


Figure 58: The muon η distribution in the single muon CR for the case in which 1D k-factors are used (left), compared to the case in which 2D k-factors are used (right), using 2017 samples.

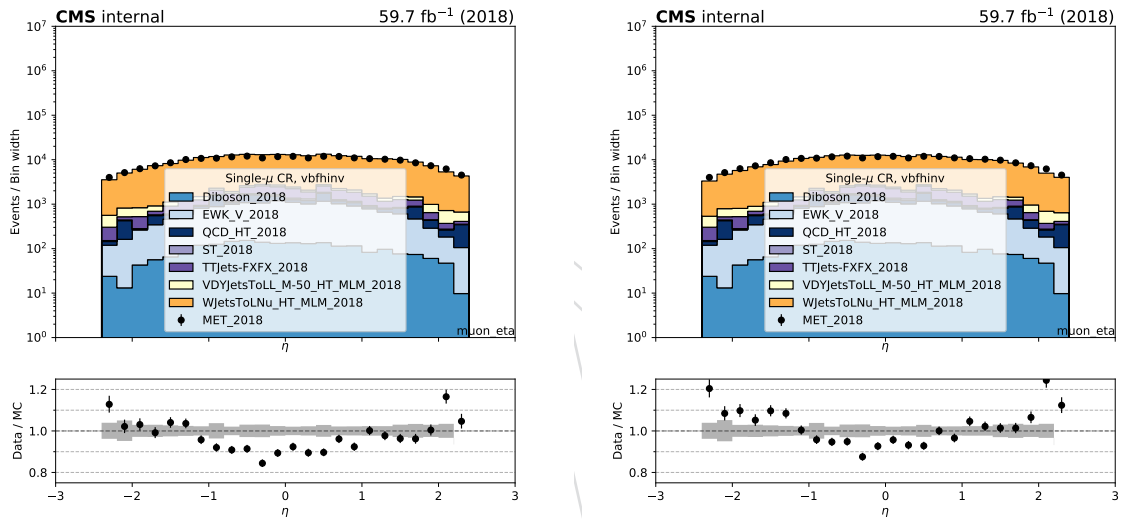


Figure 59: The muon η distribution in the single muon CR for the case in which 1D k-factors are used (left), compared to the case in which 2D k-factors are used (right), using 2018 samples.

690 B Trigger efficiencies in double muon CR

691 In this section, the efficiencies of $p_T^{\text{miss}} + H_T^{\text{miss}}$ triggers measured in double muon control region
 692 are presented. In addition, efficiencies of these triggers as a function of m_{jj} both in single muon
 693 and double muon control region are also presented.

694 Fig. 60 shows the efficiencies as a function of M_{jj} in data and MC for the three categories in
 695 2017, whereas Fig. 61 shows the efficiencies as a function of M_{jj} in data and MC for the three
 696 categories in 2018.

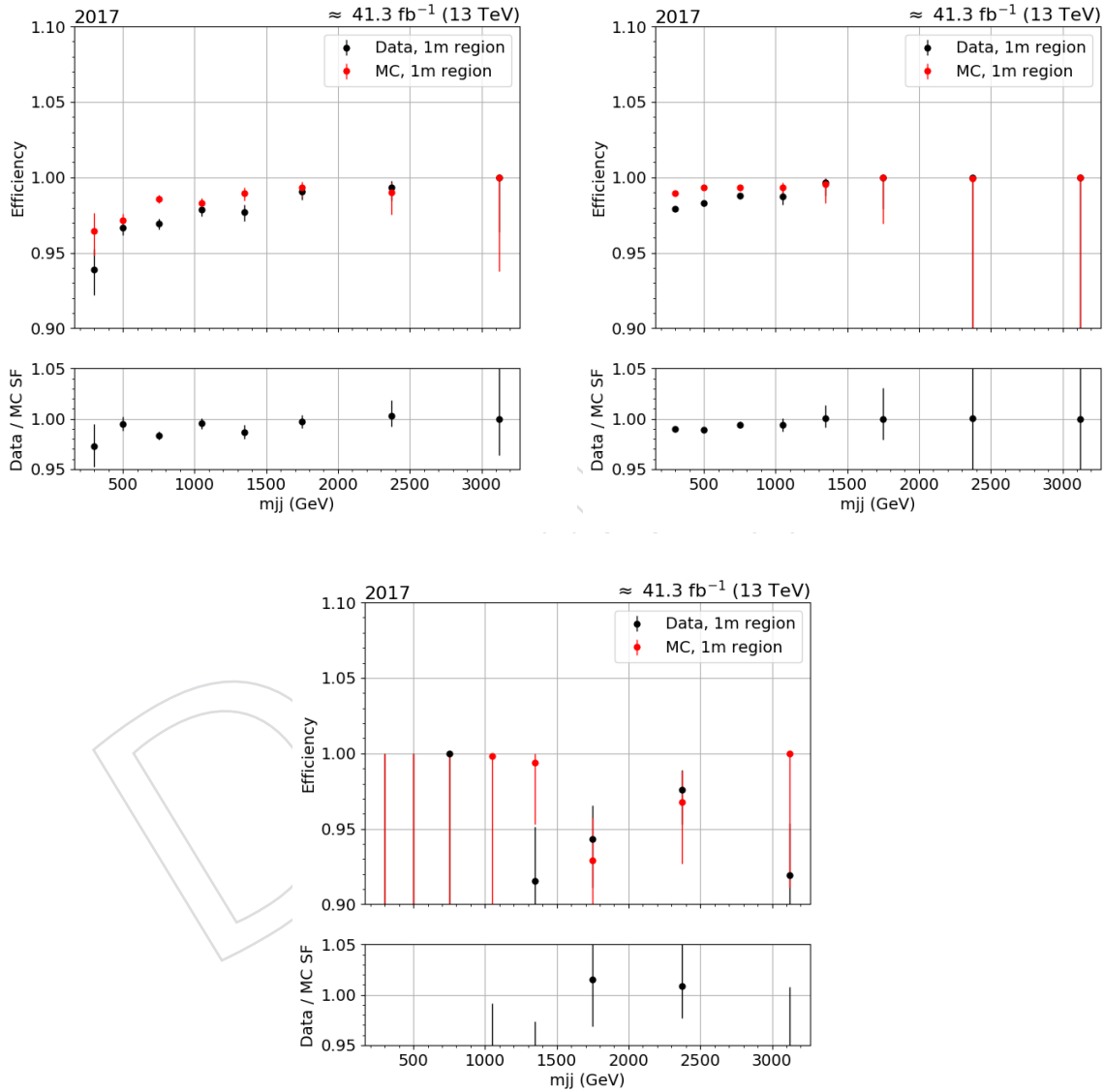


Figure 60: MET trigger efficiency as a function of m_{jj} in three categories: One forward jet and one central jet, two central jets and two forward jets. These results are obtained from 2017 data and MC samples with the selection of single muon events.

697 Figs. 62 and ?? show the efficiencies obtained in double muon CR as a function of recoil in data
 698 and MC for the three jet categories in 2017 and 2018, respectively. Figs. 64 and ?? show the
 699 efficiencies obtained in double muon CR as a function of M_{jj} in data and MC for the three jet

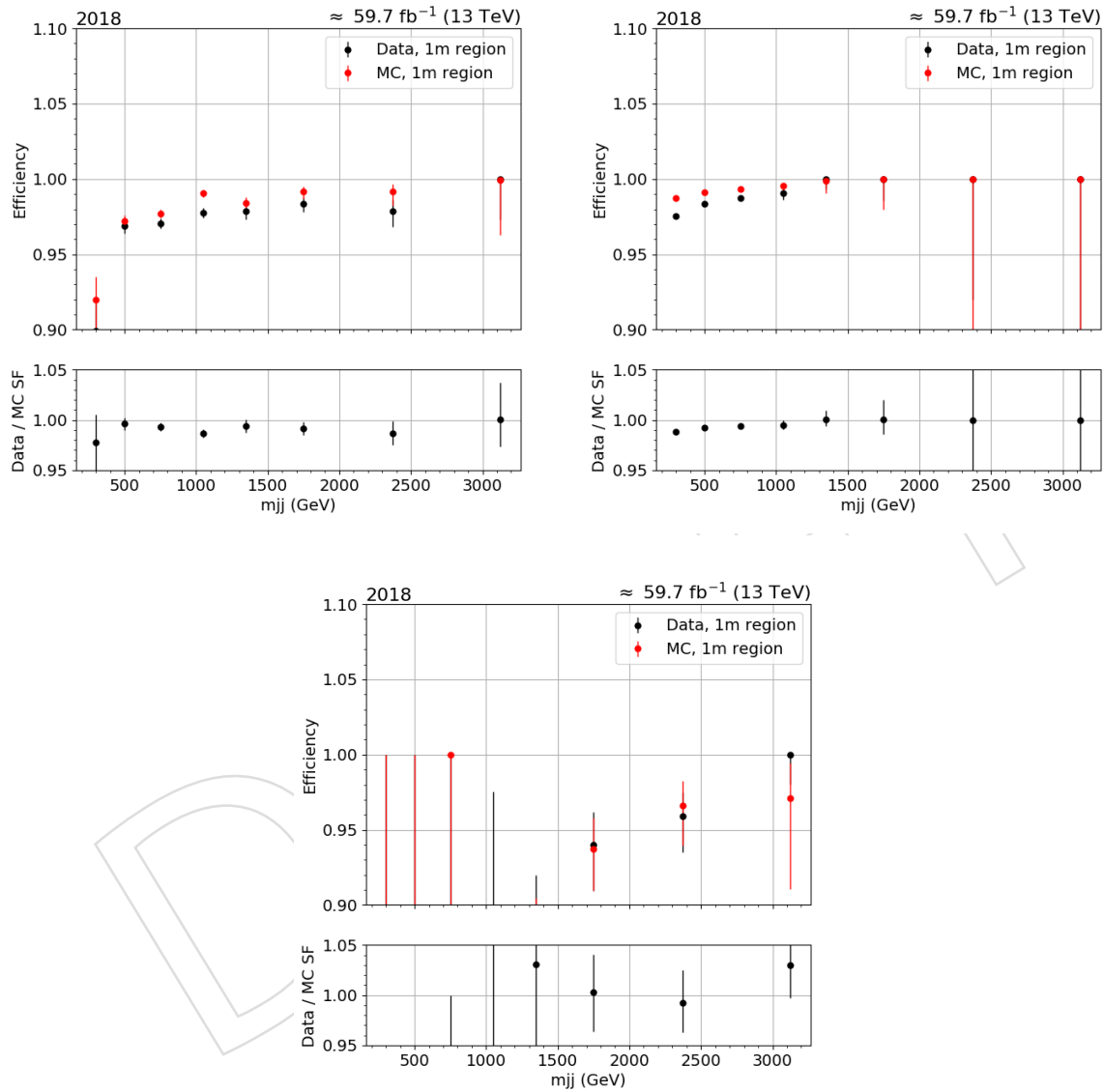


Figure 61: MET trigger efficiency as a function of m_{jj} in three categories: One forward jet and one central jet, two central jets and two forward jets. These results are obtained from 2018 data and MC samples with the selection of single muon events.

700 categories in 2017 and 2018, respectively.

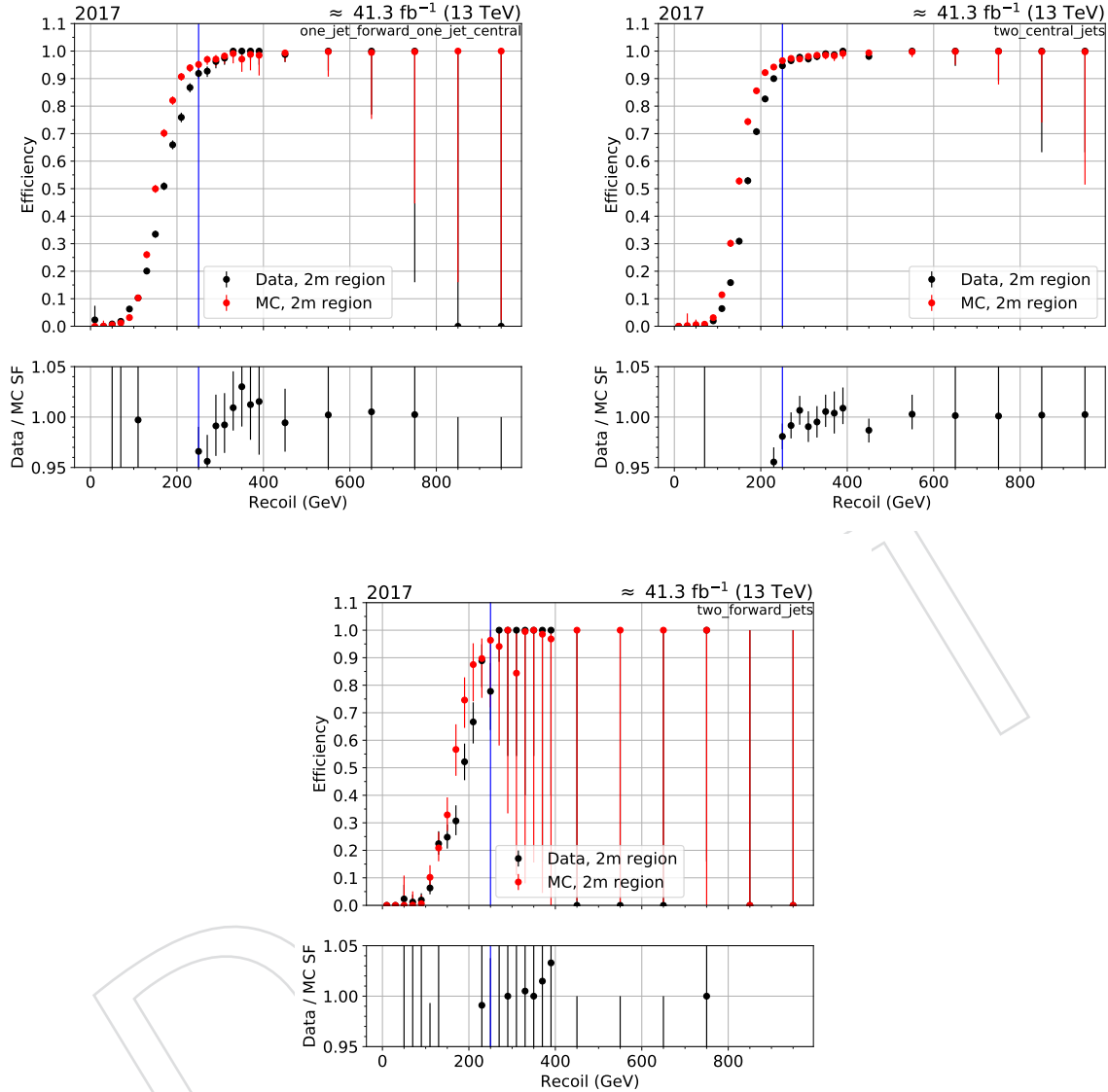


Figure 62: MET trigger efficiency as a function of recoil in three categories: One forward jet and one central jet, two central jets and two forward jets. These results are obtained from 2017 data and MC samples with the selection of double muon events.

701 Fig. 66 shows the scale factors as a function of recoil in double muon control region, using 2017
 702 (right) samples.

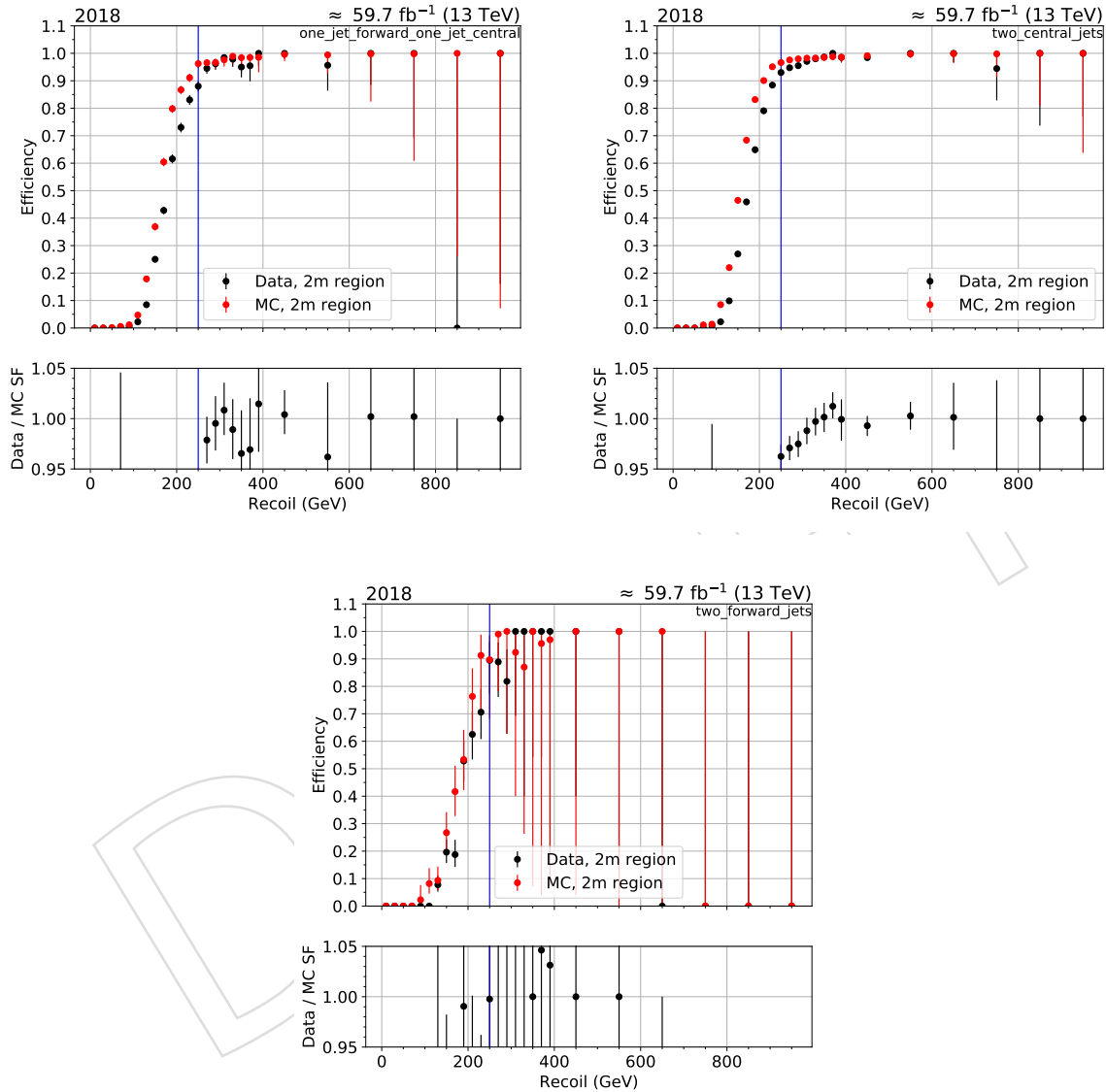


Figure 63: MET trigger efficiency as a function of recoil in three categories: One forward jet and one central jet, two central jets and two forward jets. These results are obtained from 2018 data and MC samples with the selection of double muon events.

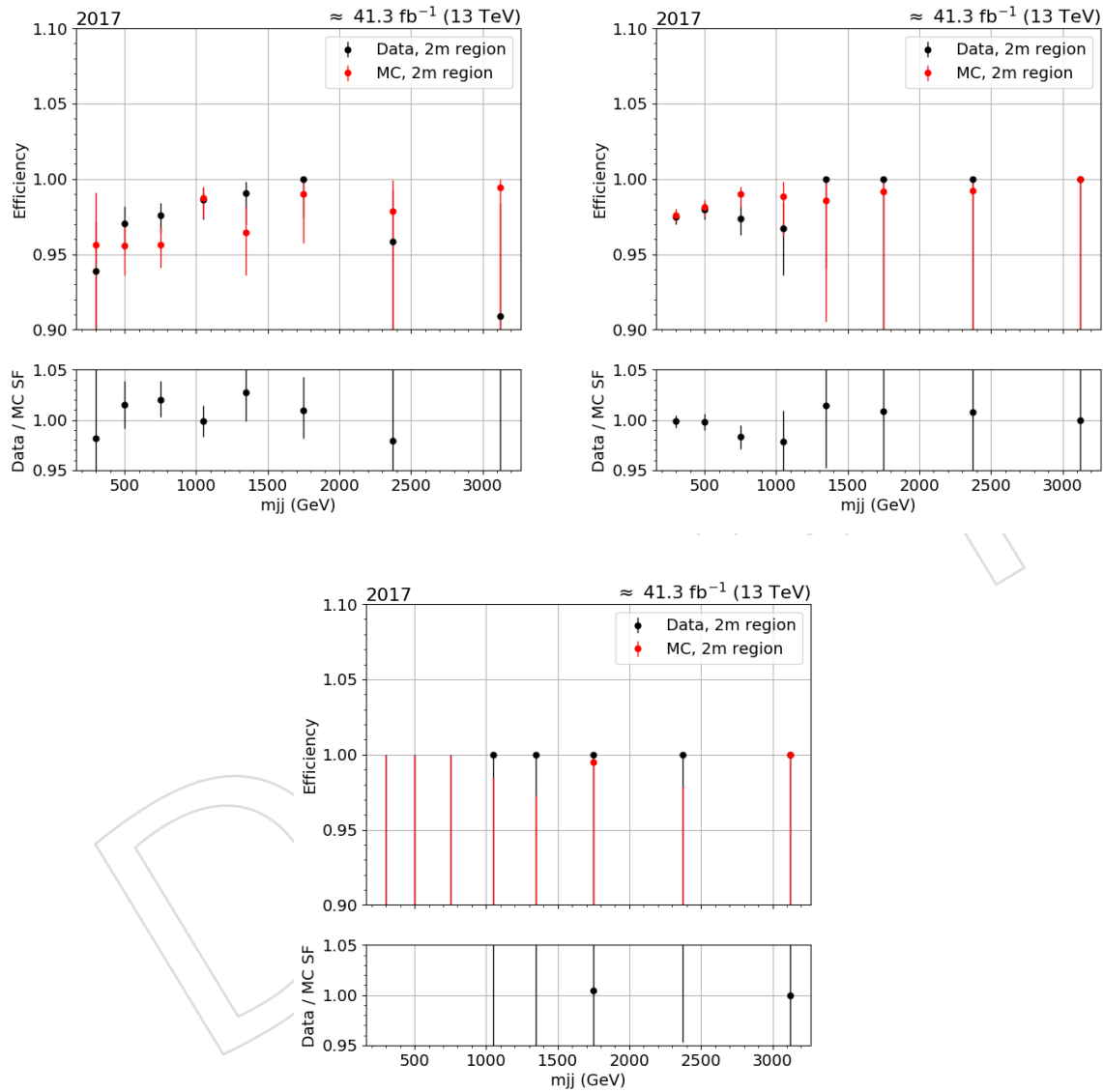


Figure 64: MET trigger efficiency as a function of m_{jj} in three categories: One forward jet and one central jet, two central jets and two forward jets. These results are obtained from 2017 data and MC samples with the selection of double muon events.

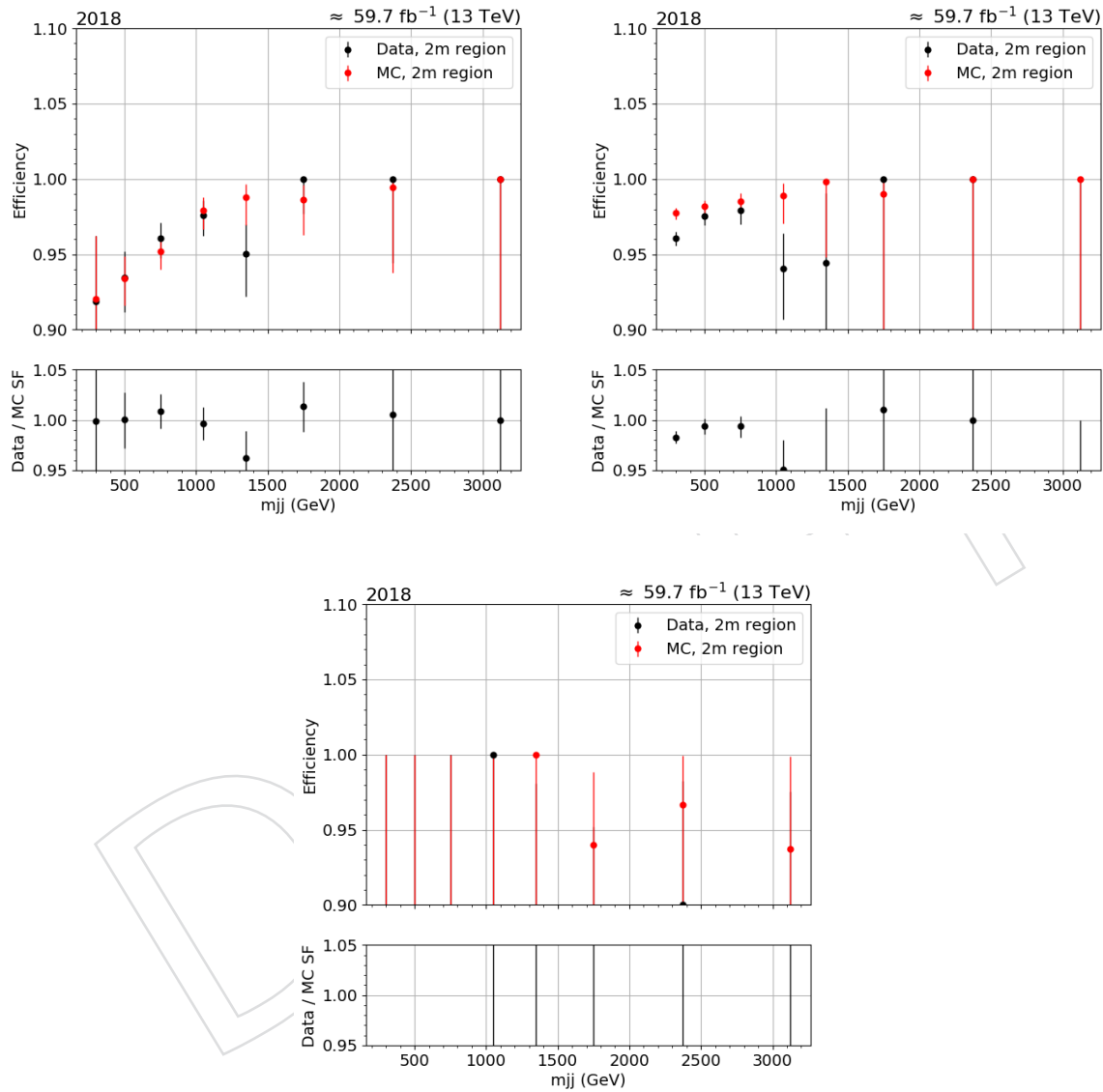


Figure 65: MET trigger efficiency as a function of m_{jj} in three categories: One forward jet and one central jet, two central jets and two forward jets. These results are obtained from 2018 data and MC samples with the selection of double muon events.

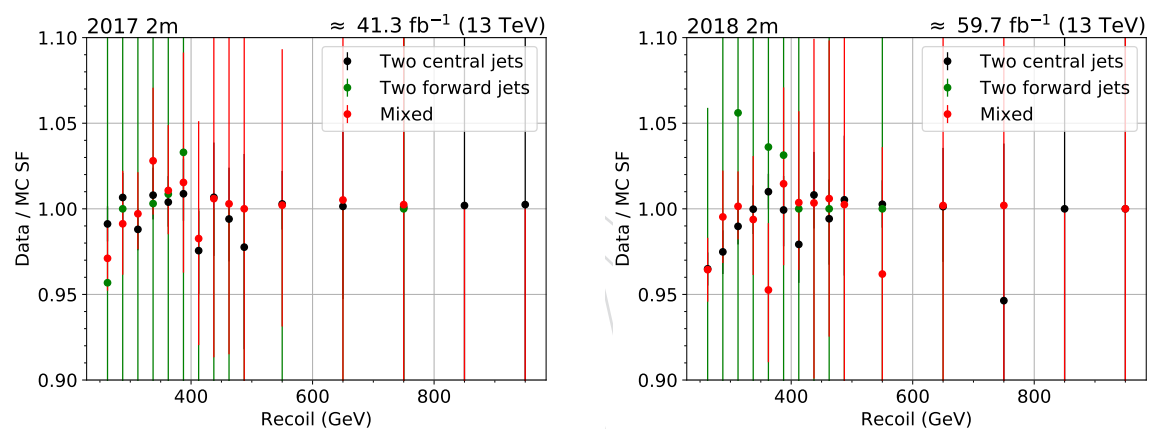


Figure 66: Data-MC scale factors for the three jet kinematic cases in the double muon control region, using 2017 (left) and 2018 (right) samples.

703 Acknowledgments

704 References

- 705 [1] CMS Collaboration, “Extraction and validation of a new set of CMS PYTHIA8 tunes from
706 underlying-event measurements”, arXiv:1903.12179.
- 707 [2] M. L. Mangano, M. Moretti, F. Piccinini, and M. Treccani, “Matching matrix elements and
708 shower evolution for top-quark production in hadronic collisions”, *JHEP* **01** (2007) 013,
709 doi:10.1088/1126-6708/2007/01/013, arXiv:hep-ph/0611129.
- 710 [3] R. Frederix and S. Frixione, “Merging meets matching in MC@NLO”, *JHEP* **12** (2012)
711 061, doi:10.1007/JHEP12(2012)061, arXiv:1209.6215.
- 712 [4] NNPDF Collaboration, “Parton distributions from high-precision collider data”, *Eur.
713 Phys. J.* **C77** (2017), no. 10, 663, doi:10.1140/epjc/s10052-017-5199-5,
714 arXiv:1706.00428.
- 715 [5] GEANT4 Collaboration, “GEANT4: A simulation toolkit”, *Nucl. Instrum. Meth. A* **506**
716 (2003) 250, doi:10.1016/S0168-9002(03)01368-8.
- 717 [6] LHC Higgs Cross Section Working Group Collaboration, “Handbook of LHC Higgs cross
718 sections: 4. deciphering the nature of the Higgs sector”,
719 doi:10.2172/1345634, 10.23731/CYRM-2017-002, arXiv:1610.07922.
- 720 [7] CMS EGamma POG, “EgHLTRunIISummary”.
721 <https://twiki.cern.ch/twiki/bin/view/CMS/EgHLTRunIISummary>.
- 722 [8] M. Cacciari, G. P. Salam, and G. Soyez, “The anti- k_t jet clustering algorithm”, *JHEP* **04**
723 (2008) 063, doi:10.1088/1126-6708/2008/04/063, arXiv:0802.1189.
- 724 [9] M. Cacciari, G. P. Salam, and G. Soyez, “FastJet user manual”, *Eur. Phys. J. C* **72** (2012)
725 1896, doi:10.1140/epjc/s10052-012-1896-2, arXiv:1111.6097.
- 726 [10] CMS Collaboration, “Jet energy scale and resolution in the CMS experiment in pp
727 collisions at 8 TeV”, *JINST* **12** (2017) P02014,
728 doi:10.1088/1748-0221/12/02/P02014, arXiv:1607.03663.
- 729 [11] CMS Collaboration, “Identification of heavy-flavour jets with the CMS detector in pp
730 collisions at 13 TeV”, *JINST* **13** (2018), no. 05, P05011,
731 doi:10.1088/1748-0221/13/05/P05011, arXiv:1712.07158.
- 732 [12] CMS JME POG. <https://twiki.cern.ch/twiki/bin/view/CMS/MissingETOptionalFiltersRun2>.
- 734 [13] CMS Collaboration, “Performance of electron reconstruction and selection with the CMS
735 detector in proton-proton collisions at $\sqrt{s} = 8$ TeV”, *JINST* **10** (2015) P06005,
736 doi:10.1088/1748-0221/10/06/P06005, arXiv:1502.02701.
- 737 [14] CMS Collaboration, “Description and performance of track and primary-vertex
738 reconstruction with the CMS tracker”, *JINST* **9** (2014) P10009,
739 doi:10.1088/1748-0221/9/10/P10009, arXiv:1405.6569.
- 740 [15] CMS EGamma POG. https://twiki.cern.ch/twiki/bin/viewauth/CMS/CutBasedElectronIdentificationRun2#Spring15_selection_25ns.

- 742 [16] CMS Collaboration, "Performance of CMS muon reconstruction in pp
743 collision events at $\sqrt{s} = 7 \text{ TeV}$ ", *JINST* **7** (2012) P10002,
744 doi:10.1088/1748-0221/7/10/P10002, arXiv:1206.4071.
- 745 [17] CMS Muon POG. https://twiki.cern.ch/twiki/bin/view/CMS/SWGuideMuonIdRun2#Loose_Muon.
- 746 [18] CMS Muon POG. https://twiki.cern.ch/twiki/bin/view/CMS/SWGuideMuonIdRun2#Tight_Muon.
- 747 [19] CMS Collaboration, "Reconstruction and identification of τ lepton decays to hadrons and
748 ν_τ at CMS", *JINST* **11** (2016) P01019, doi:10.1088/1748-0221/11/01/P01019,
749 arXiv:1510.07488.
- 750 [20] tau-POG. https://twiki.cern.ch/twiki/bin/view/CMS/TauIDRecommendation13TeV#Measurement_in_Z_tautau_events.
- 751 [21] CMS Collaboration, "Performance of photon reconstruction and identification with the
752 CMS detector in proton-proton collisions at $\sqrt{s} = 8 \text{ TeV}$ ", *JINST* **10** (2015) P08010,
753 doi:10.1088/1748-0221/10/08/P08010, arXiv:1502.02702.
- 754 [22] CMS EGamma POG. https://twiki.cern.ch/twiki/bin/viewauth/CMS/CutBasedPhotonIdentificationRun2#SPRING15_selections_bunch_crossi.
- 755 [23] CMS Lumi POG. https://twiki.cern.ch/twiki/bin/view/CMS/PileupJSONfileforData#Pileup_JSON_Files_For_Run_II.
- 756 [24] CMS Muon POG. <https://twiki.cern.ch/twiki/bin/view/CMS/MuonReferenceSelectionAndCalibrationsRun2>.
- 757 [25] J. M. Lindert et al., "Precise predictions for V+jets dark matter backgrounds", (2017).
758 arXiv:1705.04664.
- 759 [26] "Search for vbf higgs boson decays to invisible particles with 2016 dataset", 2017. CMS
760 Analysis Note : AN-17-267. http://cms.cern.ch/iCMS/jsp/openfile.jsp?tp=draft&files=AN2017_267_v4.pdf.
- 761 [27] CMS Collaboration, "Performance of missing transverse momentum reconstruction in
762 proton-proton collisions at $\sqrt{s} = 13 \text{ TeV}$ using the CMS detector", *Submitted to: JINST*
763 (2019) arXiv:1903.06078.
- 764 [28] P. Lenzi, C. A. Palmer, J. Thomas-Wilsker et al., "Performance of flavour tagging
765 algorithms at 13 tev with 2018 data", CMS Note 2018/323, 2019.
- 766 [29] CMS Collaboration, "Search for New Physics with Jets and Missing Transverse
767 Momentum in pp collisions at $\sqrt{s} = 7 \text{ TeV}$ ", *JHEP* **08** (2011) 155,
768 doi:10.1007/JHEP08(2011)155, arXiv:1106.4503.
- 769 [30] CMS Collaboration, "Search for dark matter produced with an energetic jet or a
770 hadronically decaying W or Z boson at $\sqrt{s} = 13 \text{ TeV}$ ", *JHEP* **07** (2017) 014,
771 doi:10.1007/JHEP07(2017)014, arXiv:1703.01651.
- 772 [31] CMS Collaboration, "Performance of the CMS missing transverse momentum
773 reconstruction in pp data at $\sqrt{s} = 8 \text{ TeV}$ ", *JINST* **10** (2015) P02006,
774 doi:10.1088/1748-0221/10/02/P02006, arXiv:1411.0511.

- 782 [32] CMS Collaboration, “Measurement of the top quark pair production cross section in
783 proton-proton collisions at $\sqrt{s} = 13$ TeV”, *Phys. Rev. Lett.* **116** (2016) 052002,
784 doi:10.1103/PhysRevLett.116.052002, arXiv:1510.05302.
- 785 [33] CMS Collaboration, “Measurement of the ZZ production cross section and Z
786 $\rightarrow \ell^+ \ell^- \ell'^+ \ell'^-$ branching fraction in pp collisions at $\sqrt{s}=13$ TeV”, *Phys. Lett. B* **763** (2016)
787 280–303, doi:10.1016/j.physletb.2016.10.054, arXiv:1607.08834.
- 788 [34] CMS Collaboration, “Measurement of the WZ production cross section in pp collisions at
789 $\sqrt{s}=13$ TeV”, *Phys. Lett. B* **766** (2017) 268–290,
790 doi:10.1016/j.physletb.2017.01.011, arXiv:1607.06943.

DRAFT